UCL Université catholique de Louvain

École polytechnique de Louvain (EPL)

The scintillation phenomenon at low elevation angles in earth-space communications

Mémoire présenté par
Joachim KERVYN DE MEERENDRÉ

en vue de l'obtention du grade de Master
Ingénieur civil électricien

Promoteur(s)
Danielle VANHOENACKER-JANVIER

Lecteur(s)
Danielle VANHOENACKER-JANVIER, Christophe CRAEYE , Laurent QUIBUS

Année académique 2016-2017

Acknowledgements

Ces quelques mots de remerciements seront les seuls mots français de ce mémoire.

Tout d'abord, j'aimerais remercier le Prof. Danielle Vanhoenacker-Janvier de m'avoir encadré tout au long de ce mémoire. Au début de ce mémoire, j'étais complètement ignorant des différentes thématiques concernant la "Wave propagation theory" et elle me fut d'une grande aide dans mon processus de compréhension. Je voudrais aussi la remercier pour sa disponibilité et pour ses conseils toujours pertinents.

Je voudrais aussi remercier Laurent Quibus pour toute l'aide qu'il m'a fournie, notamment en ce qui concerne les fichiers de simulations Matlab®. Sans ses programmes, j'aurais eu plus de mal à faire toutes mes simulations de modèles.

Un grand remerciement à mes proches, principalement mes parents, qui m'ont toujours soutenu lors de ce mémoire et qui n'ont jamais cessé de m'encourager.

J'aimerais aussi remercier Léopold Van Brandt pour ses avis et suggestions concernant la structure de mon mémoire.

Finalement, j'aimerais adresser un remerciement particulier à Marjorie David qui a pris de nombreuses heures de son temps pour relire complètement mon mémoire.

Abstract

The scintillation phenomenon is a phenomenon which affects the amplitude and the phase of radio waves. In the scenario of an earth-satellite link, radio waves can encounter tropospheric turbulences in the atmosphere. These turbulences are the sources of amplitude and phase fluctuations which degrade the communications.

It has been proved that this phenomenon becomes stronger at higher frequencies. Since radio communications tend to reach higher frequencies, this phenomenon becomes more and more studied and modelled.

This work aims to test and find models which are going to reproduce the effect of the scintillation on radio waves. Therefore, we will derive analytical models under different hypotheses and see if they match real scintillation measurements.

This will be done by implementing a software program in Matlab®. Hence, we will be able to make an exhaustive comparison between our models and the measurements under different hypotheses and parameters. From this comparison, we will try to determine the best model and which hypothesis corresponds the most to the measurements.

Contents

Chapter 1

Introduction

This thesis will be focused on a phenomenon which is called tropospheric scintillation. This phenomenon is currently gaining more and more attention since satellite electromagnetic waves are emitted at increased frequencies [3].

Indeed, satellite frequency bands such as the L-band (1-2 GHz), the C-band (4-8 GHz) and the K_u band (8-12 GHz) are becoming quite "crowded" and congested. Consequently, the demands for a higher bandwidth are increasing. However, at these higher frequencies, the tropospheric scintillation can not be neglected.

Indeed, at high frequencies, the scintillation phenomenon will occur and degrade the radio waves by causing rapid fluctuations in the magnitude and the phase of the waves. These fluctuations are called scintillations and can reach several decibels [3]. This degradation can be a real problem for high frequencies satellite communications and can potentially a provoke loss of information.

This phenomenon is mainly caused by atmospheric turbulences which can be quite strong in clouds for example [8]. Atmospheric turbulences are zones characterized by winds which vary in speed and in direction [15]. In these turbulences, the refractive index will experience rapid fluctuations which are going to cause amplitude and phase fluctuations in radio waves. Therefore, it is the rapid fluctuations of the refractive index in the turbulences which are going to cause the scintillation phenomenon.

This phenomenon can also happen with optical waves. Therefore, if we take the example of a luminous object, we will observe variations in the brightness or in the position due to the scintillation phenomenon. This is because of the amplitude and phase fluctuations.

As it was said earlier, the scintillation phenomenon is mainly caused by the fluctuations of the refractive index. Indeed, the wave phase velocity will vary with refractive index. The refractive index describes how the light propagates through a medium and is defined like this :

$$n = \frac{c}{v} \tag{1.1}$$

Where n is the refractive index, c is the light speed and v is the phase speed.

Equivalently, we have :

$$v = \frac{c}{n} \tag{1.2}$$

Therefore, when n vary, so is the phase velocity. Consequently, the refractive index will cause changes in the phase speed resulting in important amplitude (constructive and/or destructive interferences) and phase fluctuations. Refractive index fluctuations can also increase scattering, which can also lead to more fluctuations.

In this thesis, we are going to investigate the effect of the scintillation phenomenon on 19 GHz radio communications between the antenna of the Svalbard station and LEO satellites. The Svalbard station is situated in the Norwegian archipelago in the Arctic Ocean (north of mainland Europe). The antenna of the Svalbard station has the particularity of having a very low elevation angle : 3.3 °. It has been proven that scintillation is more important with low-elevation angle. Therefore, the Svalbard station will be a good place to investigate this phenomenon and make some models.

Indeed, since scintillation fluctuations can have a non-negligible degradation on radio waves, it could be really interesting to build models in order to predict scintillation events and their magnitude so as to improve radio communications. For example, if we could predict with certainty the scintillation phenomenon, we could increase the frequency of the earth-satellite link in case of low scintillation (and thus increase the information flow). We could also change the emitted power in accordance with the intensity of the scintillation phenomenon and improve the design of the link budget (accounting of all gains and losses from the transmitter to the receiver).

Therefore, in the thesis, we will make several scintillation models and compare them with real measurements from the Svalbard station.

At figure 1.1 and table 1.1, we can see the configuration of the earth-satellite link of the Svalbard antenna and its characteristics.

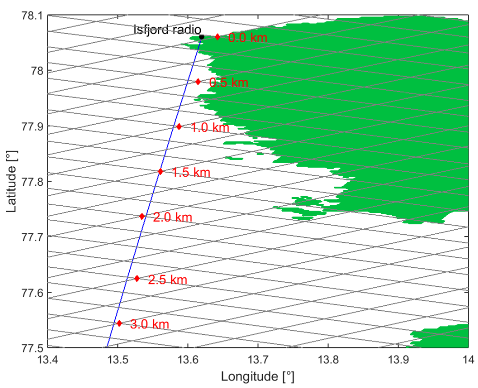

Figure 1.1 – Earth-Satellite link

Ground station longitude	13.62°
Ground station lattitude	78.06°
Ground station altitude	0
Link azimuth	183°
Link elevation	3°

Table 1.1 – Characteristics of the antenna

Figure 1.2 – Configuration of the Svalbard antenna

In order to make usable scintillation models for the Svalbard earth-satellite link, we need to introduce some concepts and formulas which are going to be useful to characterize the scintillation phenomenon.

Chapter 2

Fundamental Theory

In this chapter, we will introduce several concepts in order to find the temporal frequency spectrum of the amplitude fluctuation. Indeed, with this spectrum, we will be able to analyse the amplitude fluctuations or scintillations and see their dependence on the frequency.

This chapter is deeply inspired from Tatarski and Ishimaru work [18],[19],[10] on turbulence theory. At each beginning of a section, we will cite the pages from which the informations and computations are retrieved in order to avoid too much references.

2.1 Theory of non stationary random variables : correlation and structure function

Most meteorological variables such as temperature, pressure and wind velocity are completely random and non stationary. In order to be able to characterize these variables and to retrieve useful informations, we are going to introduce two important functions : the correlation and the structure function.

Suppose we have a function of time f(t) which is not stationary ($< f(t) >$ will thus vary over time) , we can define the function F_T as follows :

$$F_T(t) = f(t + T) - f(t) \tag{2.1}$$

If T is not too large, then the low frequency components of the function f(t) will not affect the value of the difference. This is due to the fact that the mean of f(t) will not change a lot over a period of time T if T is quite small.

In this case, we have an approximation of stationarity. Therefore, f(t) is called a random function with stationary first increments and $F_T(t)$ is only function of the time difference.

Now, we make the same reasoning for the following function :

$$\xi(t) = f(t) - < f(t) > \tag{2.2}$$

We have thus :

$$F_T(t) = \xi(t + T) - \xi(t) \tag{2.3}$$

If we take now a look at the correlation function of F_T, we have :

$$B_F(t) =< F_T(t+\tau)F_T(t) > \tag{2.4}$$

Using the definition of $F_T(t)$ (see equation 2.3), we obtain :

$$\begin{aligned} B_F(t) = \frac{1}{2}\{&< [\xi(t+T) - \xi(t+\tau)]^2 > + < [\xi(t+T+\tau) - \xi(t)]^2 > \\ &- < [\xi(t+T) - \xi(t+\tau+T)]^2 > - < [\xi(t+T) - \xi(t)]^2 >\} \end{aligned} \tag{2.5}$$

The structure function of the function ξ can be defined as in the following expression :

$$D_f(t_1, t_2) =< [\xi(t_1) - \xi(t_2)]^2 > \tag{2.6}$$

Using the two previous equations 2.5 and 2.6, the link between the correlation and the structure functions can be established :

$$B_F(\tau) = \frac{1}{2}D_f(t+\tau) + \frac{1}{2}D_f(t-\tau) - D_f(\tau) \tag{2.7}$$

Putting $< f(t) >= 0$, the structure function becomes :

$$D_f(\tau) =< [f(t+\tau) - f(t)]^2 > \tag{2.8}$$

If we expand the expression, we have :

$$D_f(\tau) =< [f(t+\tau)]^2 > + < [f(t)]^2 > -2 < [f(t+\tau)f(t)] > \tag{2.9}$$

Looking at the definition of the correlation function (equation 2.4) and using the stationarity of f(t), the following relation can be shown :

$$D_f(\tau) = 2[B_f(0) - B_f(\tau)] \tag{2.10}$$

In the meteorology domain, the structure function will often replace the correlation function the characterization of processes. The structure function represents the intensity of fluctuation within a period comparable to τ.

The exact same reasoning can be applied to variable functions of space. Using the structure definition (see equation 2.6) applied to the space, we can have :

$$D(\mathbf{r}_1, \mathbf{r}_2) =< \{[f(\mathbf{r}_1)- < f(\mathbf{r}_1) >] - [f(\mathbf{r}_2)- < f(\mathbf{r}_2) >]\}^2 > \tag{2.11}$$

If the random field is homogeneous (space stationarity), then we have :

$$D(\mathbf{r}_1 + \mathbf{r}, \mathbf{r}_1) = D(\mathbf{r}) \tag{2.12}$$

If we suppose that the process is isotropic, we have :

$$D(\mathbf{r}) = D(r) \tag{2.13}$$

In general, we will make the hypothesis of local homogeneity and local isotropy. This means that in a small zone around the point we observe, the process can be considered isotropic and homogeneous.

The structure and the correlation function are really important in the characterization of random variables. As said before, the structure and correlation functions will give us information about the intensity of the fluctuation of a variable. Such functions are going to be useful later in order to characterize the scintillation phenomenon.

2.2 Definition of the spatial frequency spectra

This section presents some important concepts and equations about the different types of spatial spectra in the theory of random fields. We will not always show the whole mathematical reasoning because it is not the main topic of this thesis and for the sake of brevity. More details about the hypothesis, the computations and their steps can be found in [18, pp. 15-26] and in [19, pp 4-32]. These spatial spectra are going to be useful because they will allows us to compute the temporal spectrum of the scintillaion.

One way to represent an homogeneous random field (for example the wind velocity) is to use the 3D stochastic Fourier-Stieltjes transform.

$$f(\mathbf{r}) = \int\int\int_{-\infty}^{\infty} exp(i\boldsymbol{\kappa}\cdot\mathbf{r})d\varphi(\kappa_1,\kappa_2,\kappa_3). \tag{2.14}$$

Using the definition of the correlation function (equation 2.4) and the homogeneity hypothesis, it is possible to show the following relation :

$$B_f(\mathbf{r}_1-\mathbf{r}_2) = \int\int\int exp(i\boldsymbol{\kappa}\cdot(\mathbf{r}_1-\mathbf{r}_2))\Phi(\boldsymbol{\kappa})d\boldsymbol{\kappa} \tag{2.15}$$

Where $\Phi(\boldsymbol{\kappa})$ is the 3D spatial frequency spectrum.

Since the $B_f(\mathbf{r}_1-\mathbf{r}_2) = B_f(\mathbf{r}_2-\mathbf{r}_1)$, we can write :

$$B_f(\mathbf{r}) = \int\int\int cos(\boldsymbol{\kappa}\cdot\mathbf{r})\Phi(\boldsymbol{\kappa})d\boldsymbol{\kappa} \tag{2.16}$$

It is also possible to show that :

$$\Phi_f(\boldsymbol{\kappa}) = \int\int\int cos(\boldsymbol{\kappa}\cdot\mathbf{r})B_f(\mathbf{r})d\mathbf{r} \tag{2.17}$$

Therefore, the functions $B_f(\mathbf{r})$ and $\Phi_f(\boldsymbol{\kappa})$ are Fourier transforms of each other.

The 1D spatial frequency spectrum can also be defined if we consider a straight line in a certain direction and look at the values of the field along this line.

$$B_f(x) = \int \cos(\kappa x)V(\kappa)dx \tag{2.18}$$

$$V(\kappa) = \frac{1}{\pi}\int_0^{\infty} B_f(x)\cos(\kappa x)dr \tag{2.19}$$

If we add now the local isotropy hypothesis, it is possible to prove the following relation between the 1D and the 3D spatial frequency spectra with a few computations.

$$\Phi(\kappa) = -\frac{1}{2\pi\kappa}\frac{dV(\kappa)}{d\kappa} \tag{2.20}$$

The 2D spectrum can also be defined. Let a function $f(x,y,z)$ in the constant plan x be :

$$f(x,y,z) = \int_{-\infty}^{\infty}\int_{-\infty}^{\infty} exp[i(\kappa_2 y+\kappa_3 z)]d\psi(\kappa_2,\kappa_3,x) \tag{2.21}$$

We can rewrite :

$$f(x,y,z) = f(x,0,0) + \int_{-\infty}^{\infty}\int_{-\infty}^{\infty} (1-exp[i(\kappa_2 y+\kappa_3 z)])\, d\psi(\kappa_2,\kappa_3,x) \tag{2.22}$$

Using again the definition of the structure function and the homogeneity, we can obtain the 2D spatial frequency spectrum of the structure function $F(\kappa_2, \kappa_3, 0)$.

$$D_f(0, \eta, \psi) = 2 \int\int [1 - cos(\kappa_2 \eta + \kappa_3 \zeta)] F(\kappa_2, \kappa_3, 0) d\kappa_2 d\kappa_3 \tag{2.23}$$

With $\eta = y - y^t$ and $\zeta = z - z^t$. η and ζ are the y and z difference between the two considered points of the structure function in the plane x.

Taking the local isotropy hypothesis, we eventually obtain :

$$D_f(\rho) = 4\pi \int_0^\infty [1 - J_0(\kappa\rho)] F(\kappa, 0) \kappa d\kappa \tag{2.24}$$

With $\kappa = \sqrt{\kappa_2^2 + \kappa_3^2}$ and $\rho = \sqrt{\eta^2 + \psi^2}$. J_0 is the 0^{th} Bessel Function [18, pp. 23,262].

Using the equation 2.10, it can be showed that the correlation function has the following expression :

$$B_f(\rho) = 2\pi \int_0^\infty [J_0(\kappa\rho)] F(\kappa, 0) \kappa d\kappa \tag{2.25}$$

Now that the 2D and the 3D spatial frequency spectra have been defined, it is possible to show that they are linked by the following relation :

$$\Phi(\kappa_1, \kappa_2, \kappa_3) = \frac{1}{2\pi} \int_{-\infty}^{\infty} cos(\kappa_1 x) F(\kappa_2, \kappa_3, x) dx \tag{2.26}$$

With this last equation, we have succeeded to introduce these important spectra. As we will see it later, these spectra will be useful in order to compute the temporal frequency spectrum of the scintillation.

We will now take an example of structure function and compute its 3D spatial frequency spectrum. We will see later that this example has not been taken randomly.

Given the following structure function :

$$D_f(r) = c^2 r^p \quad (0 < p < 2) \tag{2.27}$$

Where c is a constant and r is the distance between two points.

It can be shown that the associated 1D spatial frequency spectrum has the following form [18] :

$$V(\kappa) = \frac{\Gamma(p+1)}{2\pi} \sin\left(\frac{\pi p}{2}\right) c^2 \kappa^{-(p+1)} \tag{2.28}$$

Using the equation 2.20, we obtain the 3D spectrum :

$$\Phi(\kappa) = -\frac{1}{2\pi\kappa} \frac{\Gamma(p+1)}{2\pi} \sin\left(\frac{\pi p}{2}\right) c^2 (-(p+1)) \kappa^{-(p+2)} \tag{2.29}$$

Using the fact that $\Gamma(z+1) = z\Gamma(z)$.

$$\Phi(\kappa) = \frac{\Gamma(p+2)}{4\pi^2} sin(\frac{\pi p}{2}) c^2 \kappa^{-(p+3)} \tag{2.30}$$

If we took the example of p = 2/3, we would thus obtain :

$$\Phi(\kappa) = \frac{\Gamma(8/3)}{4\pi^2} sin(\frac{\pi}{3}) c^2 \kappa^{-11/3} = 0.033 c^2 \kappa^{-11/3} \tag{2.31}$$

This 3D spatial frequency spectrum will be used later in this work.

2.3 The 2D amplitude and phase spatial-frequency spectra

At this stage, we have defined the structure function, the correlation function and several types of spectra. These definitions have been made considering random field functions or random functions. We could for example have a look at the structure function of the temperature, wind speed or any other random variable.

However, for the scintillation phenomenon, it is the amplitude and the phase fluctuations of the wave passing through the atmosphere that will interest us. We will thus be interested at the 2D and 3D spatial frequency spectra of the amplitude and the phase. Once we have them, we will be able to have a look at the structure function of the amplitude and the phase.

2.3.1 The wave equation : hypothesis and reformulation

As done before, we will not show the whole mathematical reasoning. These can be found in [18, pp.122-128].

Starting from the Maxwell equations for an electromagnetic field which has a time dependence like this : $e^{i\omega t}$, we can obtain the wave equation in the following form :

$$\Delta\vec{E} + k^2n^2\vec{E} + 2\nabla(\vec{E}\cdot\nabla\log n) = 0 \tag{2.32}$$

Where $\vec{E}$ is the electric field, k is the wave number and n is the refractive index. It is important to know that this equation also suppose that there are no free charges in the atmosphere and that the magnetic permeability is constant [13].

As said before in the introduction, the variations in the refractive index are mainly caused by the turbulences or eddies. In the turbulence theory, one can define the inner scale l_0 which is the characteristic length of the smallest turbulence. Once this inner scale is defined, we can assume that below l_0, the refractive index will not change much and that therefore $\nabla\log n$ will be quite small below this value.

If we assume now that all the inhomogeneities in the spatial distribution of the refractive index are much greater than the wavelength, then the last term of the equation will be very small compared to the other ones and we can neglect it [18, pp. 93,267].

This condition can be put equivalently in equation :

$$\lambda << l_0 \tag{2.33}$$

Neglecting the last term and reducing the vector equation in three scalar equations, we obtain :

$$\Delta u + k^2n^2(\mathbf{r})u = 0 \tag{2.34}$$

Since the refractive index of the air is approximately equal to 1 and given that our wave goes through the atmosphere, we can make the following decomposition :

$$n = 1 + n_l \tag{2.35}$$

Assuming that $|n_l| << 1$.

Doing some manipulations with the wave equation, we have :

$$\Delta u + k^2 n^2(\mathbf{r}) u = \frac{\Delta u}{u} + k^2 n^2(\mathbf{r}) = \Delta \log u + (\nabla \log u)^2 + k^2 n^2(\mathbf{r}) = 0 \tag{2.36}$$

Setting $\log u = \log A + iS = \psi$, we have :

$$\Delta \psi + (\nabla \psi)^2 + k^2 (1 + n_l(\mathbf{r}))^2 = 0 \tag{2.37}$$

We make the following decomposition :

$$\psi = \psi_0 + \psi_l \tag{2.38}$$

Where ψ_0 corresponds the the unperturbed part of the wave and ψ_l to the perturbed part. By the principle of the small perturbation method, we can say that the wave equation will also be valid for ψ_0, the unperturbed part of the wave.

ψ_0 satisfies thus the following equation :

$$\Delta \psi_0 + (\nabla \psi_0)^2 + k^2 = 0 \tag{2.39}$$

Making the substitution and inserting equation 2.39 in equation 2.37, it is possible to obtain :

$$\Delta \psi_l + \Delta \psi_l \cdot (2\Delta \psi_0 + \Delta \psi_l) + 2k^2 n_l(\mathbf{r}) + k^2 n_l^2(\mathbf{r}) = 0 \tag{2.40}$$

We also make the following assumption :

$$|\nabla \psi_l| << |\nabla \psi_0| \tag{2.41}$$

By doing some dimensional reasoning, the condition $|\nabla \psi_l| << |\nabla \psi_0|$ can be transform in an equivalent condition :

$$|\nabla \psi_l| << k = \frac{2\pi}{\lambda} \tag{2.42}$$

It means that ψ_l cannot change much over distances of the order of the wavelength.

We eventually have this equation :

$$\Delta \psi_l + 2\nabla \psi_0 \cdot \nabla \psi_l + 2k^2 n_l(\mathbf{r}) = 0 \tag{2.43}$$

In the case where we have $u_0 = A_0 e^{ikx}$ (monochromatic planar wave) and $\lambda << l_0$, this equation can be greatly simplified :

$$\frac{\delta^2 \psi_l}{\delta y^2} + \frac{\delta^2 \psi_l}{\delta z^2} + 2ik \frac{\delta \psi_l}{\delta x^2} + 2k^2 n_l(\mathbf{r}) = 0 \tag{2.44}$$

This equation will be useful in order to find the spatial frequency spectra of the amplitude and phase fluctuation of the wave going through the atmosphere.

2.3.2 Finding the 2D spatial frequency spectrum using the spectral expansions method

The spectral expansion method is a method used to represent random variables in function of their spectrum. This method will allow us to compute the phase and amplitude spatial frequency spectra. More details about this reasoning using the spectral expansions method can be found in [18, pp. 128-134].

Using this method for the refractive index and for ψ, we obtain :

$$n_l(x,y,z) = n_l(x,0,0) + \int_{-\infty}^{\infty}\int_{-\infty}^{\infty}[1 - e^{i(\kappa_2 y+\kappa_3 z)}]d\nu(\kappa_2,\kappa_3,x) \tag{2.45}$$

$$\psi_l(x,y,z) = \psi_l(x,0,0) + \int_{-\infty}^{\infty}\int_{-\infty}^{\infty}[1 - e^{i(\kappa_2 y+\kappa_3 z)}]d\varphi(\kappa_2,\kappa_3,x) \tag{2.46}$$

Where $d\nu$ and $d\varphi$ are the spectral representations of n_l and ψ.

Inserting this two equations in our reformulated wave equation from the previous section (see equation 2.44) and doing some manipulations, it can be shown that :

$$d\varphi(\kappa_2,\kappa_3,x) = ik\int_0^x dx^{'} exp[-\frac{i\kappa^2(x-x^{'})}{2k}]d\nu(\kappa_2,\kappa_3,x^{'}) \tag{2.47}$$

Taking the real part ($\chi = Re\ \psi_l$) and the imaginary part ($S_l = Im\ \psi_l$) of the equation 2.46, we can obtain the following equations :

$$da(\kappa_2,\kappa_3,x) = k\int_0^x dx^{'} sin[\frac{\kappa^2(x-x^{'})}{2k}]d\nu(\kappa_2,\kappa_3,x^{'}) \tag{2.48}$$

$$d\sigma(\kappa_2,\kappa_3,x) = k\int_0^x dx^{'} cos[\frac{\kappa^2(x-x^{'})}{2k}]d\nu(\kappa_2,\kappa_3,x^{'}) \tag{2.49}$$

Where da and $d\sigma$ are the spectral representations of the fluctuation log-amplitude (χ) and the fluctuation phase (S_l)

Multiplying the equation 2.48 by its complex conjugate and averaging afterwards, we have :

$$\begin{aligned}\overline{da(\kappa_2,\kappa_3,x)da^*(\kappa_2^{'},\kappa_3^{'},x)} = k^2\int_0^x dx^{'}\int_0^x dx^{''} sin[\frac{\kappa^2(x-x^{'})}{2k}]\\ \times sin[\frac{(\kappa^{'})^2(x-x^{''})}{2k}]\overline{d\nu(\kappa_2,\kappa_3,x)d\nu^*(\kappa_2^{'},\kappa_3^{'},x)}\end{aligned} \tag{2.50}$$

The same reasoning can be done for 2.47 and 2.49 to obtain $\overline{d\nu(\kappa_2,\kappa_3,x)d\nu^*(\kappa_2^{'},\kappa_3^{'},x)}$ and $\overline{d\sigma(\kappa_2,\kappa_3,x)d\sigma^*(\kappa_2^{'},\kappa_3^{'},x)}$.

If we suppose that our variables are homogeneous, then their correlations must depend only on the distance between the two chosen points (and not on their positions).

The following equations must thus be satisfied :

$$\overline{d\nu(\kappa_2,\kappa_3,x)d\nu^*(\kappa_2^{'},\kappa_3^{'},x)} = \delta(\kappa_2-\kappa_2^{'})\delta(\kappa_3-\kappa_3^{'})F_n(\kappa_2,\kappa_3,0)d\kappa_2 d\kappa_3 d\kappa_2^{'} d\kappa_3^{'} \tag{2.51}$$

$$\overline{da(\kappa_2,\kappa_3,x)da^*(\kappa_2^{'},\kappa_3^{'},x)} = \delta(\kappa_2-\kappa_2^{'})\delta(\kappa_3-\kappa_3^{'})F_\chi(\kappa_2,\kappa_3,0)d\kappa_2 d\kappa_3 d\kappa_2^{'} d\kappa_3^{'} \quad (2.52)$$

$$\overline{d\sigma(\kappa_2,\kappa_3,x)d\sigma^*(\kappa_2^{'},\kappa_3^{'},x)} = \delta(\kappa_2-\kappa_2^{'})\delta(\kappa_3-\kappa_3^{'})F_S(\kappa_2,\kappa_3,0)d\kappa_2 d\kappa_3 d\kappa_2^{'} d\kappa_3^{'} \quad (2.53)$$

Where F_n is the 2D spectral function of the refractive index, F_A the 2D spectral density of the structure function of the fluctuations of χ in the plane x and F_σ the 2D spectral density of the structure function of the fluctuations of S_l in the plane x.

Inserting equations 2.52 and 2.51 in the equation 2.50, we obtain :

$$\begin{aligned} F_\chi(\kappa_2,\kappa_3,0) = k^2 \int_0^x dx^{'} \int_0^x dx^{''} sin[\frac{\kappa^2(x-x^{'})}{2k}] \times sin[\frac{\kappa(x-x^{tt})}{2k}] \\ \times F_n(\kappa_2,\kappa_3,x^{'}-x^{''}) \end{aligned} \quad (2.54)$$

The same method can be followed for the phase to find the expression of F_s. Therefore, we have obtained the expressions for the 2D spatial frequency spectra of the log-amplitude and phase fluctuation. However, if we look t the equation 2.54, we still have an unknown : F_n.

In order to find F_n, we are going to introduce the Kolmogorov law.

2.4 The Kolmogorov law and its hypothesis

In 1941, Kolmogorov advanced several hypotheses about the structure function of the refractive index in a turbulent medium. In this section, we will explain and use his hypotheses.

As a reminder, a turbulent medium is a medium in which turbulences or eddies can be found. This eddies can have different proportions and are described by their characteristic length which represent their size. The two first subsections are based from [19, pp. 51-54],[4].

2.4.1 Kinetic energy and energy dissipation of the turbulences

In the theory of turbulent flow, it is possible to show the two following definitions :

$$T = \int_0^{+\infty} E(\kappa)d\kappa$$

$$\epsilon = 2\nu \int_0^{+\infty} \kappa^2 E(\kappa)d\kappa$$

Where T is the kinetic energy and $E(\kappa)$ its associated spectral density. κ is the spatial frequency and can be given by $\kappa = \frac{2\pi}{l}$ where l is the characteristic size of the eddy. ϵ is the rate of energy dissipation and ν is the kinematic viscosity.

It has been shown by experimental data that $E(\kappa)$ and the spectrum of ϵ have the following forms (see 2.1a and 2.1b).

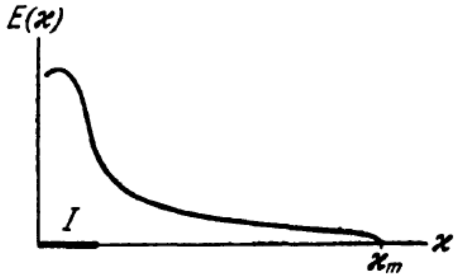

(a) Typical curve of the spectral energy density in turbulent flow [18]

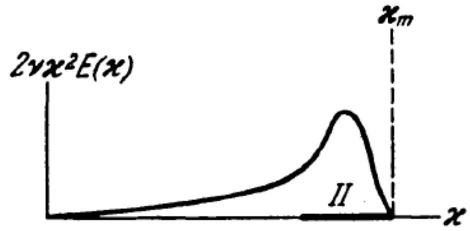

(b) Spectral density of the energy dissipation rate [18]

We can distinguish 3 different regions for these two spectra (see figure 2.1b and 2.1a). This regions can be see more clearly in the figure 2.2 which show the spectral energy density again.

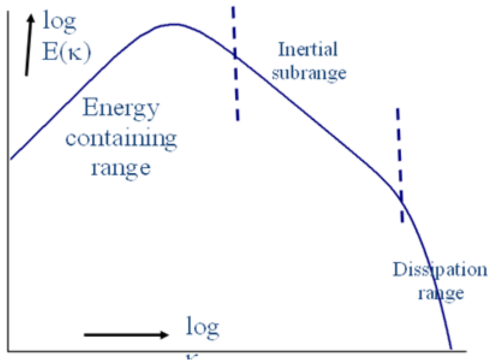

Figure 2.2 – Typical curve of the spectral energy density in turbulent flow [11]

As we can see in the figure 2.2, there are 3 regions. The first one is the input range, the second one the inertial range and the last one is the dissipation range. At low frequencies (large eddies), we have the input range where the energy is entering the spectrum. At higher frequencies (small eddies), the energy is progressively dissipated and decreases rapidly towards 0 as the eddies becomes smaller. In the figure 2.1a, the spatial frequency corresponding to $E(x) = 0$ is x_m. Between the input and the dissipation range, we have the inertial range where $\log E(\kappa)$ seems to decrease linearly (see figure 2.2).

These 3 regions are separated by the two following frequencies :

- $\kappa_{L_0} = \frac{2\pi}{L_0}$ which is between the input range and the inertial range. L_0 is called the outer scale.
- $\kappa_{l_0} = \frac{2\pi}{l_0}$ which is between the inertial range and the dissipation range. l_0 is called the inner scale.

In the figure 2.1b, we can see that the spectral density of the energy dissipation rate is generally low except in the dissipation region, where it increases a lot. Indeed, when $E(\kappa)$ decreases, it means that there is more dissipation. This is thus logical that the spectral density of the energy dissipation rate is higher in this region.

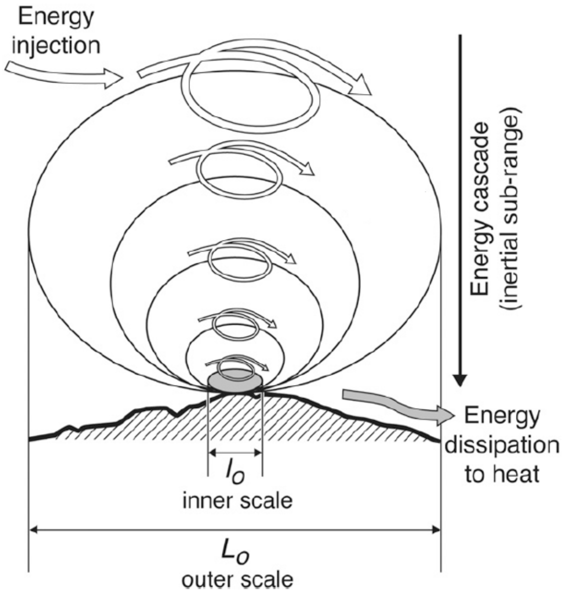

Figure 2.3 – Fragmentation process [4]

It can be viewed as a process of eddy fragmentation : large eddies, which contain most of the energy, fragment into smaller ones which will contain less energy (see figure 2.3). This process stops when the dissipation rate becomes equal to zero : the eddies are now stable.

2.4.2 Structure function formula according Kolmogorov's hypothesis

With the shape of the spectra in figures 2.1b and 2.1a come the hypotheses of Kolmogorov, which are the following :

- In the equilibrium range (dissipation range and inertial range) at very high Re, the structure function of the turbulence velocity only depends only on ν (the viscosity) and ϵ (the dissipation rate).
- In the inertial sub-range, the structure function depends on ϵ only

Thanks to these hypotheses and doing a dimension reasoning, it is possible to obtain the well-known Kolomogorov 2/3 law :

$$D_{rr}(r) = C^2 \epsilon^{2/3} r^{2/3} \qquad l_0 << r << L_0 \tag{2.55}$$

Where D_{rr} is the structure function of the wind velocity of the radial components and r is the distance between two considered points. This equation is only valid in the inertial sub-range.

Analogous reasoning can be applied for other variables such as temperature and refractive index. Therefore, for the refractive index, we have :

$$D_n(r) = C_n^2 r^{2/3} \qquad l_0 << r << L_0 \tag{2.56}$$

Or equivalently :

$$D_n(\vec{r_1}, \vec{r_2}) = C_n^2 |\vec{r_1} - \vec{r_2}|^{2/3} \qquad l_0 << |\vec{r_1} - \vec{r_2}| << L_0 \tag{2.57}$$

As it was written before, l_0 and L_0 are called the inner and the outer scale and define the limits of the inertial range. In general, their precise values are unknown. However, their order of magnitude is known :

- $l_0 \in [1mm - 1cm]$
- $L_0 \in [10m - 100m]$

With the right hypothesis, it is also possible to show that in the dissipation range, the structure function of the refractive index has the following shape :

$$D_n(r) = C_n^2 l_0^{2/3} \left(\frac{r}{l_0}\right)^2 \qquad r << l_0 \tag{2.58}$$

Or equivalently :

$$D_n(\vec{r_1}, \vec{r_2}) = C_n^2 l_0^{2/3} \left(\frac{|\vec{r_1} - \vec{r_2}|}{l_0}\right)^2 \qquad |\vec{r_1} - \vec{r_2}| << l_0 \tag{2.59}$$

If we have another look at the "two-third" law (equation 2.57) and at equation 2.59, we see that they only depend on the distance between two given observation points and not on their positions. This is due to the homogeneity hypothesis.

However, in practice, this hypothesis is never completely true. Indeed, in reality, the structure function of a random variable such as the refractive index will not only depend on the distance between the observation points but also on their positions. The C_n^2 could not be the same for the whole atmosphere and will thus vary with the position [18, pp. 164].

It would be much closer to reality to write the following equation :

$$D_n(\vec{r_1}, \vec{r_2}) = \begin{cases} C_n^2(\frac{\vec{r_1}+\vec{r_2}}{2})|\vec{r_1} - \vec{r_2}|^{2/3} & l_0 << |\vec{r_1} - \vec{r_2}| << L_0 \\ C_n^2(\frac{\vec{r_1}+\vec{r_2}}{2}) l_0^{2/3} \left(\frac{|\vec{r_1}-\vec{r_2}|}{l_0}\right)^2 & |\vec{r_1} - \vec{r_2}| << l_0 \end{cases} \tag{2.60}$$

These two expressions (equations 2.60) are only valid considering two observation points with a distance of the same order as L_0 or smaller. If the distance between the two observation points in bigger, then we leave the inertial range and we can no longer use these equations.

If we suppose now that we take another pair of observation points in another region of the atmosphere and that the distance between them is smaller than L_0, then these two expressions (equations 2.60) can be used. However, since it is another region, the C_n^2 will not be the same.

> Therefore we can assume that C_n^2 is a smooth function of the coordinates, which change appreciably only in distances of the order L_0 [18, p. 164].

2.4.3 The 3D spatial frequency spectrum of the refractive index

Now that we have the expression of structure function of the refractive index in the inertial range, we can compute the 3D spatial spectrum. The reasoning to compute it was done in a previous section (see equation 2.31).

Therefore, in the **inertial range**, the 3D spatial spectrum of the refractive index has the following equation :

$$\Phi_n(\kappa, \frac{\vec{r_1}+\vec{r_2}}{2}) = 0.033\ C_n^2(\frac{\vec{r_1}+\vec{r_2}}{2})\ \kappa^{-11/3} \tag{2.61}$$

Where C_n^2 is a constant which is unknown.

It is important to know here that this spectrum is only valid in the inertial range between l_0 and L_0.

The Von Karman spectrum

As it was just said before, the Kolmogorov spectrum is only valid in the inertial range. In the dissipation range, it can be shown that the 3D spatial spectrum of the refractive index is approximately null. In the input range, however, the local isotropy and local homogeneity hypotheses are no longer correct and the 3D spatial spectrum of the refractive index is completely unknown. The only thing we know in the input range about the spectrum is that it is finite.

We have thus :

$$\Phi_n(\kappa) = \begin{cases} 0.033\ C_n^2(\frac{\vec{r_1}+\vec{r_2}}{2})\ \kappa^{-11/3} & 2\pi/L_0 < \kappa < 2\pi/l_0 \\ 0 \quad 2\pi/l_0 < \kappa \end{cases} \tag{2.62}$$

One common way to combine these two parts of the spectrum can be seen in the following equation :

$$\Phi_n^{(eqrge)}(\kappa) = 0.033\ C_n^2(\frac{\vec{r_1}+\vec{r_2}}{2})\ \kappa^{-11/3} exp(-\kappa^2/\kappa_m^2) \qquad 2\pi/L_0 < \kappa \tag{2.63}$$

Where $\kappa_m = 5.92/l_0$ and which is valid for the inertial and the dissipation range [10, p. 368].

Another equation which is often used is the following :

$$\Phi_n^{(vk)}(\kappa) = 0.033\ C_n^2(\frac{\vec{r_1}+\vec{r_2}}{2})(\kappa_L^2+\kappa^2)^{-11/3} exp(-\kappa^2/\kappa_m^2) \qquad 2\pi/L_0 < \kappa \tag{2.64}$$

Where $\kappa_L = 1/L_0$ [10, p. 368].

This equation has the advantage of covering the whole range even if the input range can not normally be described in an isotropic form as it is done here [21]. This equation makes the supposition that the 3D spectrum is constant in the input range. This equation is called the Von Karman spectrum. We will not use the Von Karman spectrum in this chapter but it will be useful later.

Now that we have the 3D spatial spectrum of the refractive index, we are going to come back to the computation of the 2D spatial frequency spectra of the log-amplitude and the phase fluctuation (see equation 2.54). We will then be able to find their structure functions.

2.5 The log-amplitude and phase fluctuation structure functions

In the section 2.2, we showed that the 2D and the 3D spatial spectrum are linked by the relation 2.26 which we will apply here to the refractive index.

We have thus :

$$\Phi_n(\kappa_1, \kappa_2, \kappa_3) = \frac{1}{2\pi}\int_{-\infty}^{\infty} cos(\kappa_1 x)F_n(\kappa_2, \kappa_3, x)dx \tag{2.65}$$

Putting $\kappa_1 = 0$ and looking at two points whose distance is $\xi = x^{'} - x^{''}$, we can find :

$$\pi\Phi_n(0, \kappa_2, \kappa_3) = \int_0^{\infty} F_n(\kappa_2, \kappa_3, \xi)d\xi \tag{2.66}$$

Since, we suppose that the refractive index is a locally isotropic field, we can make the following simplification :

$$\pi\Phi(\kappa) = \int_0^{\infty} F(\kappa, \xi)d\xi \tag{2.67}$$

As we have seen in section 2.4, the 3D spatial frequency spectrum of the refractive index Φ_n depends also on the position. Consequently, the 2D spatial frequency spectrum will also have this dependence :

$$\pi\Phi_n(\kappa, \eta) = \int_0^{\infty} F_n(\kappa, \xi, \eta)d\xi \tag{2.68}$$

Where $\eta = \frac{x^{'}+x^{''}}{2}$ [18, p.165].

If we now come back to the equation 2.54 of the amplitude 2D space spectrum and consider its dependence on the position, we have the following equation [18, p.166].

$$\begin{aligned} F_A(\kappa_2, \kappa_3, 0) = k^2 \int_0^x dx^{'} \int_0^x dx^{''} sin[\frac{\kappa^2(x - x^{'})}{2k}] \times sin[\frac{\kappa(x - x^{tt})}{2k}] \\ \times F_n(\kappa_2, \kappa_3, x^{'} - x^{''}, \frac{x^{'} + x^{''}}{2}) \end{aligned} \tag{2.69}$$

Therefore, according on whether the C_n^2 is dependent on the position or not, F_n and Φ_n may depend on the position η.

In this work, we will consider both cases.

1. C_n^2 is considered to be constant no matter the position. Consequently, D_n, F_n and Φ_n will not be position dependant.
2. C_n^2 varies with the position and so do D_n, F_n and Φ_n.

2.5.1 The 2D spatial frequency spectrum when C_n^2 is constant

More informations about the computations of this subsection can be found in [**?**, pp. 134-136]

If we consider the C_n^2 to be constant, then the 2D spatial frequency spectrum of the amplitude has the following expression :

$$F_A(\kappa_2, \kappa_3, 0) = k^2 \int_0^x dx^{'} \int_0^x dx^{''} sin[\frac{\kappa^2(x-x^{'})}{2k}] \times sin[\frac{\kappa(x-x^{tt})}{2k}] \\ \times F_n(\kappa_2, \kappa_3, x^{'} - x^{''}) \tag{2.70}$$

With the following change of variables : $\zeta = x^{'} - x^{''}$ and $2\eta = x^{'} + x^{''}$ and some reasoning, it is possible to obtain the equations 2.71 and 2.72.

$$F_A(\kappa_2, \kappa_3, 0) \approx \int_0^L \left(k^2 L - \frac{k^3}{\kappa^2} sin \frac{\kappa^2 L}{k} \right) F_n(\kappa_2, \kappa_3, \zeta) d\zeta \tag{2.71}$$

$$F_S(\kappa_2, \kappa_3, 0) \approx \int_0^L \left(k^2 L + \frac{k^3}{\kappa^2} sin \frac{\kappa^2 L}{k} \right) F_n(\kappa_2, \kappa_3, \zeta) d\zeta \tag{2.72}$$

Where F_A and F_S are respectively the 2D spatial frequency spectra of the amplitude and the phase at an observation point whose x coordinate is L (see figure 2.4).

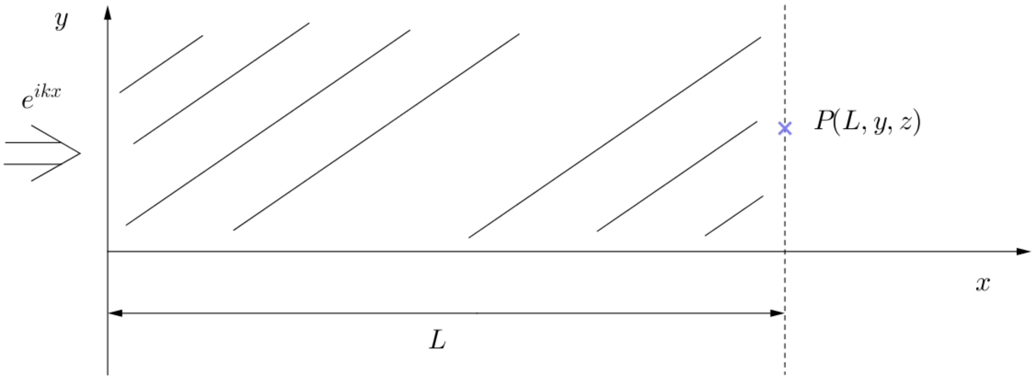

Figure 2.4 – Wave going trough the turbulent zone

As we can see it in the figure 2.4, at x = 0, we have the wave which is entering the turbulent zone up to the plane x = L, where the turbulent zone ends. This is the reason why the integration over $\zeta = x^{'} - x^{''}$ is done from 0 towards L.

Since F_n is very small for high values of ζ (Φ_n and consequently F_n are very small in the dissipation region), the integral can be prolonged towards infinity.

$$F_A(\kappa_2, \kappa_3, 0) \approx \int_0^\infty \left(k^2 L - \frac{k^3}{\kappa^2} sin \frac{\kappa^2 L}{k} \right) F_n(\kappa_2, \kappa_3, \zeta) d\zeta \tag{2.73}$$

Using the relation between the 2D and 3D spectra (equation 2.67) and considering local isotropy, we eventually have :

$$F_A(\kappa, 0) \approx \pi k^2 L \left(1 - \frac{k}{\kappa^2 L} sin \frac{\kappa^2 L}{k} \right) \Phi_n(\kappa) \tag{2.74}$$

$$F_S(\kappa,0) \approx \pi k^2 L \left(1 - \frac{k}{\kappa^2 L} sin\frac{\kappa^2 L}{k}\right) \Phi_n(\kappa) \tag{2.75}$$

With these two equations, we have found the expression of the 2D spatial frequency spectra of the amplitude and the phase when C_n^2 is constant.

2.5.2 The 2D spectrum when C_n^2 varies

In reality, the C_n^2 will vary in the atmosphere and consequently, the 2D spatial frequency spectrum of the amplitude will depend on the position $\frac{r^{'}+r^{''}}{2}$.

$$\begin{aligned} F_A(\kappa_2,\kappa_3,0) = k^2 \int_0^x dx^{'} \int_0^x dx^{''} sin[\frac{\kappa^2(x-x^{'})}{2k}] \times sin[\frac{\kappa(x-x^{tt})}{2k}] \\ \times F_n(\kappa_2,\kappa_3,x^{'}-x^{''},\frac{r^{'}+r^{''}}{2}) \end{aligned} \tag{2.76}$$

Making some operations and some changes of variables, it is possible to obtain the two following equations for F_A and F_S.

$$F_A(\kappa,0) \approx 2\pi k^2 \int_0^L C_n^2(\vec{r})\Phi_n^{(o)}(\kappa) sin^2[\frac{\kappa^2(L-\eta)}{2k}]d\eta \tag{2.77}$$

$$F_S(\kappa,0) \approx 2\pi k^2 \int_0^L C_n^2(\vec{r})\Phi_n^{(o)}(\kappa) cos^2[\frac{\kappa^2(L-\eta)}{2k}]d\eta \tag{2.78}$$

Where $\Phi_n^{(o)}$ is the 3D spatial frequency spectrum of the refractive index without the C_n^2 and $\eta = \frac{r^{'}+r^{''}}{2}$.

With these two equations, we have found the expressions of the 2D spatial frequency spectra of the amplitude and the phase when C_n^2 varies. We will now be able to compute the structure functions of the amplitude and the phase.

2.6 Definition of the temporal frequency spectrum

Now that we have found the 2D spatial frequency spectra of the amplitude and the phase fluctuation, it will be possible to compute their structure function and their temporal frequency spectra. Therefore, with the time-frequency spectrum, we will be able to characterize the scintillation phenomenon which will allow us to see its influence over the whole range of temporal frequencies. More details about this section can be found in [10, pp. 388-391].

The temporal frequency spectrum of the log-amplitude fluctuation is the Fourier transform of the log-amplitude fluctuation correlation function [10, p. 391], [13], [22].

$$W_\chi(\omega) = 2\int_{-\infty}^{\infty} B_\chi(L,\tau)e^{i\omega\tau}d\tau = 4\int_0^{\infty} B_\chi(L,\tau)cos(\omega\tau)d\tau. \tag{2.79}$$

It is important to say here that the correlation has no unity and so has the spectrum W_χ.

Until now, we have considered that the correlation and the structure function were only function of the position and not of the time. However, without a time dependence, it is impossible to have the temporal frequency spectrum of the amplitude.

In order to consider the time dependence of the correlation, we will make the hypothesis that the medium is moving with the wind at a velocity of $V = U + V_f$ (U is the average velocity and V_f is the fluctuation velocity). We will also consider that the velocity is slowly varying in function of the time and that V_f is negligible.

> For example, in turbulence, we assume that the eddies of a certain size l do not appreciably change their shape within the time required fore the eddies to move the distance l [10, p. 388].

This is called the Taylor's frozen-in hypothesis and can be expressed using the refractive index like this :

$$n(r,t) = n(r - Ut, 0) \tag{2.80}$$

If we now consider the correlation of the log-amplitude fluctuation χ at two different points in a plane x = L, we can obtain the following relation using the homogeneity and the Taylor's frozen-in hypothesis :

$$B_\chi(r_1, t_1; r_2, t_2) = B_\chi(L, y_1 - y_2 - U_2\tau, z_1 - z_2 - U_3\tau) \tag{2.81}$$

Where $r_1 = L\hat{x} + y_1\hat{y} + z_1\hat{z}$, $r_2 = L\hat{x} + y_2\hat{y} + z_2\hat{z}$ and $\tau = t_1 - t_2$. U_1 and U_2 are the y and z components of the wind velocity.

Using the equation 2.25 and supposing isotropy, we can write :

$$B_\chi(r_1, t_1; r_2, t_2) = 2\pi \int_0^\infty J_0(\kappa\rho) F_\chi(\kappa, 0)\kappa d\kappa \tag{2.82}$$

Where $\rho = \sqrt{(y_1 - y_2 - U_2\tau)^2 + (z_1 - z_2 - U_3\tau)^2}$.

Using now the equations 2.74 (constant C_n^2 hypothesis) and 2.77 (varying C_n^2) and considering the temporal correlation at one location $y_d = y_1 - y_2 = 0$ and $z_d = z_1 - z_2 = 0$, we obtain the two equations [13]:

$$B_\chi(L,\tau) = 2\pi^2 k^2 L \int_0^\infty d\kappa J_0(\kappa U_t \tau) \left(1 - \frac{k}{\kappa^2 L} sin \frac{\kappa^2 L}{k}\right) \Phi_n(\kappa)\kappa \tag{2.83}$$

$$B_\chi(L,\tau) = 4\pi^2 k^2 \int_0^\infty d\kappa J_0(\kappa U_t \tau) \int_0^L d\eta C_n^2(\vec{r}) \Phi_n^{(o)}(\kappa) sin^2[\frac{\kappa^2(L-\eta)}{2k}]\kappa \tag{2.84}$$

Where U_t is equal to $\sqrt{U_2^2 + U_3^2}$ and is the wind transverse velocity. The equations 2.83 and 2.84 correspond respectively to the correlation functions of the log-amplitude fluctuation when C_n^2 is constant and when C_n^2 varies.

Inserting these 2 equations in equation 2.79, we can find the final equation for the temporal frequency spectrum :

$$W_\chi(\omega) = 8\pi^2 k^2 L \int_0^\infty d\tau \cos(\omega\tau) \int_0^\infty d\kappa J_0(\kappa U_t \tau) \left(1 - \frac{k}{\kappa^2 L} sin \frac{\kappa^2 L}{k}\right) \Phi_n(\kappa)\kappa \tag{2.85}$$

$$W_\chi(\omega) = 16\pi^2 k^2 \int_0^\infty d\tau \cos(\omega\tau) \int_0^\infty d\kappa J_0(\kappa U_t \tau) \int_0^L d\eta C_n^2(\vec{r}) \Phi_n^{(o)}(\kappa) sin^2[\frac{\kappa^2(L-\eta)}{2k}]\kappa \tag{2.86}$$

We use the following equation [23] :

$$\int_0^\infty cos(\omega\tau) J_0(\kappa U_t \tau) d\tau = [(\kappa U_t)^2 - \omega^2]^{-1/2} \quad \text{for} \quad \kappa U_t > \omega \quad \text{and} \quad 0 \quad \text{otherwhise} \tag{2.87}$$

We have thus finally :

$$W_\chi(\omega) = 8\pi^2 k^2 L \int_{\omega/U_t}^\infty d\kappa \left(1 - \frac{k}{\kappa^2 L} sin \frac{\kappa^2 L}{k}\right) \Phi_n(\kappa)[(\kappa U_t)^2 - \omega^2]^{-1/2}\kappa \tag{2.88}$$

$$W_\chi(\omega) = 16\pi^2 k^2 \int_{\omega/U_t}^\infty d\kappa J_0(\kappa U_t \tau) \int_0^L d\eta C_n^2(\vec{r}) \Phi_n^{(o)}(\kappa) sin^2[\frac{\kappa^2(L-\eta)}{2k}][(\kappa U_t)^2 - \omega^2]^{-1/2}\kappa \tag{2.89}$$

Where the function $f_A(\kappa)$ is often called the filter function and has the following expression :

$$f_A(\kappa) = 1 - \frac{k}{\kappa^2 L} \sin \frac{\kappa^2 L}{k} \tag{2.90}$$

With these two equations, we have finally found the expression of the temporal frequency spectrum of the log-amplitude fluctuation. It is important to keep in mind here that the Kolmogorov spectrum $\Phi_n(\kappa)$ (see equation 2.61) is only valid for $2\pi/L_0 < \kappa < 2\pi/l_0$. We will come back to this problem later in this work.

2.6.1 The asymptotic behaviour of the temporal frequency spectrum

Before having a look at the results and at the shape of the temporal frequency spectrum of the log-amplitude fluctuation, we will first have a look at the asymptotic behaviour of the spectrum [16]. As written before, the spectrum (with the constant C_n^2 hypothesis) is defined by the following relation :

$$W_\chi(\omega) = 8\pi^2 k^2 L \int_{\omega/U_t}^\infty f_A(\kappa)\Phi_n(\kappa)[(\kappa U_t)^2 - \omega^2]^{-1/2}\kappa d\kappa \tag{2.91}$$

As it was done in [9], let be the following change of variable :

$$\kappa = (\kappa'^2 + \frac{\omega^2}{V^2})^{1/2} \tag{2.92}$$

Equivalently, we have :

$$\kappa d\kappa = \kappa' d\kappa' \tag{2.93}$$

$$d\kappa' = \frac{\kappa d\kappa}{\kappa'} = \frac{\kappa d\kappa}{(\kappa^2 - \frac{\omega^2}{U_t^2})^{1/2}} = U_t \frac{\kappa d\kappa}{(\kappa^2 U_t^2 - \omega^2)^{1/2}} \tag{2.94}$$

Substituting the equations 2.92 and 2.94 in the equation of the spectrum, we obtain the following equation :

$$W_\chi(\omega) = \frac{8\pi^2 k^2 L}{U_t} \int_0^\infty f_A((\kappa'^2 + \frac{\omega^2}{U_t^2})^{1/2}) \Phi_n((\kappa'^2 + \frac{\omega^2}{U_t^2})^{1/2}) d\kappa \tag{2.95}$$

If we now have :

$$\kappa^2(L/k) = t^2 + (\frac{\omega}{\omega_1}) \tag{2.96}$$

Where ω_1 is defined as $U_t(k/L)^{1/2}$ [9],

Doing some manipulations, we can find the following expression for the spectrum :

$$W_\chi(\omega) = \left(\frac{8\pi^2}{U_t}\right)(0.033C_n^2)k^{2/3}L^{7/6}\int_0^\infty f_A([t^2+\left(\frac{\omega}{\omega_1}\right)^2]^{1/2})[t^2+\left(\frac{\omega}{\omega_1}\right)^2]^{-11/6}dt \tag{2.97}$$

From this expression, we can find the asymptotic behaviour of this expression by taking $\omega << \omega_1$ or taking $\omega_1 >> \omega$.

When we have $\omega << \omega_1$, the expression becomes :

$$W_\chi^0(\omega) = \left(\frac{8\pi^2}{U_t}\right)(0.033C_n^2)k^{2/3}L^{7/6}\int_0^\infty f_A(t)[t]^{-11/3}dt \tag{2.98}$$

Using the definition of the filter function (equation 2.90), we obtain :

$$W_\chi^0(\omega) = \left(\frac{8\pi^2}{U_t}\right)(0.033C_n^2)k^{2/3}L^{7/6}\int_0^\infty (1-\frac{1}{t^2}\sin t^2)t^{-11/3}dt \tag{2.99}$$

Computing the integral [9], we can eventually have :

$$W_\chi^0(\omega) = \left(\frac{8\pi^2}{U_t}\right)(0.033C_n^2)k^{2/3}L^{7/6}\frac{\pi}{[2\Gamma(10/3)\sin(\frac{\pi}{3})]} \tag{2.100}$$

$$= \left(\frac{8\pi^3}{U_t}\right)(0.033C_n^2)k^{2/3}L^{7/6}\frac{1}{0.1039} \tag{2.101}$$

$$= 0.8506\frac{C_n^2k^{2/3}L^{7/6}}{U_t} \tag{2.102}$$

When we have $\omega >> \omega_1$, the filter function $f_A(\kappa) \approx 1$ since the filter function tends towards 1 when κ tends towards infinity. This can be seen in the figure 2.90.

The expression thus becomes :

$$W_\chi^\infty(\omega) = \left(\frac{8\pi^2}{U_t}\right)(0.033C_n^2)k^{2/3}L^{7/6}\int_0^\infty [t^2+\left(\frac{\omega}{\omega_1}\right)^2]^{-11/6}dt \tag{2.103}$$

$$\tag{2.104}$$

Computing the integral [9], we can eventually have :

$$W_\chi^\infty(\omega) = \left(\frac{8\pi^2}{U_t}\right)(0.033C_n^2)k^{2/3}L^{7/6}\left(\frac{\omega}{\omega_1}\right)^{-8/3}\frac{\sqrt{\pi}}{2}\frac{\Gamma(4/3)}{\Gamma(11/6)} \tag{2.105}$$

$$= 2.19\frac{C_n^2k^{2/3}L^{7/6}}{V}\left(\frac{\omega}{\omega_1}\right)^{-8/3} \tag{2.106}$$

With these equations [1], we have computed the two asymptotes of the temporal frequency spectrum of the log-amplitude fluctuation when C_n^2 is supposed to be constant.

The transition frequency is defined as the frequency where the two asymptotes intersect. Therefore, ω_t can be found thanks to the following relation :

$$W_\chi^\infty(\omega_t) = W_\chi^0(\omega_t) \tag{2.107}$$

With some simplifications, it can be shown that the final expression for the transition frequency [14] is :

$$\omega_t = 1.43 U_t \left(\frac{k}{L}\right)^{1/2} \tag{2.108}$$

A similar reasoning can be done in the case where C_n^2 varies along the link and it can be shown that ω_t keeps the same expression in that case.

2.7 The hypothesis and assumptions of the temporal frequency spectrum

To finish this chapter, it could be good to remind all the hypotheses that where made in order to obtain the two following expressions for the temporal frequency spectrum of the log-amplitude fluctuation.

$$W_\chi(\omega) = 8\pi^2 k^2 L \int_{\omega/U_t}^{\infty} \left(1 - \frac{k}{\kappa^2 L} sin \frac{\kappa^2 L}{k}\right) \Phi_n(\kappa)[(\kappa U_t)^2 - \omega^2]^{-1/2} \kappa d\kappa \tag{2.109}$$

$$W_\chi(\omega) = 16\pi^2 k^2 L \int_{\omega/U_t}^{\infty} d\kappa \int_0^L d\eta C_n^2(\vec{r}) \Phi_n^{(o)}(\kappa) sin^2[\frac{\kappa^2 (L-\eta)}{2k}][(\kappa U_t)^2 - \omega^2]^{-1/2} \kappa \tag{2.110}$$

The hypotheses and assumptions which allowed us to obtain these two equations are :

1. Local isotropy
2. Local homogeneity
3. Constant/Varying C_n^2
4. Constant U_t
5. Wind fluctuation $V_f = 0$
6. Monochromatic planar wave of the following form Ae^{ikx}
7. Inertial subrange and Kolmogorov spectrum
8. Frozen medium
9. $|\nabla \psi_l| << k$: smallness of changes of ψ_l over distances of the order of wavelength (as a reminder Re $\psi = A$ and Im $\psi = S$). This means that the amplitude and phase of the wave cannot change too much within a distance which is smaller than λ.
10. weak fluctuation $|n_l| << 1$
11. wavelength smaller than l_0 : $\lambda << l_0$

12. no charges in the atmosphere

13. the magnetic permeability is constant

It is very important to keep these hypotheses in mind. Moreover, in this thesis, our wave is not an horizontal wave since the angle of elevation is equal to 3°. However, all the computations which have been done are still correct. We just have to make a rotation of the axes.

Now that we have found the expression of the temporal frequency spectrum of the log-amplitude fluctuation and cited all the hypotheses which have been made, we will try to find the different parameters needed to compute the spectrum such as the C_n^2 and the transverse wind speed U_t. After that, we will be able to compare our spectrum models with real measurements.

Therefore, in the next chapter, we will present the meteorological data which were used to compute the different parameters and their organisation. We will also explain where our scintillation measurements come from and their characteristics.

Chapter 3

Scintillation measurements and meteorological data

In this chapter, we are going to present the scintillation measurements and explain when and how they were made. We will also explain where the meteorological data come from and how they were used.

3.1 The meteorological data

As it was said in the introduction, we use the meteorological data from the station of Svalbard which is situated near the north pole. The meteorological data come from the Norwegian Meteorological Institute and are freely available on the website http://thredds.met.no.

The meteorological previsions are done every 6 hours and are made according to a 4-dimensions mesh. The 4 dimensions are longitude, latitude, atmosphere hybrid sigma pressure and time. Therefore, the data are not given in function of the height but in function of pressure layers. In order to have the height, we compute the geopotential corresponding to the pressure. More informations about the geopotential and the following equations can be found in [5].

The geopotential can be expressed thanks to the following expression :

$$\phi_{k+1/2} = \phi_s + \sum_{j=k+1}^{NLEV} R_{DRY}(T_v)_j \log\left(\frac{p_{j+1/2}}{p_{j-1/2}}\right). \tag{3.1}$$

Where NLEV is the number of “pressure” layers (the 1/2 terms correspond to half-layers), T_v is the virtual temperature, p is the pressure and R_{DRY} is the gas constant of dry air.

From the geopotential, we can compute the geopotential height by dividing the standard gravity.

$$h = \frac{\phi}{g_0} \tag{3.2}$$

Using the two equations 3.2 and 3.1, it is possible to find the height of the meteorological data.

Since the meteorological data are predicted according to pressure layers, the height difference between points at the same position will not be constant. This can be seen in figure 3.1 where we have the X component of the wind velocity in function of the height.

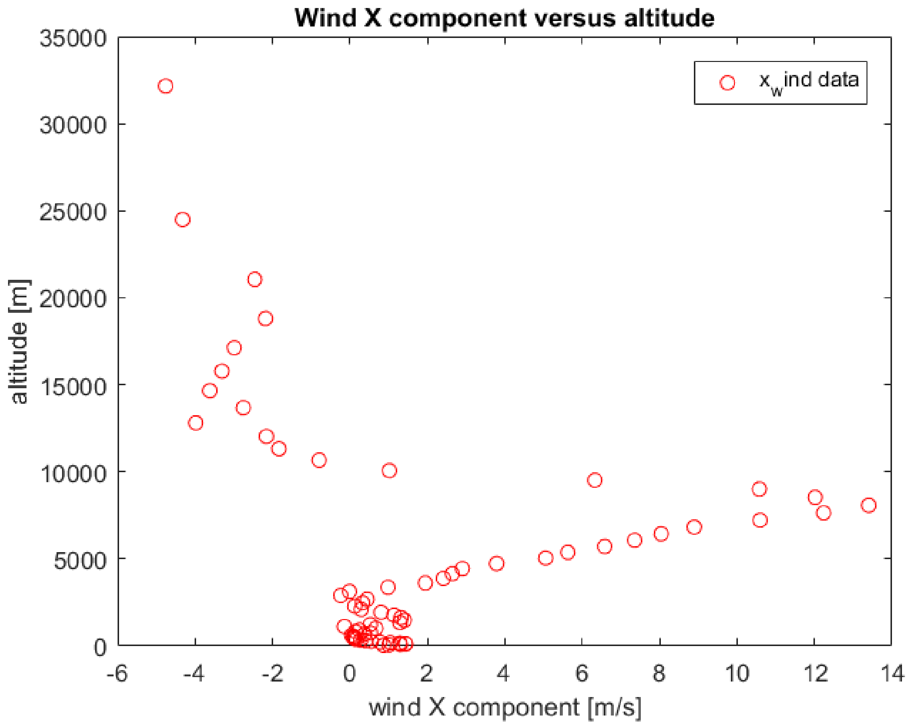

Figure 3.1 – Position of the data in function of the altitude

As we can see, most of the data are available at low altitude. If we look at higher altitude, we see that the number of points decreases and that we lose precision. In total, we have 65 points along the height.

From these points, we are going to make interpolations in order to have the data at regular height step. In this thesis, we are going to make interpolations so as to have data every 25 m. Also, as we will explain later, we will not need data above 2000 m. This has been done for the X wind component in the figure 3.2.

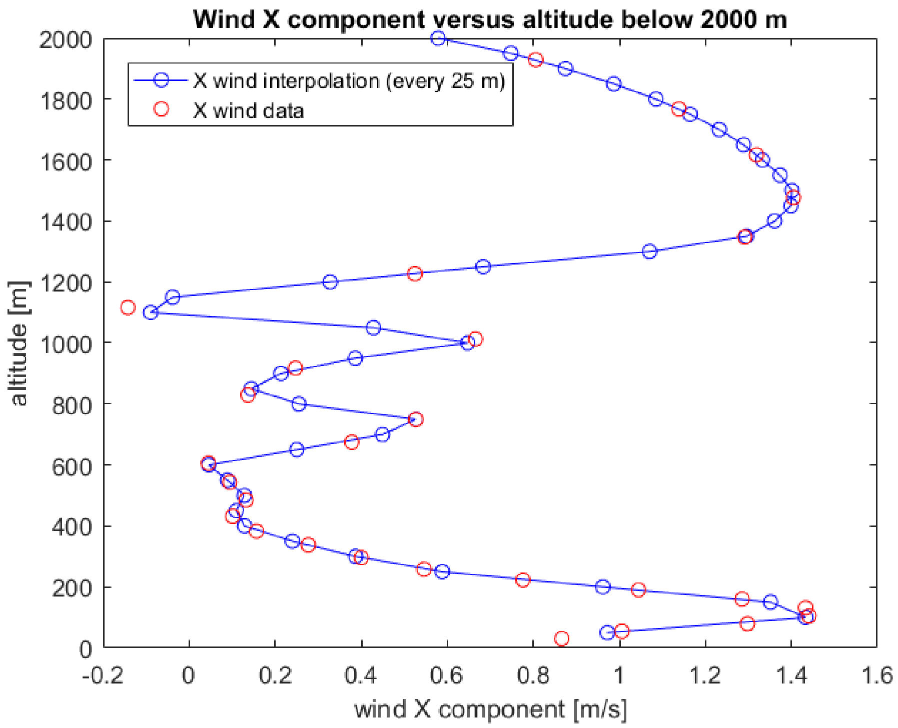

Figure 3.2 – Data interpolation in function of the altitude

To have the data every 25 m as in the figure 3.2, a shape-preserving piecewise cubic interpolation has been done.

In the horizontal plan, the longitude and latitude coordinates are separated from each other by a distance of 2.5 km. We can see the horizontal mesh in the figure 3.3.

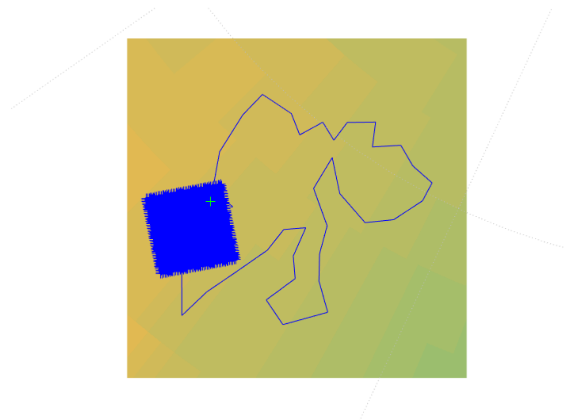

Figure 3.3 – Horizontal mesh of the Svalbard Island

In the figure 3.3, we can see in blue the horizontal mesh which represents the points where we can find the data. The cyan cross represents the location of the antenna.

Finally, the data are function of the time and are available every hour. In this thesis, the most important data that will be used are the pressure, the temperature, the wind velocity components and the specific humidity.

3.2 The scintillation measurements

In the previous chapter, we built a spectrum model (with constant or varying C_n^2) in order to compare it with scintillation measurements.

These scintillation measurements were made in March and July 2016 at the Svalbard station. Therefore, we know the scintillation signals during these months. In the figure 3.4, we can see the scintillation signal of the 3^{th} of March.

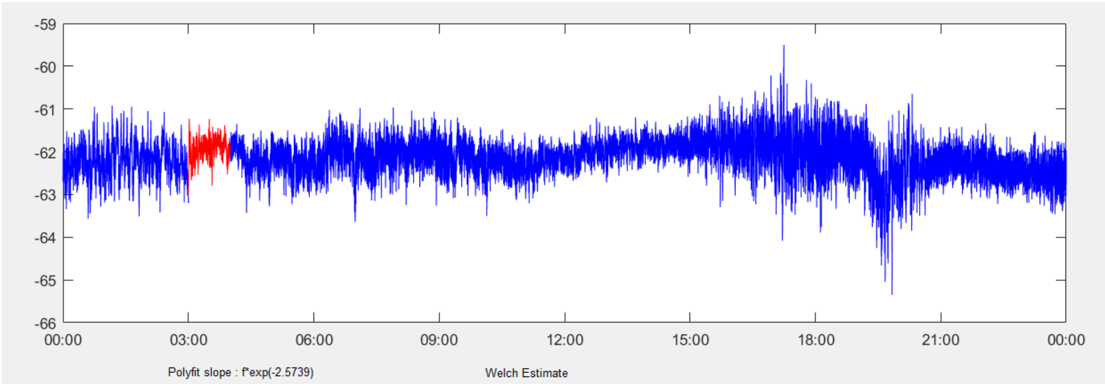

Figure 3.4 – Scintillation signal on the 3^{th} of March

From the scintillation signal, the Power spectrum density estimate has been computed via Welch's method in Matlab. We will not go here into the details of the Welch algorithm. In the figure 3.5, we can see the PSD estimate on the 3^{th} of March based on the 3 a.m - 4 a.m time interval. This interval corresponds to the red part of the signal in figure 3.4.

Moreover, it is important to know here that the DC component of the signal was not removed when computing the PSD. Later in this work, we will always remove the DC component of the signal since the scintillation phenomenon only concerns the amplitude fluctuation of the signal.

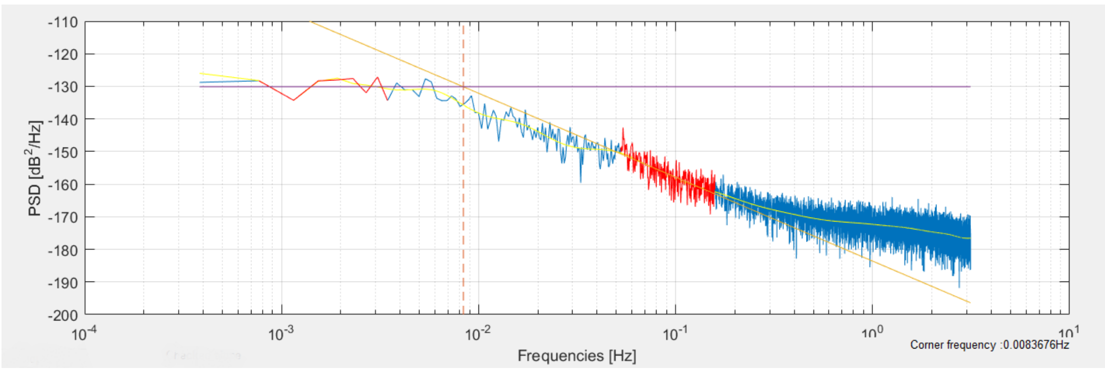

Figure 3.5 – Scintillation signal on the 3^{th} of March

In the figure 3.5, we can see several things. Firstly, the scintillation PSD can be seen in blue. As we can see it, the scintillation PSD has a very characteristic shape. At low frequencies, the PSD is approximately constant. However, after what is called the transition frequency, the PSD begins to decreases approximately linearly (we are in logarithmic scale). This corner frequency (vertical dashed line) has been computed doing a variance-based method which will not be explained here and gives us an indication of the place where the PSD begins to decrease linearly.

In yellow, we can see a polyfit approximation which show sus an approximation of the scintillation PSD. Finally, the purple horizontal line and the orange oblique line show us the approximated asymptotical behaviour of the scintillation PSD. These asymptotes have been computed on the basis of the two red parts of the PSD in figure 3.5.

Now that we have explained where the meteorological data and the measurements comes from and how they are organised, we will try to compute the different parameters which are needed for our scintillation spectrum models.

Chapter 4

Characterisation of the turbulent zone and its parameters

In this chapter, we are going to determine different parameters such as the length L of the link in the turbulent zone, the transverse wind speed U_t and the C_n^2. To find their values, we will have a look at the altitude profiles of U_t and C_n^2.

4.1 The structure constant C_n^2 : definition and profiles

In order to compute the temporal frequency spectrum (see equations 2.109 and 2.110), we first need to find the value of the structure constant C_n^2 (which is going to be considered as a constant or as a variable according to the considered spectrum).

4.1.1 C_n^2 definition

According to Kolmogorov's law (see equation 2.55), the structure function of the refractive index in the inertial sub-range has the following expression :

$$D_n(r) = C_n r^{\frac{2}{3}} \tag{4.1}$$

By definition of the structure function (see 2.6), we can have :

$$D_n(r+\delta, r) = D_n(r) =< (n(r+\delta) - n(r))^2 >> \tag{4.2}$$

Using the two previous equations, we can find an expression for C_n^2 in the inertial sub-range [16].

$$C_n^2 = \frac{< (n(r+\delta) - n(r))^2 >}{\delta^{2/3}} \tag{4.3}$$

It is important to know that there are several ways to compute the refractive structure constant and they do not always give the same results [6],[7]. In our case, we took this one because it has the advantage of being precise and simple to compute.

Since we have available of the highest precision in the Z direction in our 4D mesh (25 m precision in the vertical plan instead of 2500 m in the horizontal plan), we have made the following transformation :

$$C_n^2(z) = \frac{< (n(z+dz) - n(z))^2 >}{dz^{2/3}} \tag{4.4}$$

We can make this transformation because of the isotropy hypothesis.

However, in order to have the C_n^2, we need to compute the refractive index. This is possible thanks to the following equation :

$$N = 77.6\frac{P}{T} - 5.6\frac{e}{T} + 3.75 \times 10^5 \frac{e}{T^2} \qquad [6][17] \tag{4.5}$$

Where P is the total atmospheric pressure (in hPa), T is the absolute temperature (in K) and e is the water vapour pressure and can be computed from the pressure and the specific humidity.

Since the atmospheric pressure, the temperature and the specific humidity are available in the meteorological data from the Norwegian Meteorological Institute, it is thus possible to compute the refractive index via the equation 4.5. Once the refractive index is obtained, we can find the C_n^2 thanks to the equation 4.4.

4.1.2 C_n^2 profiles

Using the formula 4.4, we can compute the profiles of the C_n^2 along the altitude. Starting from theses profiles we will find where is approximately the turbulent zone. Indeed, one criteria to delimit the turbulent zone (the whole atmosphere is not turbulent) is to look at the values of the C_n^2. Therefore, the turbulent zone will be situated in the zone where the C_n^2 has the largest values.

Indeed, as you can see it the equation of the spectrum (see equations 2.109 and 2.110), the C_n^2 value is really important in the integral. The highest the value of the C_n^2, the largest will be its contribution to the integral and thus to the spectrum. Therefore, since the C_n^2 generally varies along two orders of magnitude (between 10^{-12} and 10^{-14}), we will only take the highest values. For this work, we have decided to take values above 10^{-13} only because with lower values the contribution to the integral is really smaller. By taking only the value above 10^{-13}, we will determine the depth of the turbulent zone.

Therefore, in the next figures, we can see the C_n^2 profiles in July 2016 at different times of the day. For the sake of clarity, we have not put all the graphs (of the whole month) since the amount of information is huge but only a few of them.

Each figure shows the C_n^2 profile at different points of the earth-satellite link. Therefore, we have chosen to have a look at the profiles at 0, 0.5, 1, 1.5, 2, 2.5 and 3 km from the antenna (see figure 1.1). In the next figures, we can see the C_n^2 profile on the 1^{st} of July at different times of the day (see figure 4.1). A vertical line corresponding to 10^{-13} has always been drawn as well.

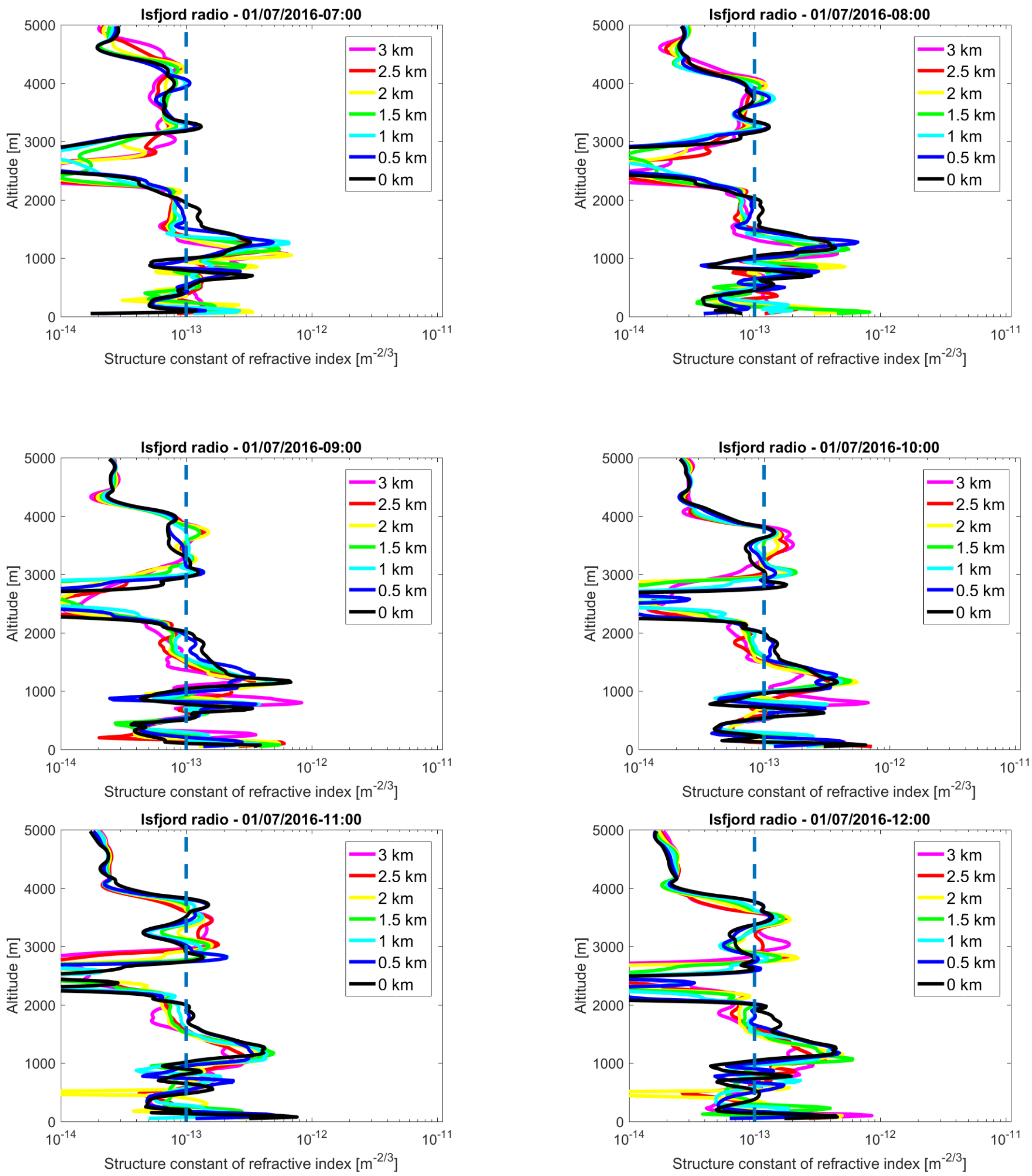

Figure 4.1 – C_n^2 profile on 1^{st} of July between 7 a.m and 12 a.m

The first thing to say about the profiles of the 1^{st} of July is that they do not change a lot between 7 a.m and 12 a.m. The general form stays quite the same hour after hour. We also see that the C_n^2 has values above 10^{-13} between 0 and 2 km and between 3 and 4 km approximately.

We will now have a look at the profiles on other days. Since the profiles do not seem to change a lot in 6 hours, we will not take more than one profile a day.

In the figures 4.2, we can see the profiles of the following days : 1, 3, 5, 7, 9, 11, 12, 14, 16, 18, 19, 21, 22, 24, 26, 28, 29 and 30^{th} of July 2016.

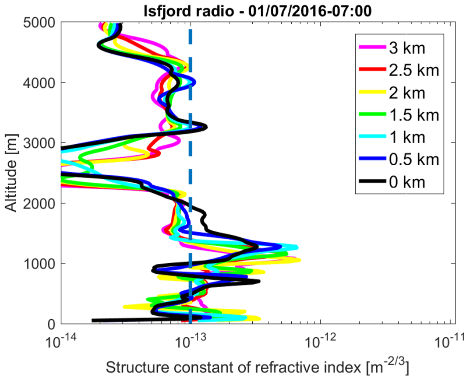
Isfjord radio - 01/07/2016-07:00
Altitude [m]
Structure constant of refractive index [m^-2/3]
3 km
2.5 km
2 km
1.5 km
1 km
0.5 km
0 km

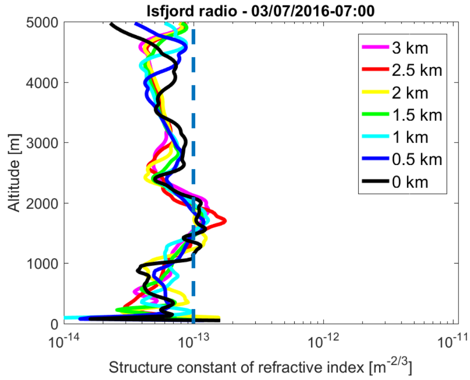
Isfjord radio - 03/07/2016-07:00
Altitude [m]
Structure constant of refractive index [m^-2/3]
3 km
2.5 km
2 km
1.5 km
1 km
0.5 km
0 km

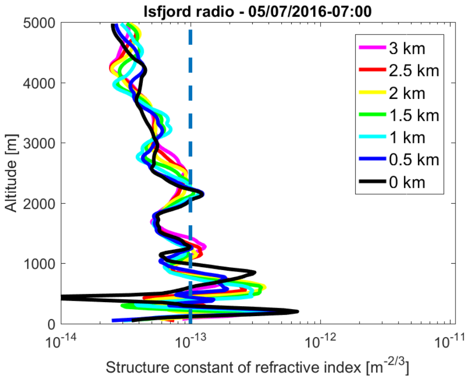
Isfjord radio - 05/07/2016-07:00
Altitude [m]
Structure constant of refractive index [m^-2/3]
3 km
2.5 km
2 km
1.5 km
1 km
0.5 km
0 km

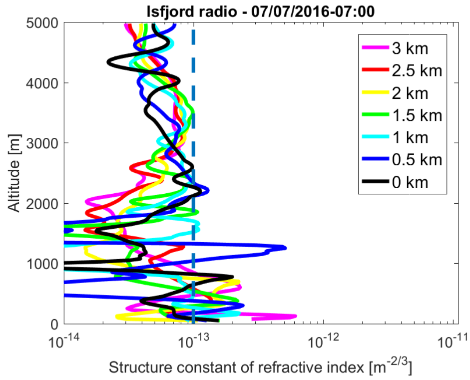
Isfjord radio - 07/07/2016-07:00
Altitude [m]
Structure constant of refractive index [m^-2/3]
3 km
2.5 km
2 km
1.5 km
1 km
0.5 km
0 km

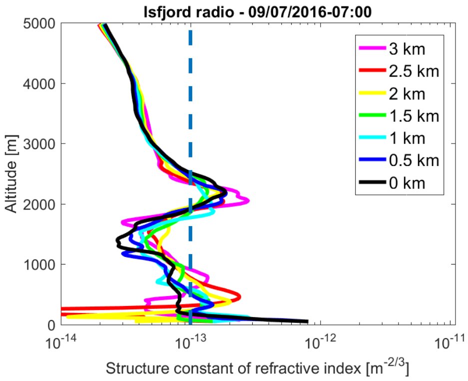
Isfjord radio - 09/07/2016-07:00
Altitude [m]
Structure constant of refractive index [m^-2/3]
3 km
2.5 km
2 km
1.5 km
1 km
0.5 km
0 km

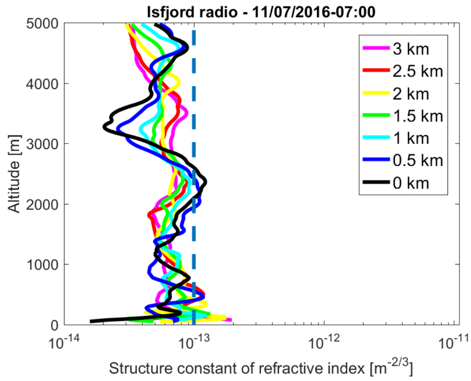
Isfjord radio - 11/07/2016-07:00
Altitude [m]
Structure constant of refractive index [m^-2/3]
3 km
2.5 km
2 km
1.5 km
1 km
0.5 km
0 km

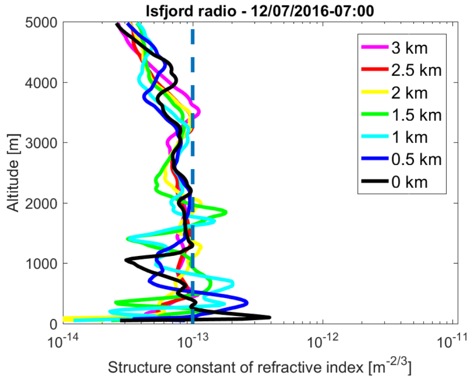
Isfjord radio - 12/07/2016-07:00
Altitude [m]
Structure constant of refractive index $[m^{-2/3}]$
3 km
2.5 km
2 km
1.5 km
1 km
0.5 km
0 km

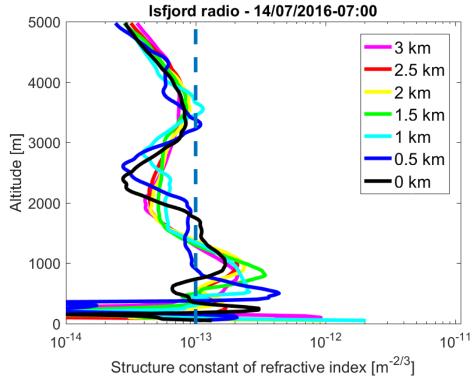
Isfjord radio - 14/07/2016-07:00
Altitude [m]
Structure constant of refractive index $[m^{-2/3}]$
3 km
2.5 km
2 km
1.5 km
1 km
0.5 km
0 km

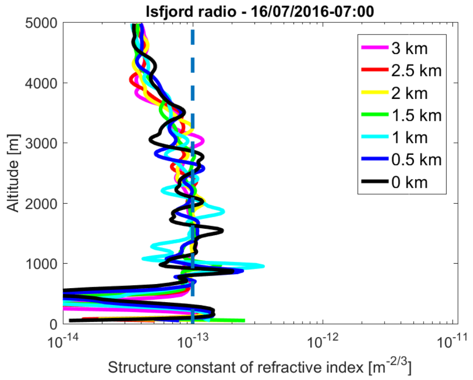
Isfjord radio - 16/07/2016-07:00
Altitude [m]
Structure constant of refractive index $[m^{-2/3}]$
3 km
2.5 km
2 km
1.5 km
1 km
0.5 km
0 km

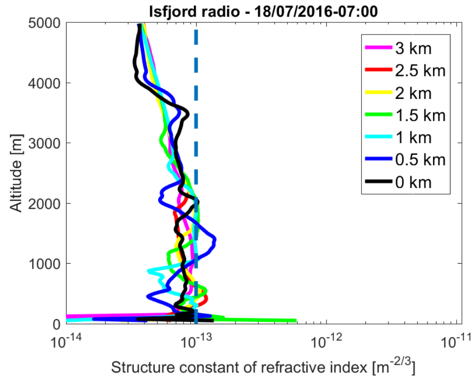
Isfjord radio - 18/07/2016-07:00
Altitude [m]
Structure constant of refractive index $[m^{-2/3}]$
3 km
2.5 km
2 km
1.5 km
1 km
0.5 km
0 km

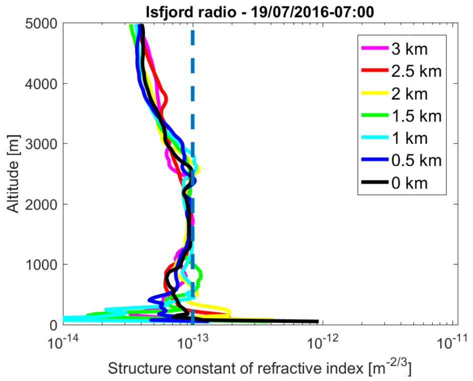
Isfjord radio - 19/07/2016-07:00
Altitude [m]
Structure constant of refractive index $[m^{-2/3}]$
3 km
2.5 km
2 km
1.5 km
1 km
0.5 km
0 km

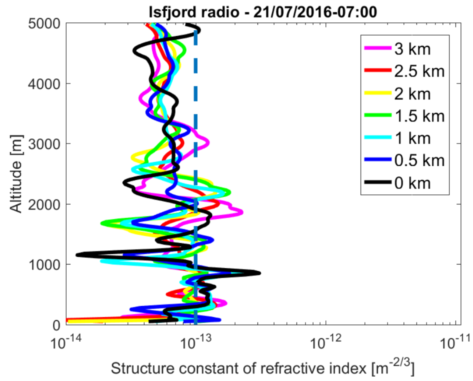
Isfjord radio - 21/07/2016-07:00
Altitude [m]
Structure constant of refractive index $[m^{-2/3}]$
3 km
2.5 km
2 km
1.5 km
1 km
0.5 km
0 km

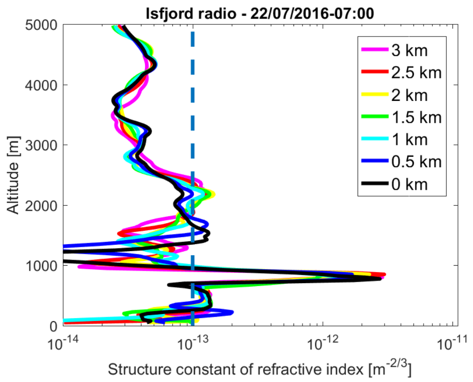
Isfjord radio - 22/07/2016-07:00
Altitude [m]
Structure constant of refractive index $[m^{-2/3}]$
3 km
2.5 km
2 km
1.5 km
1 km
0.5 km
0 km

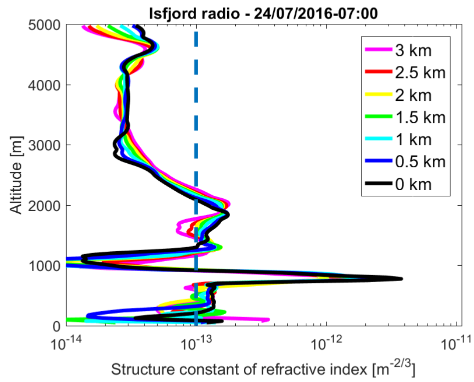
Isfjord radio - 24/07/2016-07:00
Altitude [m]
Structure constant of refractive index $[m^{-2/3}]$
3 km
2.5 km
2 km
1.5 km
1 km
0.5 km
0 km

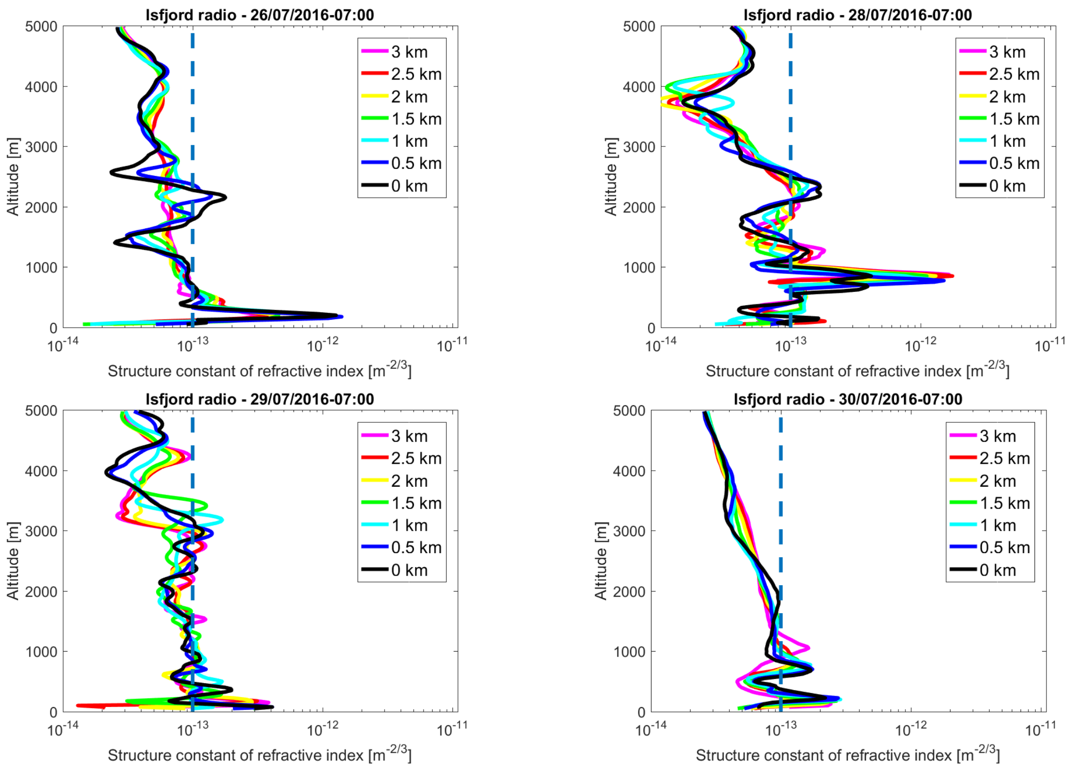

Figure 4.2 – C_n^2 profiles in most days of July at 7 a.m

From the profiles at figure 4.2, we can see that in general the value of the C_n^2 is the highest near the ground. After about 2-2.5 km, its value tends to decrease below 10^{-13}. Therefore, 2 km would be a good approximation for the turbulent zone depth.

4.2 The turbulent zone depth and the length of the link in the turbulent zone

In order to be the most accurate in our choice of turbulent zone depth, we have computed the last altitude at which the C_n^2 profiles are equal to 10^{-13} before decreasing. It can be seen in table 4.1. Based on this table and the C_n^2 profiles from figure 4.2, we will choose a final value for the turbulent zone depth [8].

	Last altitude [m] at which the C_n^2 crosses 10^{-13}						
Distance from antenna [m]	**3 km**	**2.5 km**	**2 km**	**1.5 km**	**1 km**	**0.5 km**	**0 km**
1st	1250	1375	1325	1350	1350	4050	3325
2sd	3200	3350	3450	3450	3550	3575	3525
3th	2100	1925	1900	1950	1975	1825	2075
4th	2575	2600	2775	2900	3050	3325	3325
5th	1400	1300	1250	2225	2250	2225	2200
6th	850	1000	1025	1050	1000	4325	1050
7th	825	575	725	1875	1700	2325	2250
8th	2300	2350	2350	2200	2175	2025	2000
9th	2325	2350	2400	2475	2425	2425	2500
10th	1500	1625	1350	1425	1500	1475	1000
11th	125	625	400	225	175	2400	2575
12th	3600	/	2050	1950	1750	525	1300
13th	3300	3375	3350	2750	2675	2700	2700
14th	1275	1350	1350	1275	3650	3375	1725
15th	1775	1675	1775	1825	1875	2050	1275
16th	3125	2425	2175	2825	2450	2650	2850
17th	3750	3575	3500	3350	3275	3100	3050
18th	/	600	625	2050	1900	1650	2050
19th	1725	200	2650	1000	2800	2425	100
20th	2400	2375	1050	1525	1600	1650	1650
21th	3150	2200	2400	2375	2250	2025	4925
22th	2425	2350	2275	2275	2250	1775	1650
23th	2350	2375	2400	2425	2450	1500	1600
24th	2250	2200	2175	2150	2150	2100	2075
25th	2200	2200	2225	2250	2325	2375	2150
26th	500	625	625	650	600	2350	2250
27th	2525	2425	2300	2225	2175	2025	2000
28th	2225	2275	2375	2425	2550	2575	2475
29th	2825	2950	3000	3475	3275	3050	3150
30th	1275	1100	1000	975	975	875	800
31th	1050	975	900	875	850	950	950
Mean of July	2005.6	1816.9	1908.1	1992.7	2096	2312.9	2146.8

Table 4.1 – Highest altitude at which C_n^2 is equal to 10^{-13} on July at 7 a.m

From this table and the profiles, we can see that the last value at which C_n^2 is equal to 10^{-13} is most of the time around 2000 m. It is confirmed by the mean values at the different points of the earth-satellite link which are all between 1800 and 2315 m. Therefore, we will choose a turbulent zone depth **h** of 2000 m.

4.3 The link length in the turbulent zone and the Fresnel zones

According to the chosen turbulent zone depth, the link length in the turbulent zone will be different. As a reminder, we chose in the previous section that the turbulent zone depth was 2000 m.

$$h = 2000m \tag{4.6}$$

Since we have an elevation angle of about 3 °, the link length in the turbulent zone will be equal to :

$$L = \frac{h}{sin\ 3°} = 38\ 215m \tag{4.7}$$

The length of the link in the turbulent zone is important for several reasons. First, it has an importance regarding the amplitude of the temporal frequency spectrum (see equations 2.109 and 2.110). Also, it has a big influence on the corner frequency of the temporal spectrum (see equation 2.108).

Indeed, according to the length of link in the turbulent zone, eddies of different sizes will be involved in computation of the spectrum and this will affect the corner frequency. To have a better idea of which eddies are involved, we will consider a basic situation as showed in the figure 4.3.

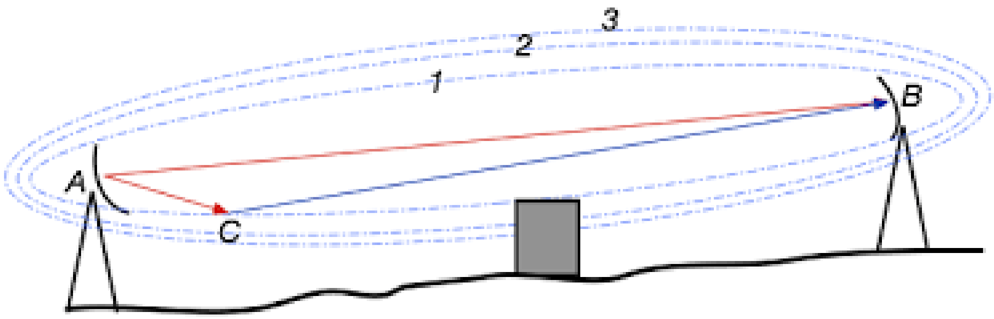

Figure 4.3 – Communications between two antennas with an obstacle [12]

In the figure 4.3, we can see two antennas which are communicating with each other with an obstacle in between. This obstacle will cause an attenuation of the amplitude of the wave. In our situation, the eddies can be seen as obstacles and these are what will cause attenuation.

Suppose the obstacle is at such a position that there is a phase shift of $n\frac{\lambda}{2}$, this can be modelled by the following equation :

$$AC + BC = AB + n\frac{\lambda}{2} \tag{4.8}$$

Where n is a natural number and is called the number of the Fresnel zone.

The n^{th} fresnel zone is thus defined as the volume corresponding to a phase shift of $n\frac{\lambda}{2}$. Therefore, if there is an obstacle inside the first Fresnel zone, the phase shift generated will be below $\frac{\lambda}{2}$. If the obstacle is inside the second Fresnel zone and not the first one, then the phase shift generated will be between $\frac{\lambda}{2}$ and $\frac{2\lambda}{2}$. In general, the attenuation in a communication is mostly due to the first Fresnel zone [12].

It can be shown that the radius of the n^{th} Fresnel zone [20] has the following radius :

$$r_n = \sqrt{\frac{n\lambda d_1 d_2}{d_1 + d_2}} \tag{4.9}$$

Where d_1 and d_2 are respectively the distance emitter-obstacle and obstacle-receiver along the link axis.

In our case, we analyse an earth-satellite communication so we can make d_2 (the obstacle-satellite distance along the link axis) tend towards infinity.

$$lim_{d_2 \to \infty} r_n = \sqrt{n\lambda d_1 \frac{1}{\frac{d_1}{d_2} + 1}} = \sqrt{n\lambda d_1} \tag{4.10}$$

Physically, it is the first Fresnel volume where the attenuations are the strongest.

The radius of the first Fresnel zone is thus :

$$r_1 = \sqrt{\lambda d_1} = \sqrt{\lambda L} \tag{4.11}$$

Since L is equal to 38 215 m and since the antenna emits 19 GHz waves, we can find the radius of the first Fresnel zone.

The wavelength has the following value :

$$\lambda = \frac{c}{f} = 0.0158m \tag{4.12}$$

The radius of the first Fresnel zone is thus :

$$r_1 = \sqrt{0.0158 * \frac{2000}{sin\ 3^\circ}} = 24.5722\ m \tag{4.13}$$

The first Fresnel zone has thus a radius of 24.57 m. This value is really important for the computation of the time-frequency spectrum.

4.4 The radius of the first Fresnel zone : case study

In chapter 2, we obtained two equations for the temporal frequency spectrum (see equations 2.109 and 2.110). Let us write them again below :

$$W_\chi(\omega) = 8\pi^2 k^2 L \int_{\omega/U_t}^{\infty} f_A(\kappa)\Phi_n(\kappa)[(\kappa U_t)^2 - \omega^2]^{-1/2}\kappa d\kappa \tag{4.14}$$

$$W_\chi(\omega) = 16\pi^2 k^2 L \int_0^{\infty} d\kappa \int_{\omega/U_t}^{L} d\eta C_n^2(\vec{r})\Phi_n^{(o)}(\kappa) f_v(\kappa)][(\kappa U_t)^2 - \omega^2]^{-1/2}\kappa \tag{4.15}$$

Where $\Phi_n(\kappa)$ is the Kolmogorov spectrum (see equation 2.61). $f_A(\kappa)$ and $f_v(\kappa)$ have the following expressions :

$$f_A(\kappa) = 1 - \frac{k}{\kappa^2 L} \sin \frac{\kappa^2 L}{k} \tag{4.16}$$

$$f_v(\kappa) = sin^2[\frac{\kappa^2(L-\eta)}{2k}] \tag{4.17}$$

As we can see, we have the product $f_A(\kappa) \times \Phi_n(\kappa)$ in equation 4.14 and $f_v(\kappa) \times \Phi_n(\kappa)$ in equation 4.15.

However, the Kolmogorov spectrum is only valid when $2\pi/L_0 < \kappa < 2\pi/l_0$. This could be problematic since we have to make an integration over κ from ω/U_t to ∞. Fortunately, this problem is in some cases resolved due to the shape of the filter function

$f_A(\kappa)$(analogous reasoning with $f_v(\kappa)$).

Indeed, if we look at the shape of the filter function in the figure 4.4, we can see that before $\sqrt{\frac{2\pi^2}{\lambda L}}$, the filter function is really small (at this value, the filter function is equal to 1).

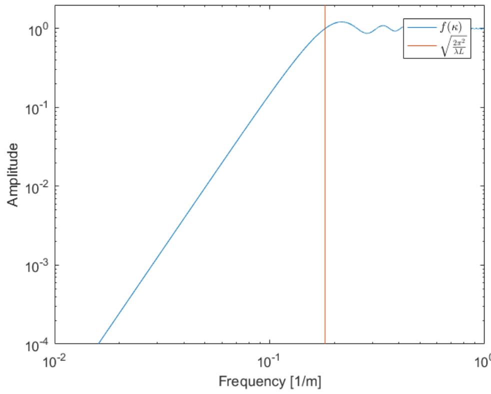

Figure 4.4 – Filter function

We define now a characteristic scale which is equal to $\kappa_0 \approx \frac{2\pi}{\sqrt{\lambda L}}$. It corresponds to $L_\lambda = \sqrt{\lambda L}$ which is the radius of the first Fresnel zone. According to the value of κ, the filter function will have the following expressions :

$$f(\kappa) = \begin{cases} 1 & \kappa >> \kappa_0 \\ \frac{\kappa^4 L^2}{6k^2} & \kappa << \kappa_0 \end{cases} \tag{4.18}$$

Based on the equation 2.61, it can be shown that the Kolmogorov spectrum has the following shape (see figure 4.5).

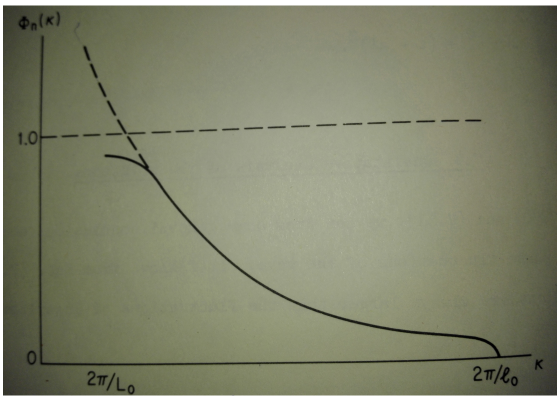

Figure 4.5 – Kolmogorov spectrum [18, p. 138]

As we can see in the figure 4.5, the Kolmogorov spectrum is only defined after $\kappa_{L0} = 2\pi/L_0$. But below this frequency, the isotropy hypothesis is no longer satisfied and the 3D spatial frequency spectrum is thus undefined.

If we now go back to the product of $f(\kappa) * \Phi(\kappa)$, we can find 3 situations which we can see in the figure 4.8.

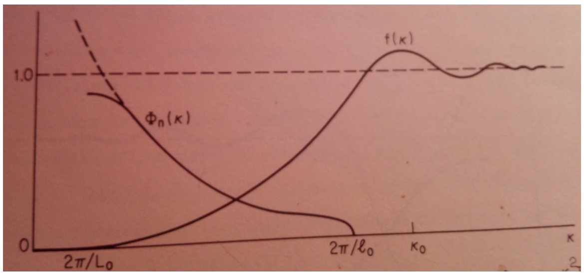

Figure 4.6 – Situation 1

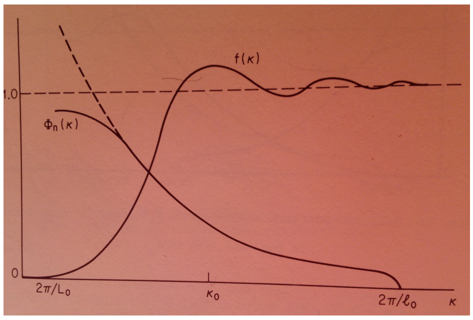

Figure 4.7 – Situation 2

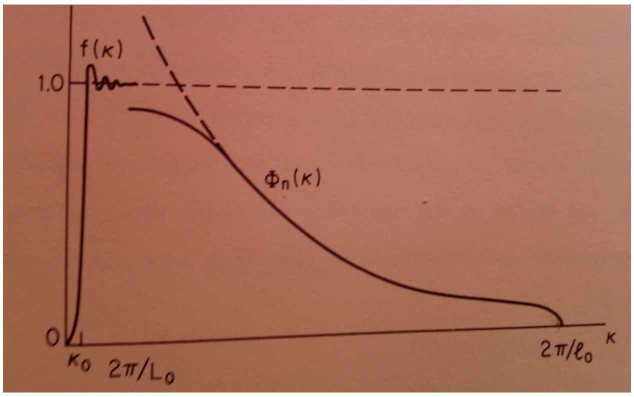

Figure 4.7 – Situation 3

Figure 4.8 – Kolmogorov spectrum and filter function for different κ_0 [18, pp. 139-141]

These three situations correspond to the three following cases :

1. $\frac{1}{\sqrt{\lambda L}} > \frac{1}{l_0}$ Situation 1
2. $\frac{1}{L_0} < \frac{1}{\sqrt{\lambda L}} < \frac{1}{l_0}$ Situation 2
3. $\frac{1}{\sqrt{\lambda L}} < \frac{1}{L_0}$ Situation 3

In the two first situations 4.6 and 4.7, there is no problem with the integral because the filter function is very small below $2\pi/L_0$. Therefore, even if $\Phi(\kappa)$ is unknown below this value, it does not matter because the product is almost equal to 0.

However, in the third situation, the undefined part of $\Phi(\kappa)$ can not be forgotten and it will have a contribution in the integral which cannot be neglected.

To solve this problem, we will use the Von Karman spectrum which extends the spectrum below $2\pi/L_0$ (see equation 4.19) and the filter function will be put to 1.

$$\Phi_n^{(vk)}(\kappa) = 0.033C_n^2(\kappa^2 + \frac{1}{L_0^2})^{-11/6} exp(-\kappa^2/\kappa_m^2) \tag{4.19}$$

Therefore, when $\frac{1}{\sqrt{\lambda L}} < \frac{1}{L_0}$, the spectrum will be :

$$W_\chi(\omega) = 8\pi^2 k^2 L \int_{\omega/U_t}^{\infty} \Phi_n^{(vk)}(\kappa)[(\kappa U_t)^2 - \omega^2]^{-1/2}\kappa d\kappa \tag{4.20}$$

The exact same reasoning can be done with $f_v(\kappa)$ when C_n^2 is not supposed to be constant. In this case, the temporal frequency spectrum will have the following equation :

$$W_\chi(\omega) = 16\pi^2 k^2 L \int_{\omega/U_t}^{\infty} d\kappa \int_0^L d\eta C_n^2(\vec{r})\Phi_n^{(vko)}(\kappa)[(\kappa U_t)^2 - \omega^2]^{-1/2}\kappa \tag{4.21}$$

When $\frac{1}{\sqrt{\lambda L}} > \frac{1}{L_0}$, the spectrum will be as it was computed before.

Looking at the asymptotic behaviour of equations 4.20 and 4.21, it is possible to show that when $\frac{1}{\sqrt{\lambda L}} < \frac{1}{L_0}$, the transition frequency will have the following expression :

$$\omega_t = \frac{U_t}{2\pi L_0} \tag{4.22}$$

Now that we have distinguished these two cases and that we have characterized the turbulent zone, we will investigate the last important parameter : the transverse wind speed.

4.5 The transverse wind speed : computation and profiles

In this section we will compute the transverse wind speed from the meteorological data of the Norwegian Meteorological institute.

4.5.1 Computation of the transverse speed

From the meteorological data, we have available the wind speed in three directions.

- $\vec{u}$ (Towards East)
- $\vec{v}$ (Towards North)
- $\vec{w}$ (Upwards)

In order to compute the transverse speed, we need to adapt the axes in such a way that they become aligned with the direction of the antenna. Once this is done, we will just have to take the perpendicular component of the wind speed in order to have the transverse speed.

We know that our antenna in Svalbard has a 183°azimuth. The situation can be seen in the following picture 4.9. For clarity purposes, this drawing is not to scale.

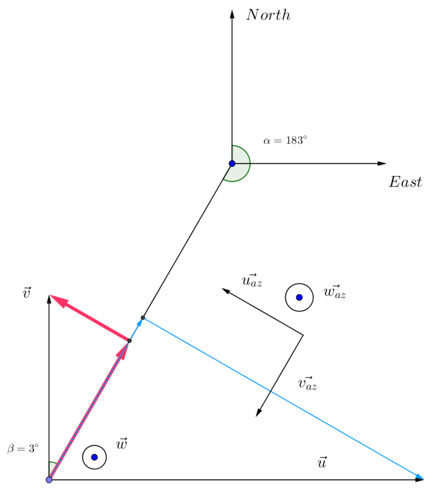

Figure 4.9 – Azimuth plan

Thanks to the 183°azimuth, we can deduce that the antenna goes towards the south-west. Based on the figure 4.9, we can deduce the horizontal transverse and parallel speed ($\vec{u_{az}}$ and $\vec{v_{az}}$).

$$\vec{u_{az}} = -\vec{u}\cos(3°) + \vec{v}sin(3°) \tag{4.23}$$

$$\vec{v_{az}} = -\vec{u}\sin(3°) - \vec{v}\cos(3°) \tag{4.24}$$

$$\vec{w_{az}} = \vec{w} \tag{4.25}$$

Now that we have considered the horizontal plane, we can consider the vertical plan with the 3 degree elevation angle (see figure 4.10). Again, it is important to know that this drawing is not to scale.

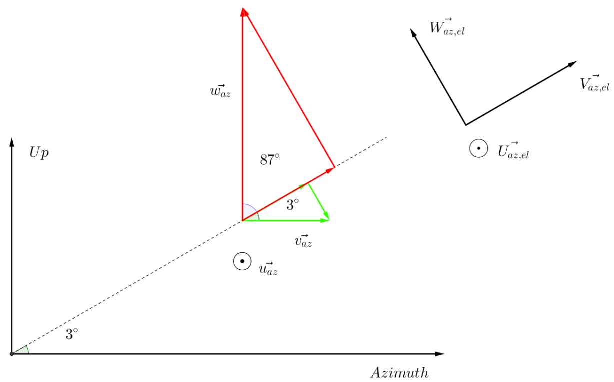

Figure 4.10 – Vertical plan

Based on the figure, we can deduce that :

$$\vec{W_{az,el}} = \vec{w_{az}}\sin(87°) - \vec{v_{az}}\sin(3°) \tag{4.26}$$

$$\vec{V_{az,el}} = \vec{w_{az}}\cos(87°) + \vec{v_{az}}\cos(3°) \tag{4.27}$$

$$\vec{U_{az,el}} = \vec{u_{az}} \tag{4.28}$$

Eventually, we can find the transverse wind speed using Pythagore 's theorem.

$$\vec{U_t} = \sqrt{\vec{U_{az,el}}^2 + \vec{W_{az,el}}^2} \tag{4.29}$$

Now that we have computed the transverse wind speed, we can have a look at the transverse wind speed profiles.

4.5.2 Transverse wind speed profiles

Using the equation 4.29, we can compute the transverse wind speed profiles. Therefore, we will see how the transverse wind speed can vary in the turbulent zone. As it was done for the C_n^2 profiles, we have the transverse wind speed along the earth-satellite liaison 0, 0.5, 1, 1.5, 2, 2.5 and 3 km away from the antenna.

In the figures 4.11, we can see the profiles of the first of July.

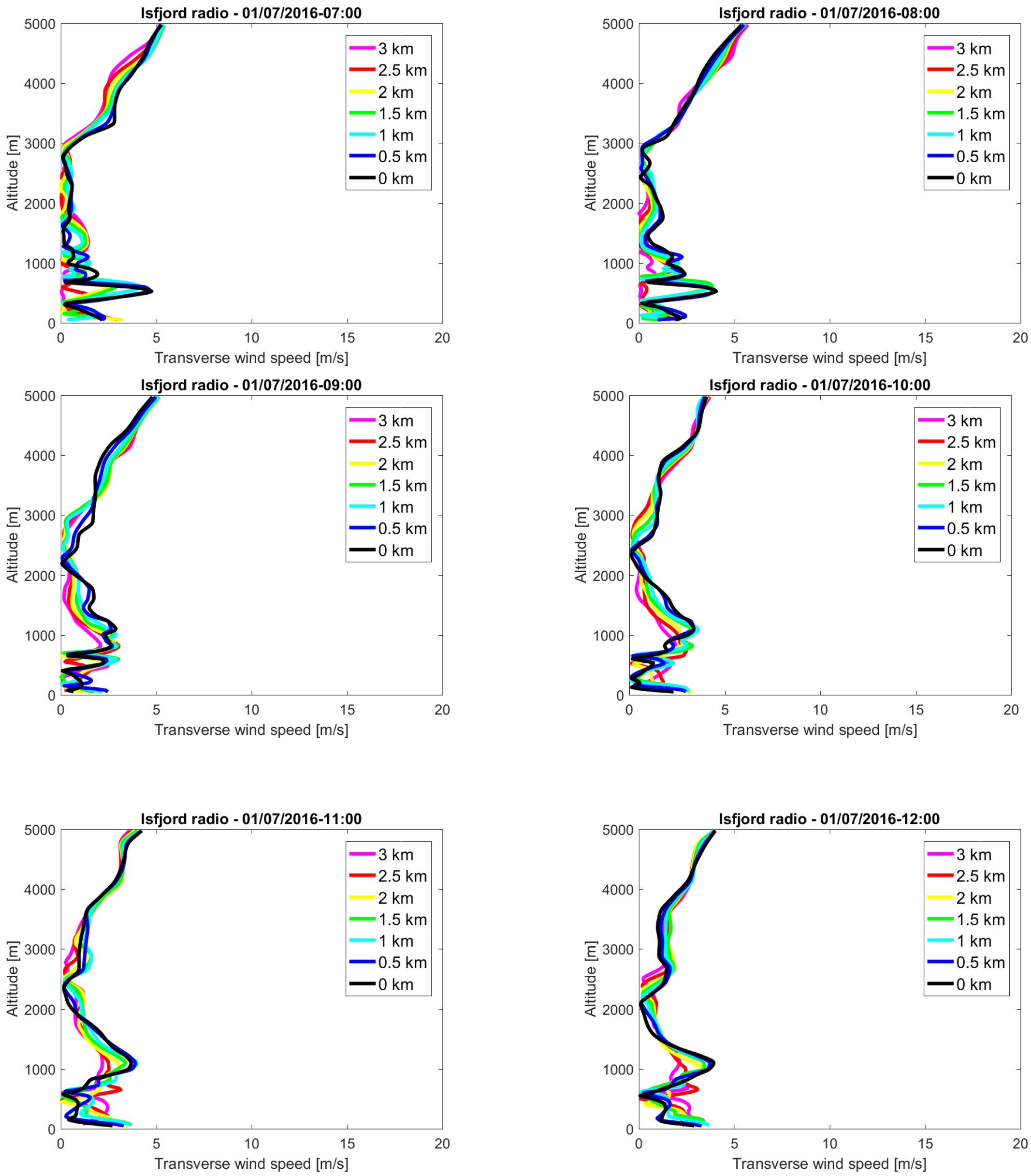

Figure 4.11 – Transverse wind speed profiles on the 1^{st} of July

From the figure 4.11, we see that the transverse wind speed was quite low that day. We also see that the wind speed does not vary a lot hour after hour. Finally, we can see that wind speed tends to increase when the altitude becomes very high.

In order to have a more general view, we will have a look at more profiles during the month of July.

In the figure 4.2, we can see the transverse wind speed profiles on the following days : 1, 3, 5, 7, 9, 11, 12, 14, 16, 18, 19, 21, 22, 24, 26, 28, 29 and 30^{th} of July 2016.

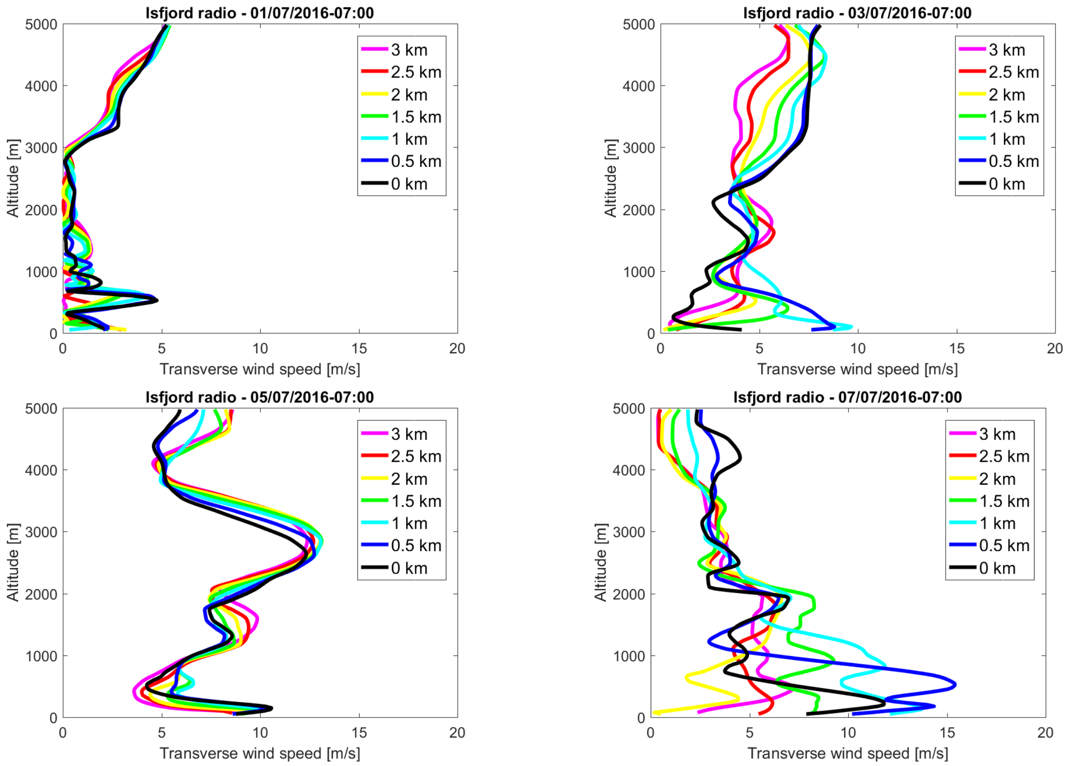

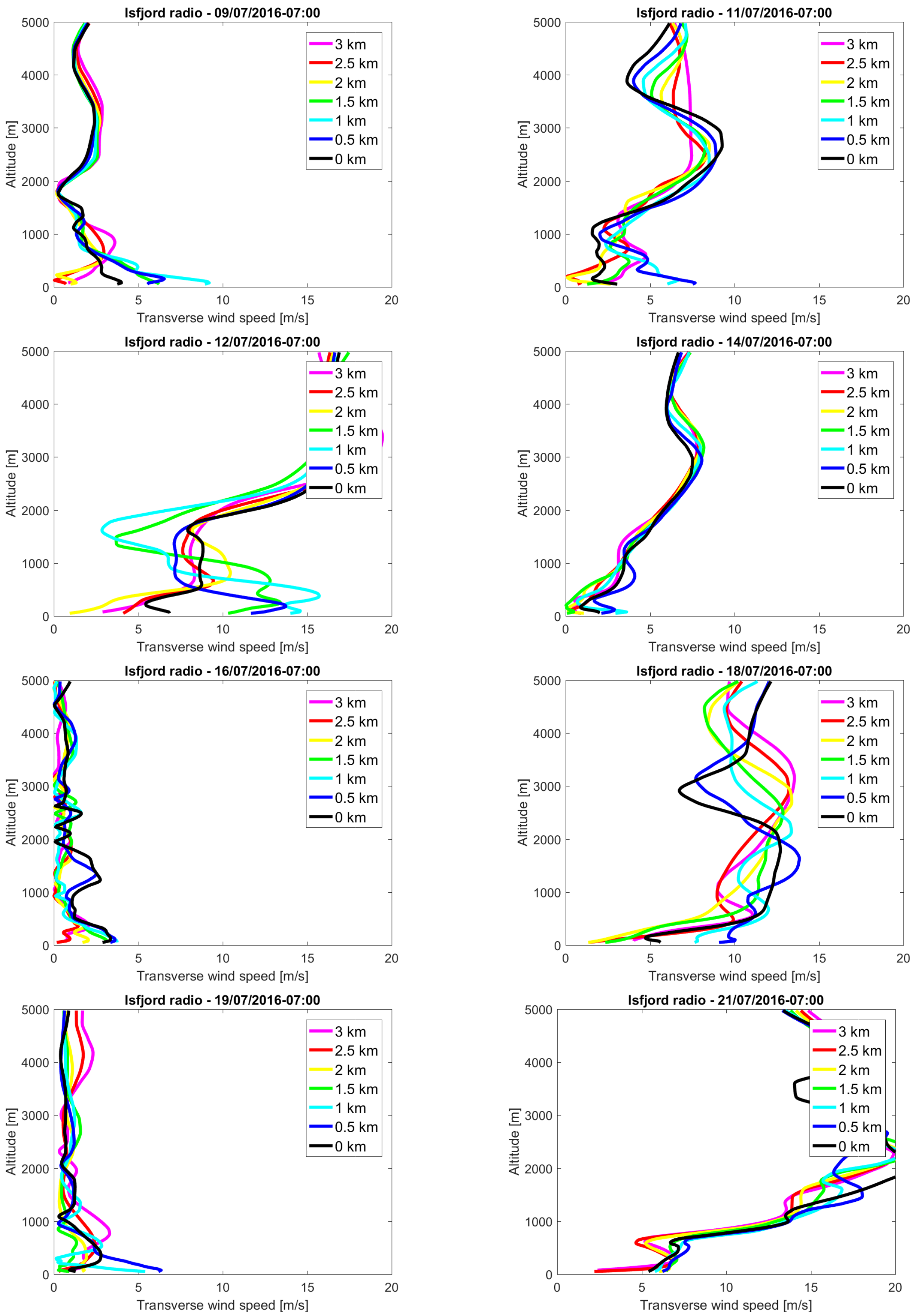
Isfjord radio - 09/07/2016-07:00
Isfjord radio - 11/07/2016-07:00
Isfjord radio - 12/07/2016-07:00
Isfjord radio - 14/07/2016-07:00
Isfjord radio - 16/07/2016-07:00
Isfjord radio - 18/07/2016-07:00
Isfjord radio - 19/07/2016-07:00
Isfjord radio - 21/07/2016-07:00
3 km
2.5 km
2 km
1.5 km
1 km
0.5 km
0 km
Altitude [m]
Transverse wind speed [m/s]
0
1000
2000
3000
4000
5000
0
5
10
15
20

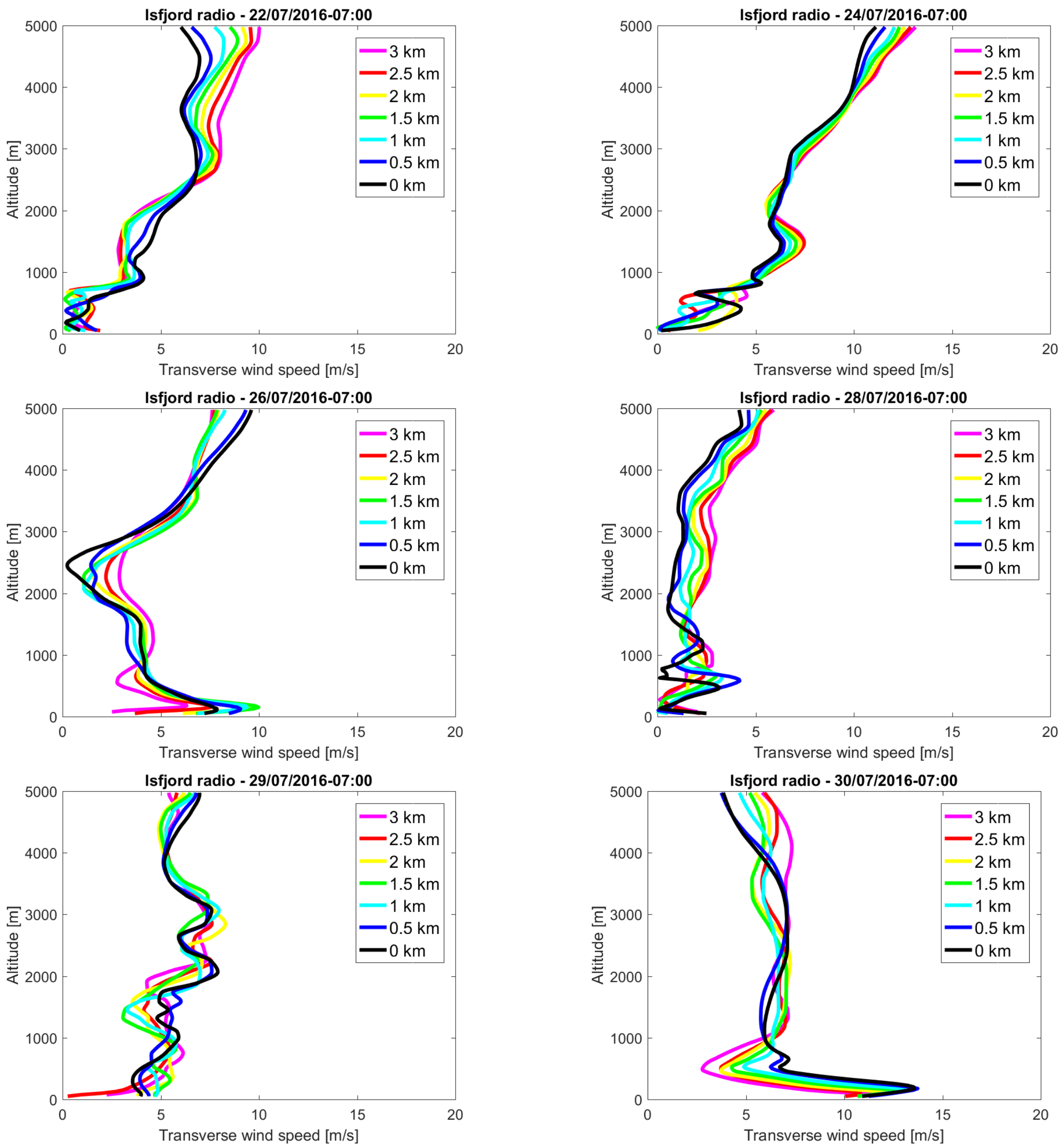

Figure 4.12 – Transverse wind speed profiles in most days of July at 7 a.m

From these profiles in the figures 4.12, we can make some conclusions. First, the transverse is in general between 0 and 20 m/s. Indeed, except on the 21^{th} of July, the transverse wind speed never goes above 20 m/s. We can also see that the profiles do not change much over the different points of the liaison (0-3km) and that the distance from the antenna does not have such a great influence on the wind profile.

Now that we have investigated the different parameters needed for the computation of the temporal frequency spectrum of the log-amplitude fluctuation, we will compute it and compare it with the measurements.

Chapter 5

Comparison of the different spectrum models with the measurements

In this chapter, we are going to compare the different models that we have with the measurements. We will then try to determine which one is the best and the most in accordance with the measurements.

As written in the previous chapters, there are 2 cases which have to be considered. The case where the link's length is large enough giving $\sqrt{\lambda L} >> L_0$ or the case where the link's length is relatively small giving $\sqrt{\lambda L} << L_0$.

With the hypotheses we made before, we computed that the link's length was about 38 215 m and that $\sqrt{\lambda L}$, the radius of the first Fresnel zone, was 24.5722 m. Therefore, in function of the outer scale length L_0, we will be in one of the two cases.

However, in practice, the outer scale length L_0 can not be computed with certainty. Some models have been made in literature to compute L_0 but the value can differ according to the model we choose [2]. Although, we can say with a fair certainty that L_0 is always between 10 m and 100 m (sometimes even lower [2]). Therefore, in this work, we will test our models with different values for L_0 and see what happens.

5.1 Analyse of the first spectrum model when $\sqrt{\lambda L} << L_0$

For a start, we will suppose that L_0 is higher than $\sqrt{\lambda L}$ and we will investigate the effect of the structure constant C_n^2 on the spectrum. As we have seen it in the previous chapters, the refractive structure constant can be either supposed to be constant or vary along the link. Therefore, we have choose between one of the following options :

- C_n^2 is supposed to be constant. In that case, the question of choosing a value for the C_n^2 arises.
- C_n^2 is considered to vary with the position

According to the choice we make, the temporal frequency spectrum will have different equations :

$$W_\chi(\omega) = 8\pi^2 k^2 L \int_{\omega/U_t}^{\infty} f(\kappa)\Phi_n(\kappa)[(\kappa U_t)^2 - \omega^2]^{-1/2}\kappa d\kappa \tag{5.1}$$

The temporal frequency spectrum model of the log-amplitude fluctuation (χ) with constant C_n^2 (see equation 5.1).

$$W_\chi(\omega) = 16\pi k^2 \int_0^L C_n^2(r)d\eta \int_{\omega/U_t}^{\infty} \Phi_n^{(0)}(\kappa)[(\kappa U_t)^2 - \omega^2]^{-1/2}\kappa d\kappa \tag{5.2}$$

The temporal frequency spectrum model of χ with varying C_n^2 (see equation 5.2).

At this stage, it is not yet possible to compute these two spectra for several reasons which we are going to explain in the next section.

5.1.1 Choice of the parameters and discretization of the C_n^2 varying spectrum

In order to compute the spectrum, we still have to make several things. First, in the case of the constant C_n^2 hypothesis, we still have to choose a value for C_n^2. Second, at this stage, the transverse wind speed U_t is supposed to be constant over the whole link, so we also have to choose its value. Finally, in the case of a varying C_n^2, C_n^2 is integrated over the link's length in the turbulent zone. However, the C_n^2 is not available in a continuous range. The integral must thus be transformed into a sum.

Choice of the transverse wind velocity

At this stage, the transverse wind speed is considered to be constant. To choose its value, we will look at its variation along the link in the turbulent zone and take its mean. As said in the chapter 3, we have at our disposal the measurements during the months of March and July 2016. Therefore, it is during these periods that we are going to look at our models in order to be able to do a comparison between the spectrum models and the measurements.

As an example, we will have a look at the transverse wind speed on the first of July.

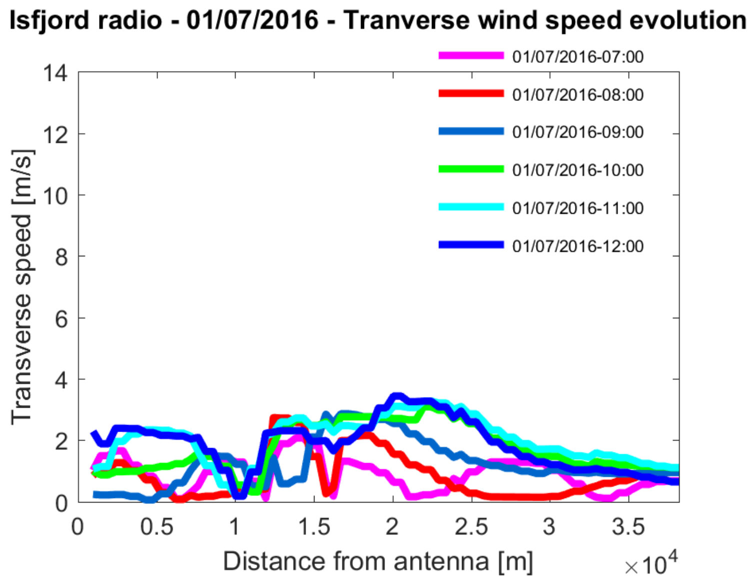

Figure 5.1 – Transverse wind speed along the link in the turbulent zone

In the figure 5.1, we can see the transverse wind speed versus the distance from the antenna (considering the 3°angle of azimuth and the 3°angle of elevation) on the 1^{st} of July between 7 a.m and 12 a.m.

As we can see it, the transverse speed was quite low in the morning of the 1^{st} of July and was always below 4 m/s. The mean values at each hour have been computed and can be seen in the table 5.1.

1^{st} of July	7 a.m	8 a.m	9 a.m	10 a.m	11 a.m	12 a.m
$U_t[m/s]$	0.8951	0.8463	1.2385	1.7529	2.0131	1.8694

Table 5.1 – Mean values of and the transverse wind speed

Choice of the refractive structure constant C_n^2

As we did for the transverse wind speed, we will compute the mean of the C_n^2 along the link in the turbulent zone in order to have the constant C_n^2 we need for the temporal frequency spectrum with constant C_n^2. In the figure 5.2, We can see the evolution of the C_n^2 depending on the distance from the antenna.

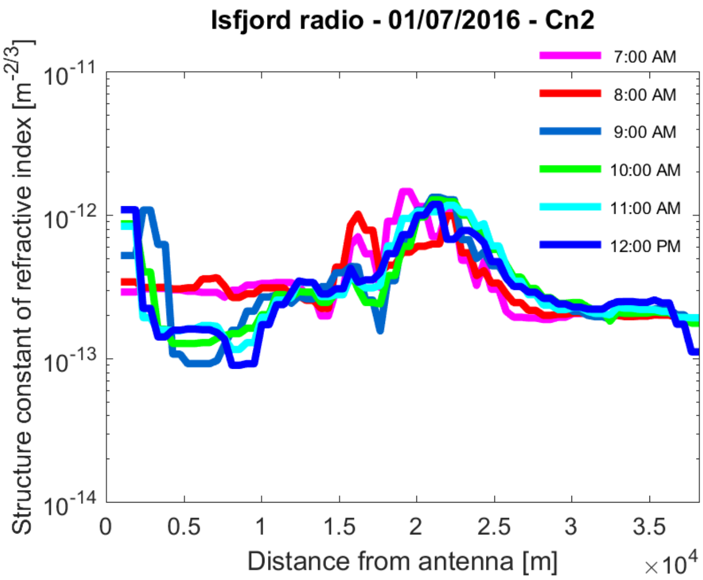

Figure 5.2 – C_n^2 along the liaison

As we can see, the value of the C_n^2 is roughly between 10^{-12} and 10^{-13}. Its mean value can be seen in the table 5.2.

1^{st} of July	7 a.m	8 a.m	9 a.m	10 a.m	11 a.m	12 a.m
$C_n^2 \times 10^{12}[m^{-2/3}]$	0.3821	0.3538	0.3863	0.3814	0.3917	0.3712

Table 5.2 – Mean values of the C_n^2

Now that we have chosen the values for C_n^2 and U_t, we still have one thing to do concerning the temporal frequency spectrum with varying C_n^2. Indeed, we only have the C_n^2 only at certain points of the link, so we have to transform the integral into a sum.

Discretization of the temporal frequency spectrum with varying C_n^2

Starting from the following continuous equation :

$$W_\chi(\omega) = 16\pi k^2 \int_0^L C_n^2(r)d\eta \int_{\omega/U_t}^{\infty} sin^2[\frac{\kappa^2(L-\eta)}{2k}]\Phi_n^{(0)}(\kappa)[(\kappa U_t)^2 - \omega^2]^{-1/2}\kappa d\kappa \quad (5.3)$$

We obtain the discrete equation for the time-frequency spectrum with varying C_n^2.

$$W_\chi(\omega) = 16\pi k^2 \sum_0^L C_n^2(\eta)\Delta\eta \int_{\omega/U_t}^{\infty} sin^2[\frac{\kappa^2(L-\eta)}{2k}]\Phi_n^{(0)}(\kappa)[(\kappa U_t)^2 - \omega^2]^{-1/2}\kappa d\kappa \quad (5.4)$$

Which is equivalent to :

$$W_\chi(\omega) = 16\pi k^2 \int_{\omega/U_t}^{\infty} \left(\sum_0^L C_n^2(\eta)\Delta\eta\right) sin^2[\frac{\kappa^2(L-\eta)}{2k}]\Phi_n^{(0)}(\kappa)[(\kappa U_t)^2 - \omega^2]^{-1/2}\kappa d\kappa \quad (5.5)$$

For the purposes of the simulation, it is better to use this last expression since it allows us to make the integral only once.

With the equations 5.1 and 5.5 and the values of all parameters such as U_t and C_n^2, we can finally compute the temporal frequency spectra of our model with constant or varying C_n^2.

5.1.2 Comparison between the two submodels of the first spectrum model: constant C_n^2 and C_n^2 varying along the link

In the analysis of this first model, we will first have a look at the influence of the C_n^2 and compare our two cases corresponding to the equations 5.1 and 5.5.

On the figure 5.3, we can see the temporal frequency spectra of the log-amplitude fluctuation in the two situations. On the left, we have our first submodel with constant C_n^2 and on the right the second submodel with varying C_n^2. The asymptotic behaviour for the constant C_n^2 spectrum can also be seen in the figures. Finally, the corner frequency is also visible in both submodels. It is important to remind here that the transition frequency is the same for both submodels and has the following expression :

$$\omega_t = 1.43 U_t \left(\frac{k}{L}\right)^{1/2} \tag{5.6}$$

The figures 5.3 shows the spectra on the 1^{st}, 2^{sd}, 3^{th},5^{th} and 10^{th} of July at 7 a.m.

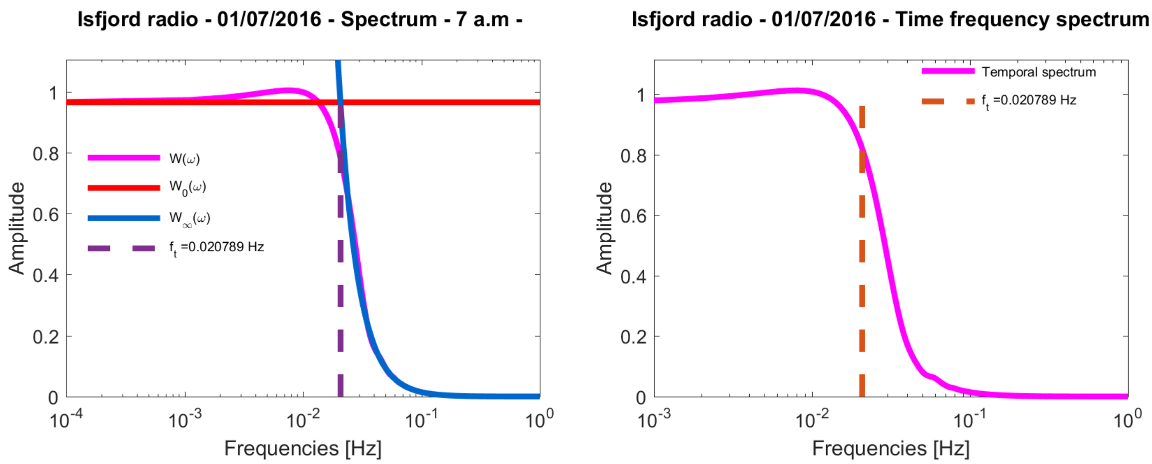

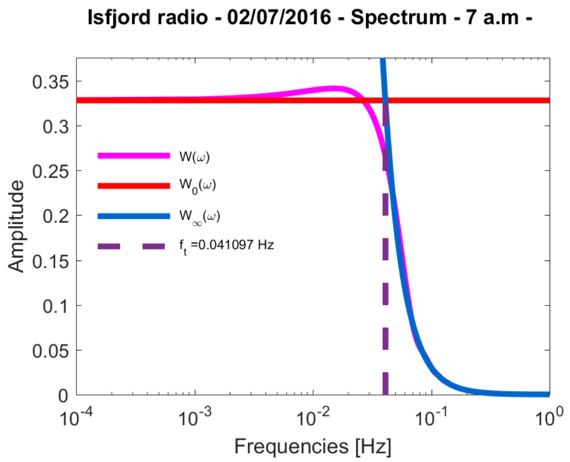
Isfjord radio - 02/07/2016 - Spectrum - 7 a.m -
W(ω)
W0(ω)
W∞(ω)
ft =0.041097 Hz
Amplitude
Frequencies [Hz]

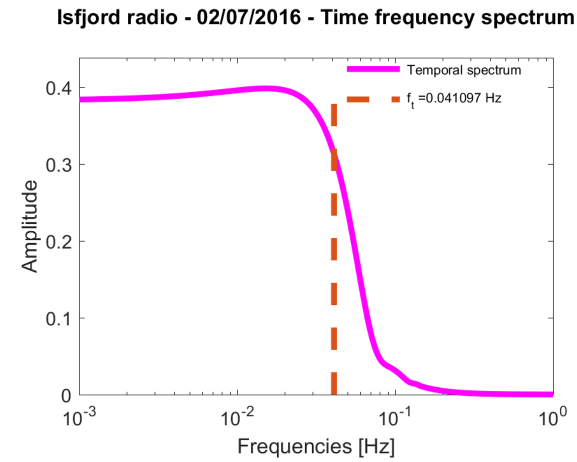
Isfjord radio - 02/07/2016 - Time frequency spectrum
Temporal spectrum
ft =0.041097 Hz
Amplitude
Frequencies [Hz]

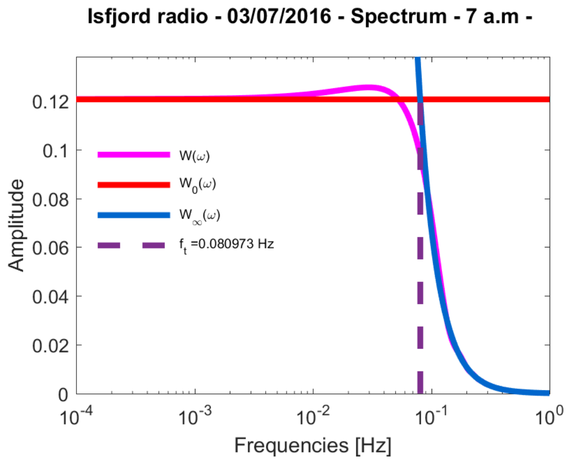
Isfjord radio - 03/07/2016 - Spectrum - 7 a.m -
W(ω)
W0(ω)
W∞(ω)
ft =0.080973 Hz
Amplitude
Frequencies [Hz]

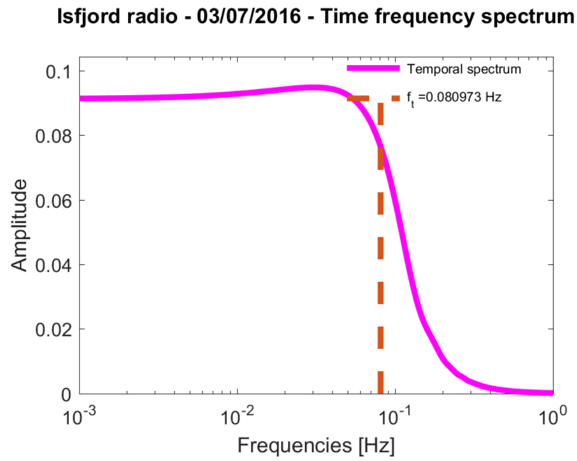
Isfjord radio - 03/07/2016 - Time frequency spectrum
Temporal spectrum
ft =0.080973 Hz
Amplitude
Frequencies [Hz]

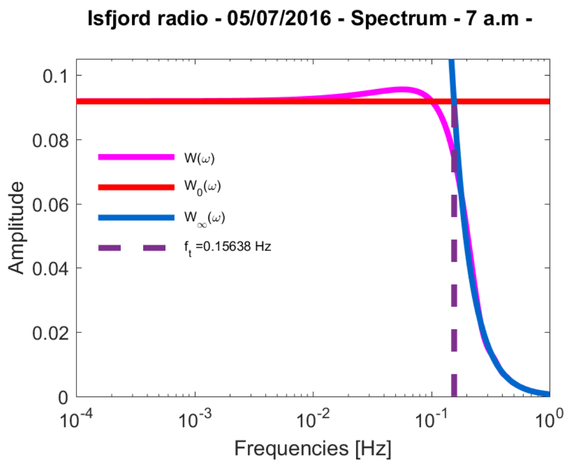
Isfjord radio - 05/07/2016 - Spectrum - 7 a.m -
W(ω)
W0(ω)
W∞(ω)
ft =0.15638 Hz
Amplitude
Frequencies [Hz]

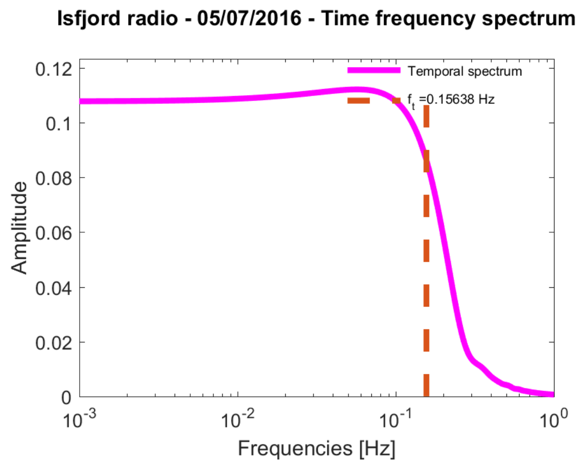
Isfjord radio - 05/07/2016 - Time frequency spectrum
Temporal spectrum
ft =0.15638 Hz
Amplitude
Frequencies [Hz]

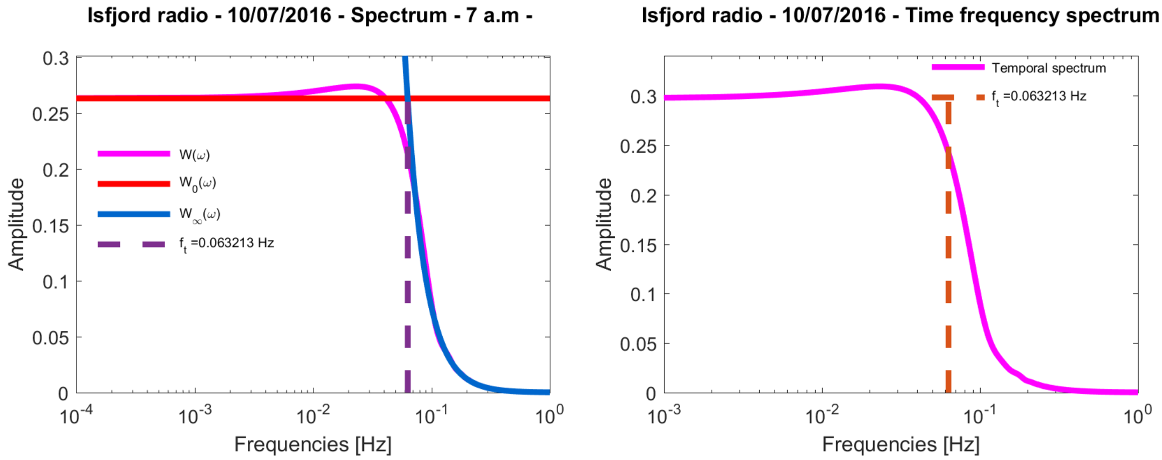

Figure 5.3 – Temporal spectrum with constant (left) and varying (right) C_n^2 on the $1^{st}, 2^{sd}, 3^{th}, 5^{th}$ and 10^{th} of July

All the values of the parameters which were used can be seen in the table 5.3.

Day of July at 7 a.m	1^{st}	2^{st}	3^{st}	5^{st}	10^{st}
U_t $[m/s]$	0.895	1.77	3.487	6.734	2.722
C_n^2 $[m^{-2/3}]$ (cst C_n^2 spectrum)	3.821E-13	2.567E-13	1.858E-13	2.732E-13	3.167E-13
f $[GHz]$	19				
λ $[m]$	0.0158				
k $[m^{-1}]$	397.935				
L $[m]$	38215				

Table 5.3 – U_t values

There are several things which can be said about these figures (see figure 5.3). To begin with, we can see that the two submodels are very similar. There are only two small differences : firstly the amplitude at low frequencies is slightly different and secondly the spectrum with varying C_n^2 is slightly bumpy towards higher frequency (this is quite negligible).

Also, we can see that the transition frequency can vary quite a lot with the transverse wind speed. Using all the spectra of the month of July (only 5 showed here), it can be shown that the transition frequency of our model is always comprised between 0.01 Hz from to 0.3 Hz. This is quite a large range and it shows the big influence of the transverse speed on our models. For example, in the figure 5.3, we see that on the 1^{st} of July, we have $f_t = 0.0207\ Hz$ compared to $f_t = 0.1564\ Hz$ on the 5^{th}. If we look at their corresponding U_t in the table 5.3, we see that the difference between the two transverse wind speed is quite large.

Now that we have made a first analysis of the two submodels of our first model, it could be very interesting to compare them with the measurements.

5.1.3 Comparison of the 2 models of the first model with the measurements

Before being able to make a comparison, we must be sure that our models and our measurements represent the same thing, which is not the case here. Indeed, we do not have the temporal frequency spectrum of the log-amplitude fluctuation for the measurements but we do have the power spectrum density. Therefore, we need to make the correct transformation to our model in order to be able to make a comparison.

The Power spectrum density

Therefore, we need to transform the temporal frequency spectrum of our model into a power spectrum density. Using the relation 5.7, our model will have the same order of magnitude as the measurements and will be in dB^2/Hz.

$$PSD(\omega) \propto 10\log_{10}|W(\omega)|/1Hz \tag{5.7}$$

Where $W(\omega)$ is the temporal frequency spectrum.

Comparison with the measurements

Now that we have made the transformation from the equation 5.7, it is possible to make a comparison.

In the following figures (see figures 5.4), we can see side by side the two submodels of our first model and the measurements on the 1^{st}, 3^{th}, 5^{th}, 9^{th}, 11^{th}, 13^{th}, 15^{th} and 17^{th} of July at 7 a.m.

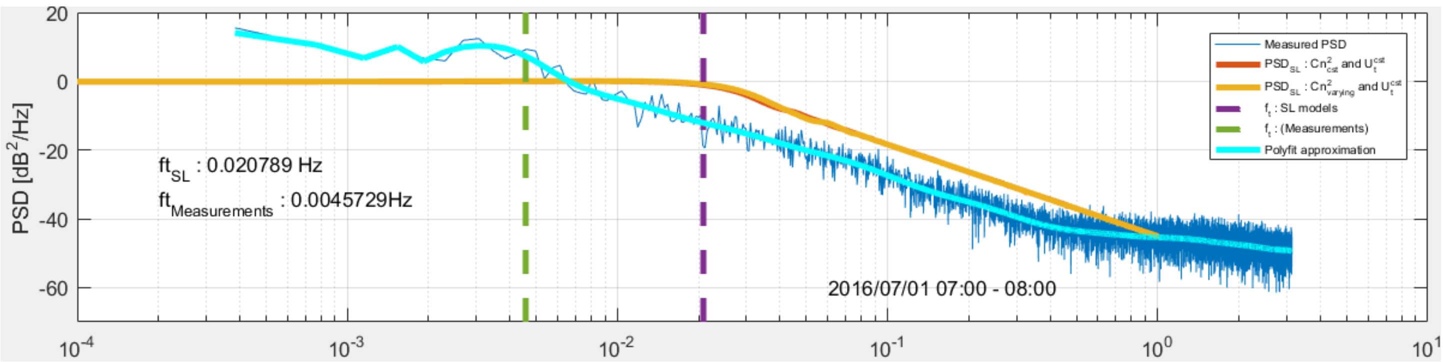

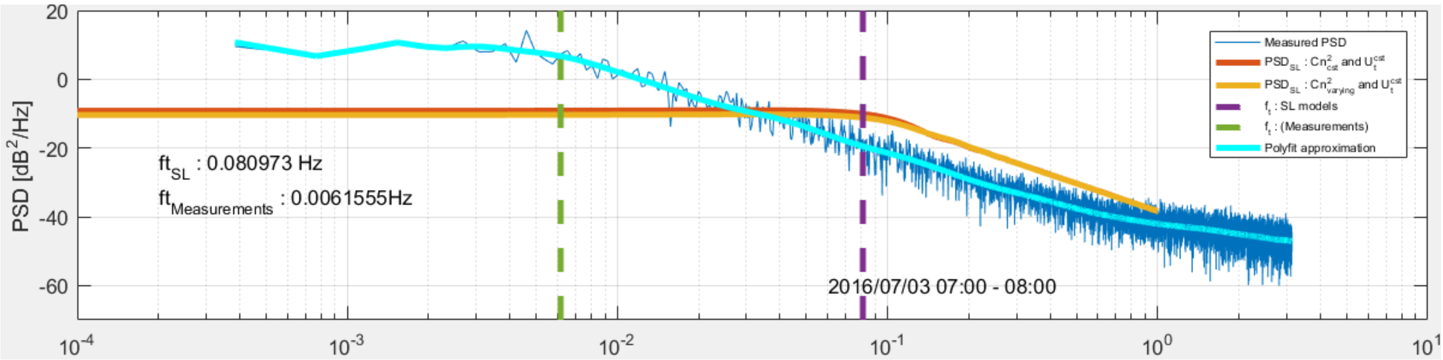

PSD [dB²/Hz]
ft_SL : 0.080973 Hz
ft_Measurements : 0.0061555Hz
2016/07/03 07:00 - 08:00
Measured PSD
PSD_SL : Cn²_cst and U_t^cst
PSD_SL : Cn²_varying and U_t^cst
f_t : SL models
f_t : (Measurements)
Polyfit approximation

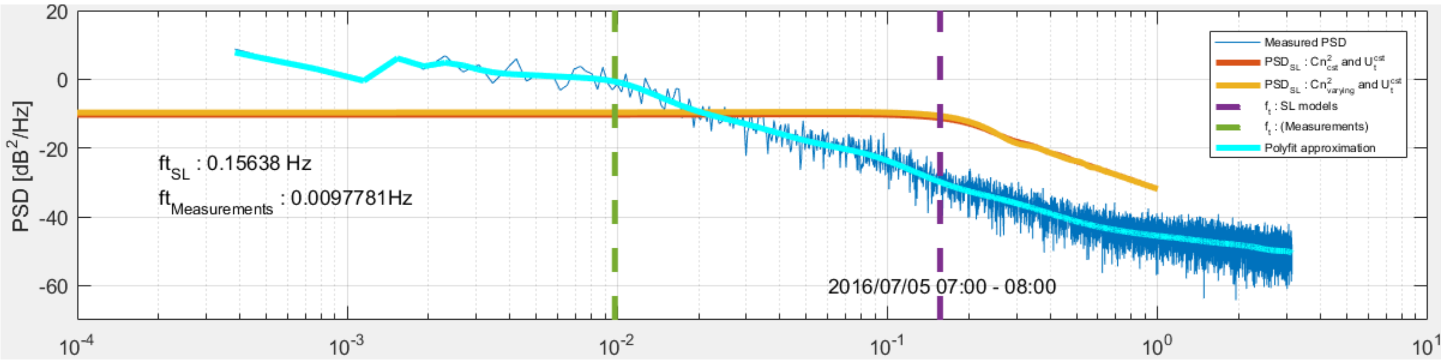

PSD [dB²/Hz]
ft_SL : 0.15638 Hz
ft_Measurements : 0.0097781Hz
2016/07/05 07:00 - 08:00
Measured PSD
PSD_SL : Cn²_cst and U_t^cst
PSD_SL : Cn²_varying and U_t^cst
f_t : SL models
f_t : (Measurements)
Polyfit approximation

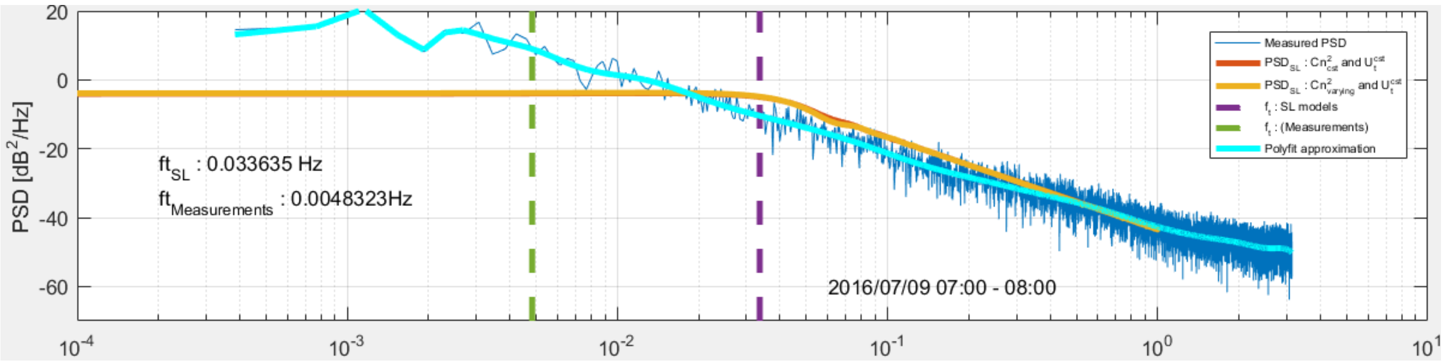

PSD [dB²/Hz]
ft_SL : 0.033635 Hz
ft_Measurements : 0.0048323Hz
2016/07/09 07:00 - 08:00
Measured PSD
PSD_SL : Cn²_cst and U_t^cst
PSD_SL : Cn²_varying and U_t^cst
f_t : SL models
f_t : (Measurements)
Polyfit approximation

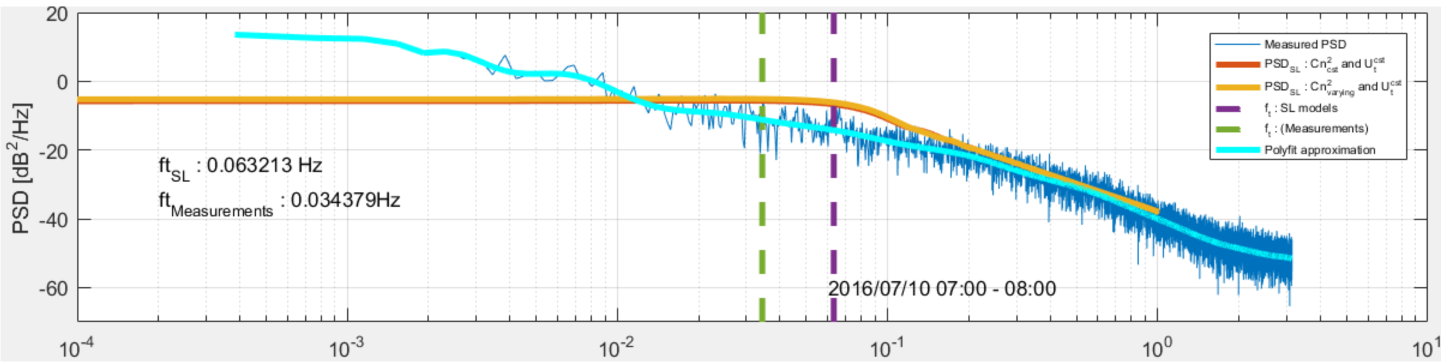

PSD [dB²/Hz]
ft_SL : 0.063213 Hz
ft_Measurements : 0.034379Hz
2016/07/10 07:00 - 08:00
Measured PSD
PSD_SL : Cn²_cst and U_t^cst
PSD_SL : Cn²_varying and U_t^cst
f_t : SL models
f_t : (Measurements)
Polyfit approximation

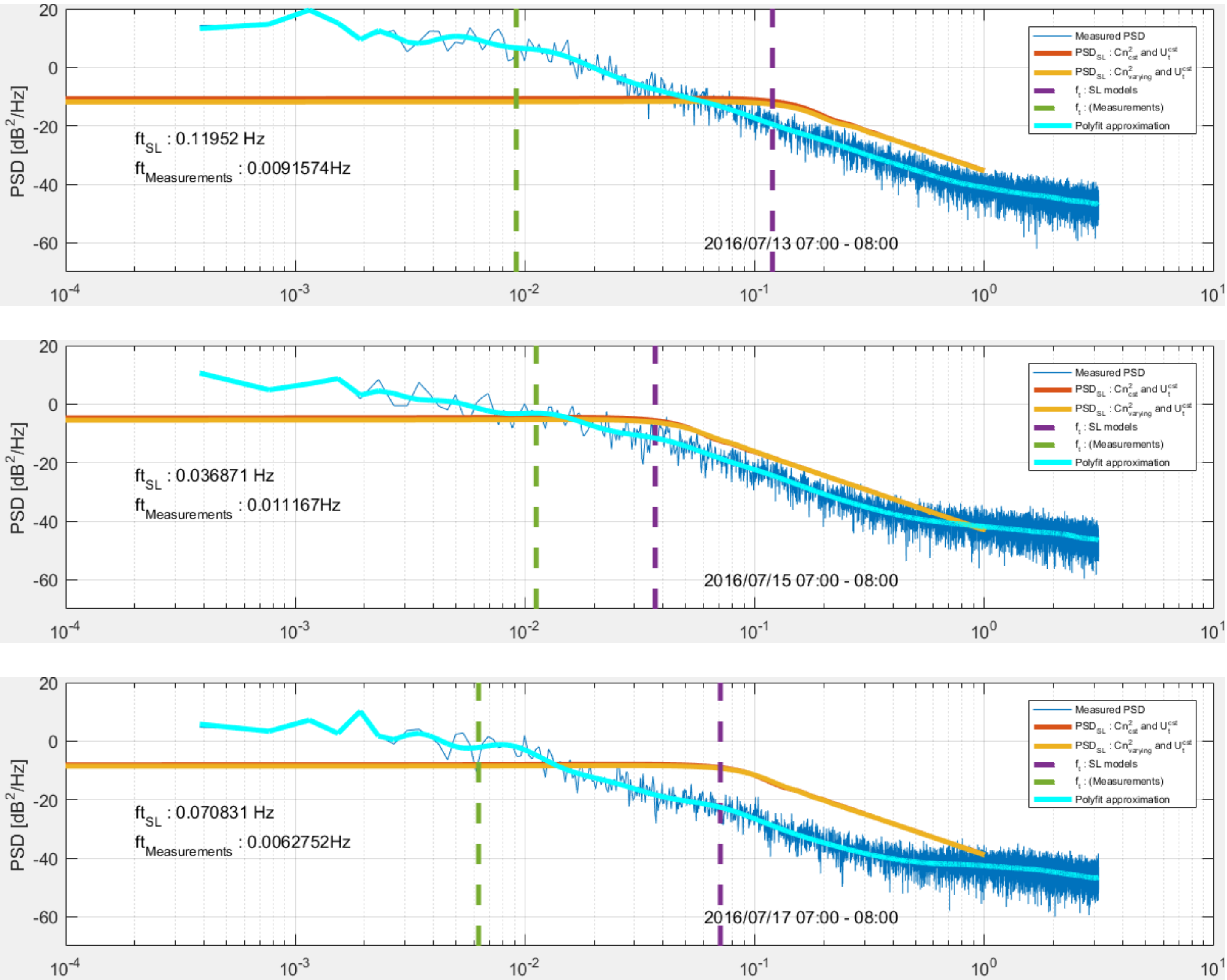

Figure 5.4 – Scintillation measurements versus our two submodels with constant and varying C_n^2 on the 1^{st}, 3^{th}, 5^{th}, 9^{th}, 11^{th}, 13^{th}, 15^{th} and 17^{th}

From the figures 5.4, we can see that our two models are quite close to the measurement PSD but they are not perfect. The main problem is about the transverse speed. Indeed, the measured transition frequency is always around 10^{-2} Hz or lower while the modelled transition frequency is in general around 10^{-1} Hz. There is almost always one order of magnitude of difference between the modelled and measured transition frequencies.

For example, for the 3^{th} of July, the measured transition frequency is 0.00615 Hz and the modelled transition frequency is 0.0809 Hz. For the 9^{th} of July, the measured transition frequency is 0.0048 Hz and the modelled transition frequency is 0.033 Hz. If we take other days, it is the same : we always have a 10 factor between the modelled and the measured transition frequency. However, if we look at the figures corresponding to the 10^{th} and the 15^{th} of July, we see that the transition frequencies of both our models and the measurement PSD are quite close. Unfortunately, if we look at all the data set of the month, this phenomenon is really unusual and it is not possible to make a conclusion for all these cases.

Regarding the slope at high frequencies, both our submodels are really precise. We see that in every case, the slope of the polyfit approximation is almost exactly parallel to the ones of the models. If we look for example at the graphs of the 9^{th} and on 13^{th}, we can well see the approximation of the measurements and the models have the same slope at high frequencies.

Finally, the amplitude of our models is always a little bit too small for low frequencies on the left of the transition frequency. For example, on the 9^{th} of July, we have about 20 dB of difference, which is quite large. If we look at the whole data set of the month of July, these submodels always have a too small amplitude at low frequencies.

Concerning our two submodels, we see that they are always overlapped and that they are almost equivalent. Consequently, from now on, we will only consider that the C_n^2 varies along the liaison.

Until now, we have considered that the transverse wind speed was constant along the liaison. For our next model, we will see what happens when we consider that, as C_n^2, it varies along the liaison.

5.1.4 The temporal frequency spectrum with varying transverse wind speed

For our next model, we will no longer consider the transverse wind speed as a constant as it was done for the C_n^2 in the previous section. We will then see whether considering a varying U_t can be an improvement for our first method or not.

When we consider the varying transverse wind speed, the equation of the temporal frequency spectrum of χ becomes :

$$W_\chi(\omega) = 16\pi k^2 \sum_0^L C_n^2(\eta) d\eta \int_{\omega/U_t(\eta)}^{\infty} sin^2[\frac{\kappa^2(L-\eta)}{2k}]\Phi_n^{(0)}(\kappa)[(\kappa U_t(\eta))^2 - \omega^2]^{-1/2}\kappa d\kappa \tag{5.8}$$

In the figures 5.5, we can see the temporal frequency spectrum of χ when U_t is not constant. Since U_t is no longer a constant,we no longer have any analytical expression for the transition frequency as we did before. The graphs of figure 5.5 show us the spectra on the 1^{st},2^{sd},3^{th},4^{th},7^{th},10^{th},15^{th},20^{th},23^{th},24^{th},29^{th} and the 30^{th} of July at 7 a.m.

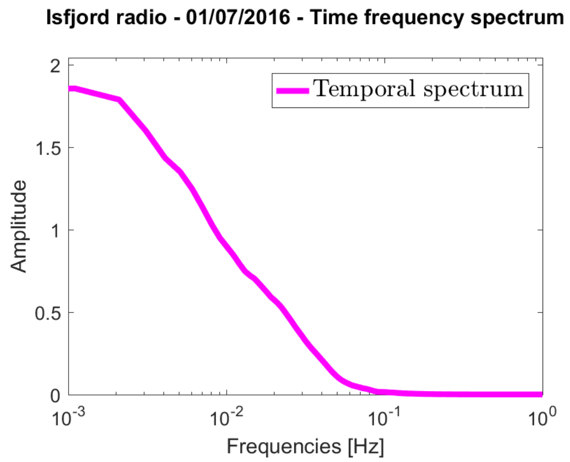
Isfjord radio - 01/07/2016 - Time frequency spectrum
Temporal spectrum
Amplitude
Frequencies [Hz]

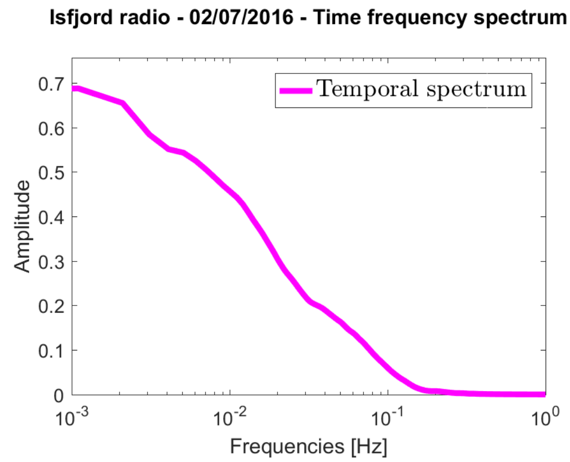
Isfjord radio - 02/07/2016 - Time frequency spectrum
Temporal spectrum
Amplitude
Frequencies [Hz]

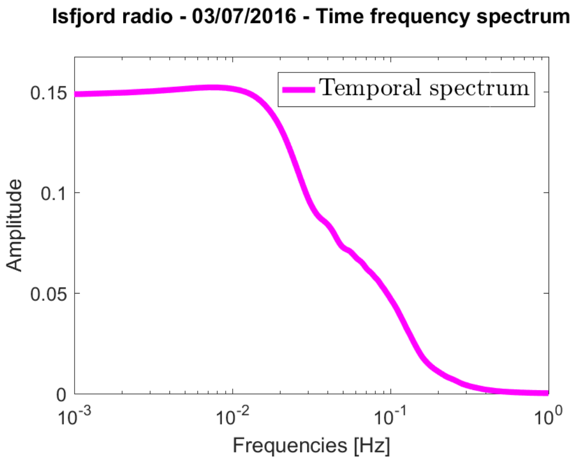
Isfjord radio - 03/07/2016 - Time frequency spectrum
Temporal spectrum
Amplitude
Frequencies [Hz]

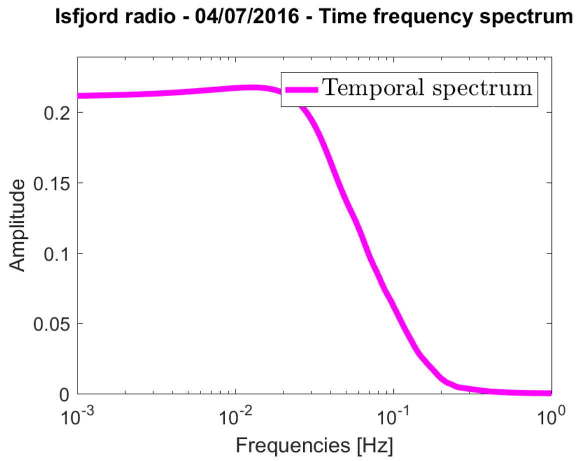
Isfjord radio - 04/07/2016 - Time frequency spectrum
Temporal spectrum
Amplitude
Frequencies [Hz]

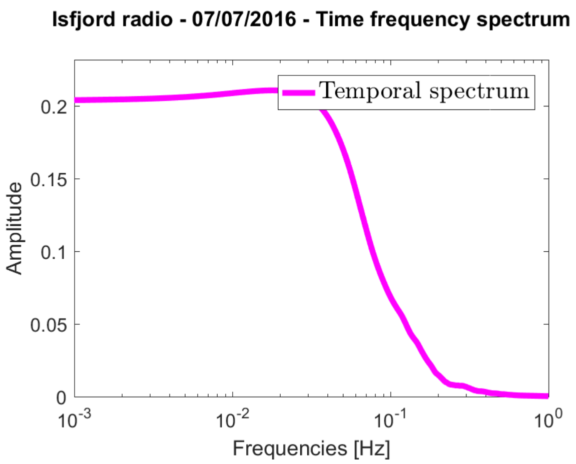
Isfjord radio - 07/07/2016 - Time frequency spectrum
Temporal spectrum
Amplitude
Frequencies [Hz]

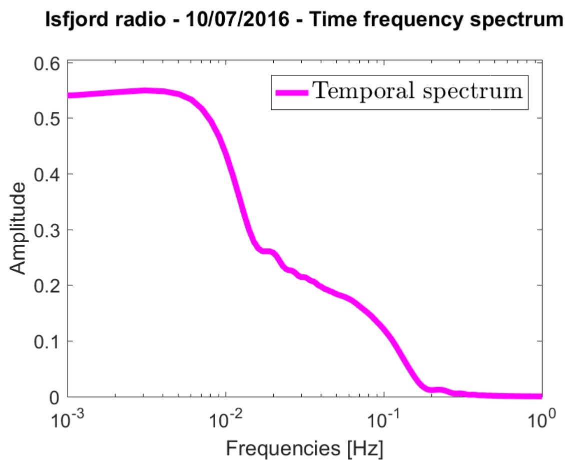
Isfjord radio - 10/07/2016 - Time frequency spectrum
Temporal spectrum
Amplitude
Frequencies [Hz]

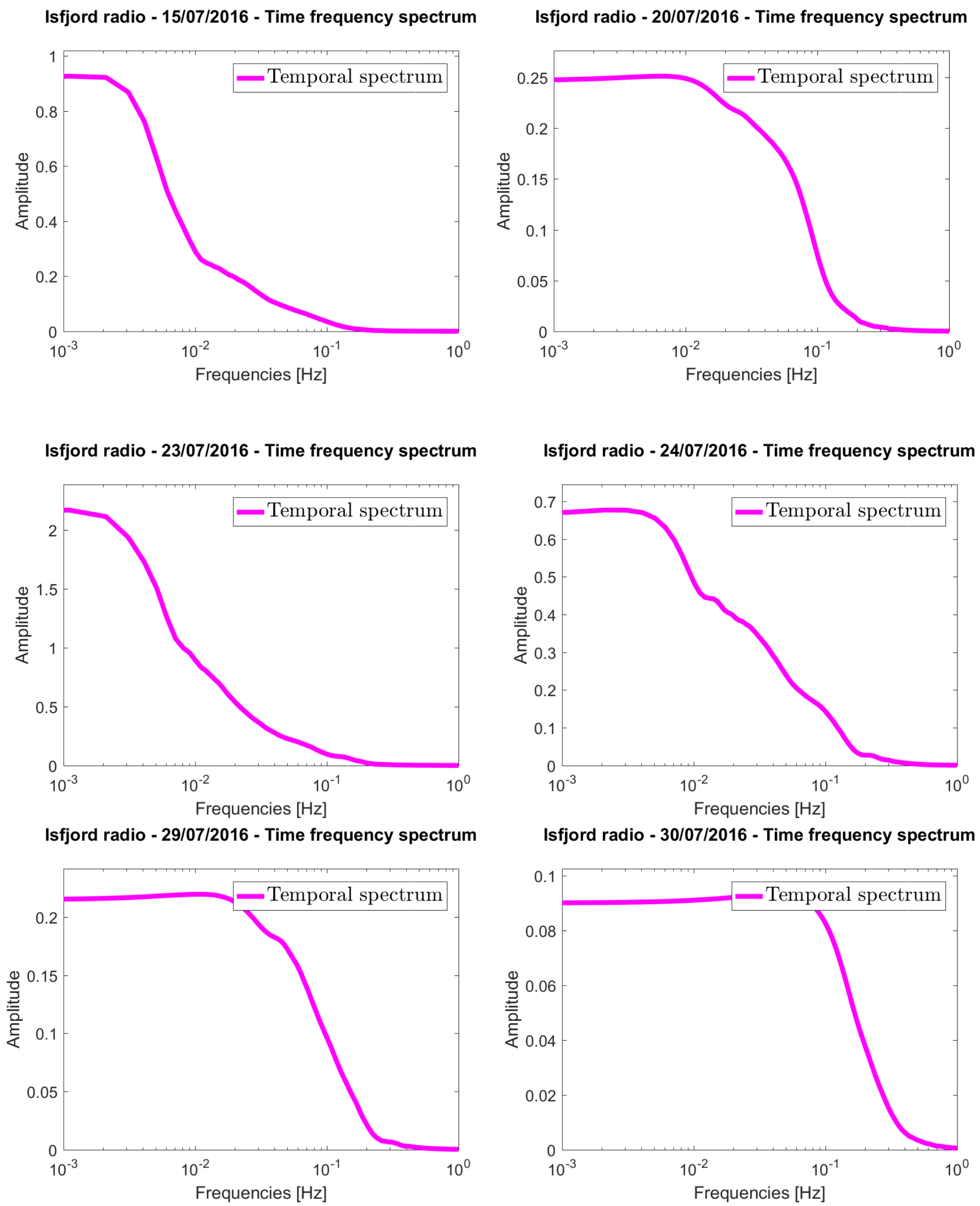

Figure 5.5 – Temporal frequency spectrum with varying U_t on the 1^{st},2^{sd},3^{th},4^{th},7^{th},10^{th},15^{th},20^{th},23^{th},24^{th},29^{th} and the 30^{th} of July at 7 a.m

At figure 5.5, we see that these spectra are quite different from those where U_t was constant. The first thing that we can say is that according to the day, the shape of the spectrum can be very different. For example, if we compare the spectrum on the 1^{st}, the 10^{th} and the 20^{th}, we see that the shapes are completely different. We no longer have a regular slope as we did before and the transition frequency is more difficult to place. For example, if we look on the 1^{st} and 2^{sd} of July, it is more difficult to separate the spectrum at low frequencies and at high frequencies.

Also, the differences of amplitude from day to day are much more significant than before. Therefore, the varying character of the transverse wind speed has much more influence than C_n^2. This is due to the fact that, according to the value of U_t, the contribution to the integral will be smaller or higher (see equation 5.11).

In order to explain the sometimes strange shape of the spectra at figure 5.5, we will have a look at the evolution of the transverse wind speed along the link at the moments in question. Therefore, in the figures 5.6, we can see the evolution of transverse wind speed along the path on 1^{st},2^{sd},3^{th},4^{th},7^{th},10^{th},15^{th},20^{th},23^{th},24^{th},29^{th} and the 30^{th} of July at 7 a.m.

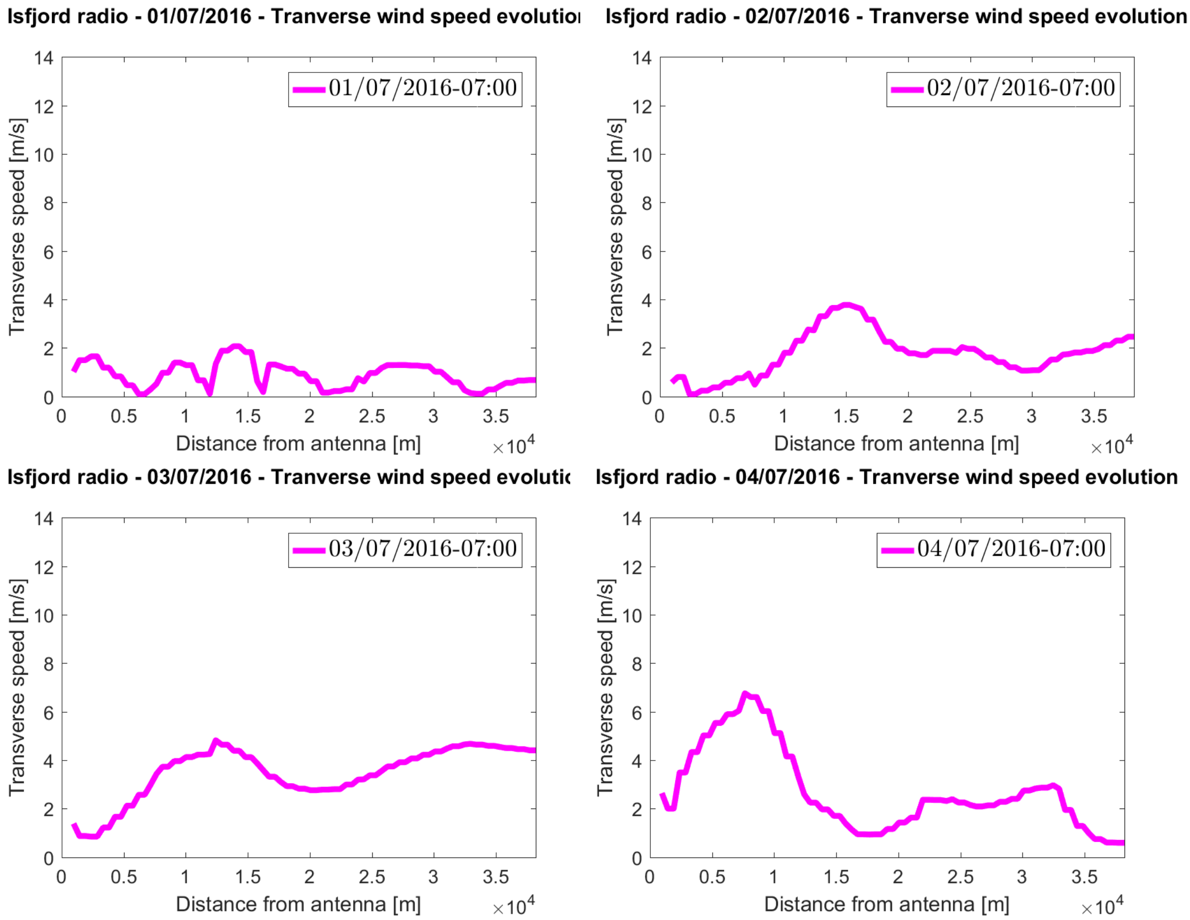

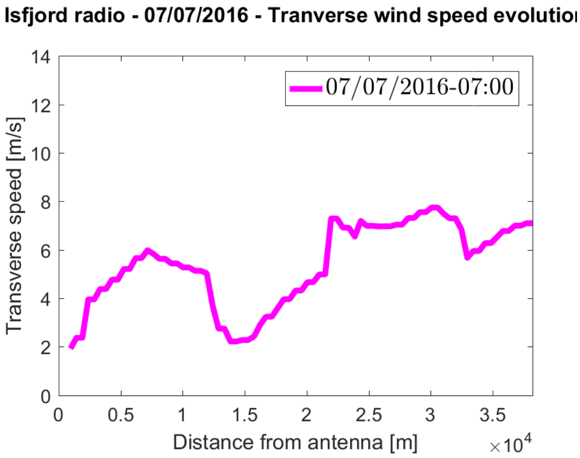
Isfjord radio - 07/07/2016 - Tranverse wind speed evolutio
07/07/2016-07:00
Transverse speed [m/s]
Distance from antenna [m]
×10^4

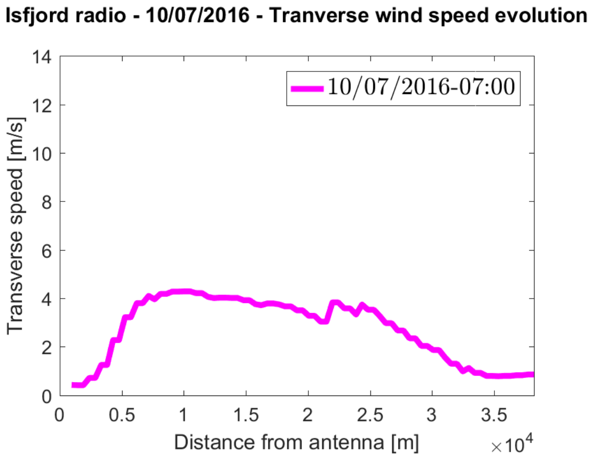
Isfjord radio - 10/07/2016 - Tranverse wind speed evolution
10/07/2016-07:00
Transverse speed [m/s]
Distance from antenna [m]
×10^4

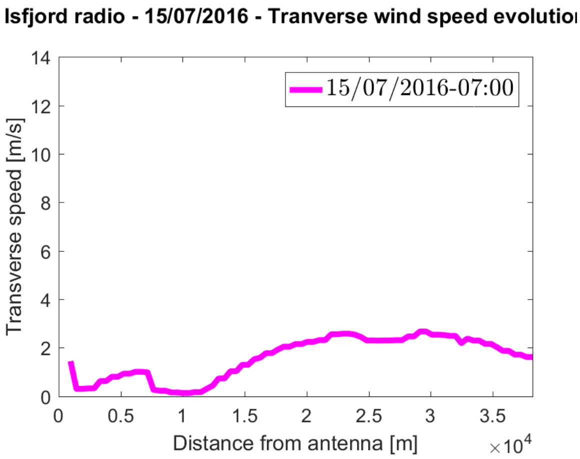
Isfjord radio - 15/07/2016 - Tranverse wind speed evolutio
15/07/2016-07:00
Transverse speed [m/s]
Distance from antenna [m]
×10^4

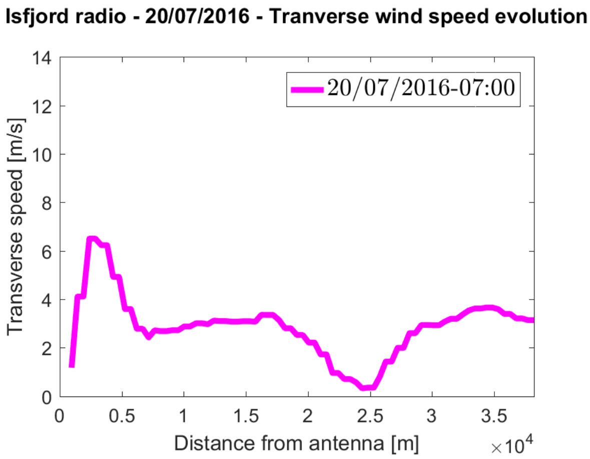
Isfjord radio - 20/07/2016 - Tranverse wind speed evolution
20/07/2016-07:00
Transverse speed [m/s]
Distance from antenna [m]
×10^4

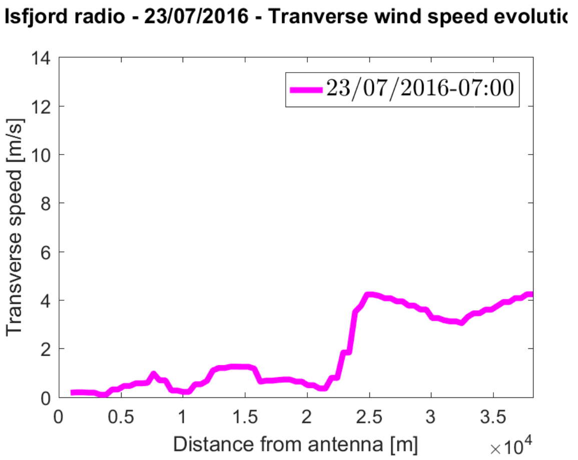
Isfjord radio - 23/07/2016 - Tranverse wind speed evolutic
23/07/2016-07:00
Transverse speed [m/s]
Distance from antenna [m]
×10^4

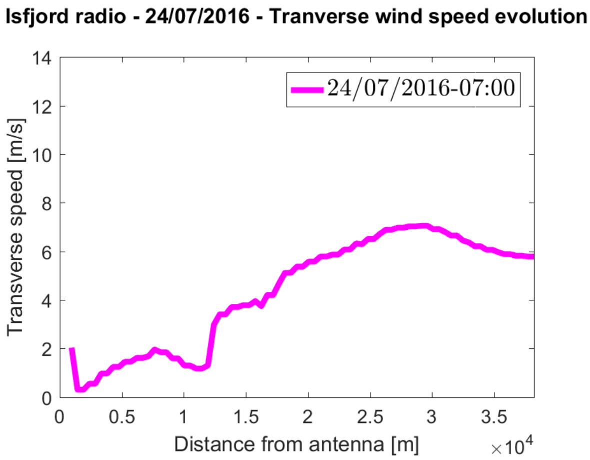
Isfjord radio - 24/07/2016 - Tranverse wind speed evolution
24/07/2016-07:00
Transverse speed [m/s]
Distance from antenna [m]
×10^4

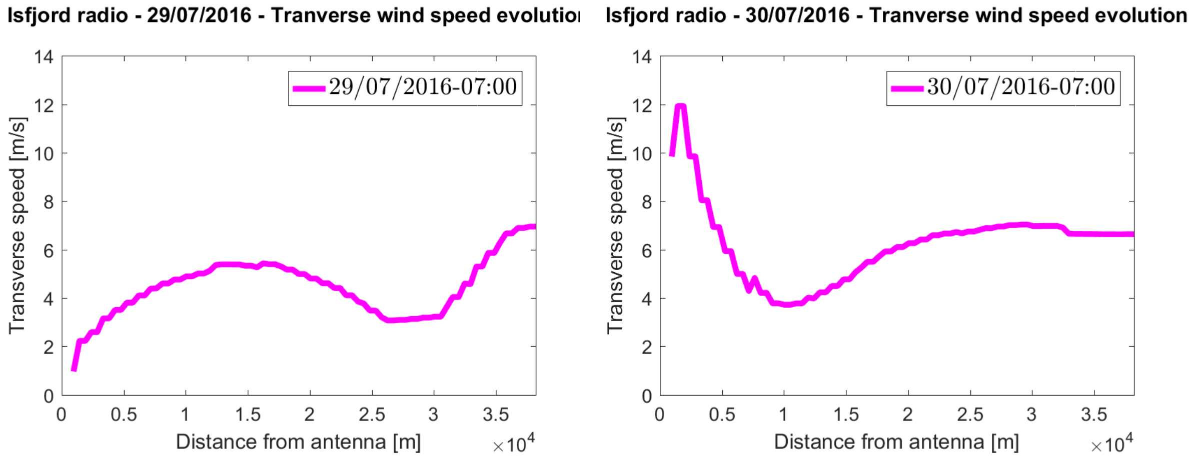

Figure 5.6 – Transverse wind speed evolution along the link on the 1^{st},2^{sd},3^{th},4^{th},7^{th},10^{th},15^{th},20^{th},23^{th},24^{th},29^{th} and the 30^{th} of July

If we now look at the different figures showing the transverse wind speed evolution along the link (see figure 5.6) and their associated spectrum, we can make the following statement : the spectra which are the less smooth and have the most different shape (compared to constant U_t spectra) are the spectra which have the lowest U_t transverse speed evolution along the path.

For example, on the 1^{st},2^{sd}, 15^{th} and the 23^{th} of July, we can see the the U_t evolution along the path is very low (see figure 5.6). If we now look at the same days in figure 5.5, we see that these associated spectra are quite different from the others. Indeed, they all decrease at lower frequencies and therefore, we could say that their transition frequencies are lower.

This is quite logical : if we look at the equation 5.11, we can see that the inferior born of the integral becomes bigger when U_t is decreasing. Consequently, if the inferior born of the integral is increasing then the contribution will be smaller. Hence, we have a spectrum which decreases at lower frequencies. We can thus say that when we have a low evolution of U_t, then the transition frequency is decreasing.

In the constant U_t spectra, we had :

$$\omega_t = 1.43 U_t \left(\frac{k}{L}\right)^{1/2} \tag{5.9}$$

In that case also, the transition frequency was deceasing with U_t.

5.1.5 Comparison of the models with constant and varying U_t with the measurements

In order to see now wheter or not the model with varying U_t is more precise than the previous ones, we will draw it with the measurements and the constant U_t model on the 1^{st},2^{sd},3^{th}, 7^{th}, 10^{th}, 15^{th}, 20^{th}, and 23^{th} of July(see figure 5.7). In red, we have our previous model with constant U_t and varying C_n^2 and in yellow, we have the model with varying U_t.

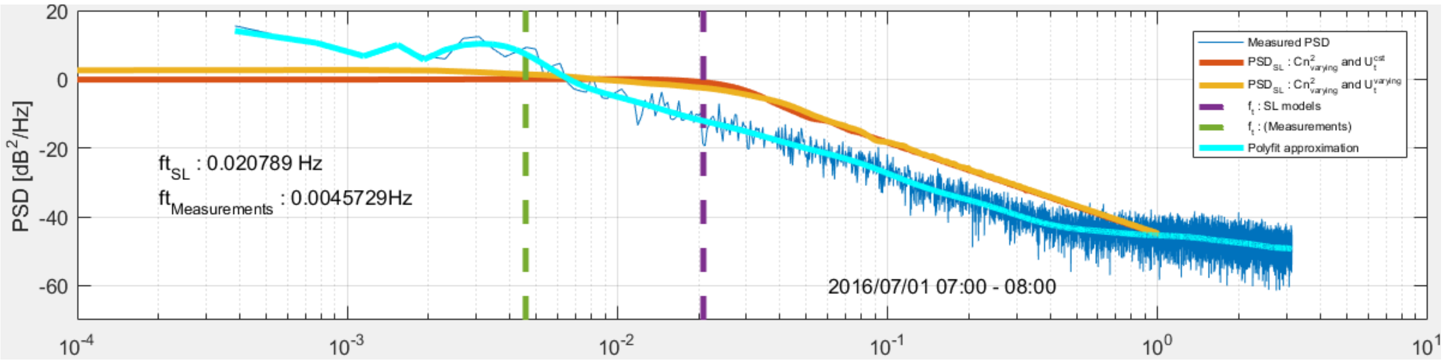

PSD [dB^2/Hz]
ft_{SL} : 0.020789 Hz
$ft_{Measurements}$: 0.0045729Hz
2016/07/01 07:00 - 08:00
Measured PSD
PSD_{SL} : $Cn^2_{varying}$ and U_t^{cst}
PSD_{SL} : $Cn^2_{varying}$ and $U_t^{varying}$
f_t : SL models
f_t : (Measurements)
Polyfit approximation

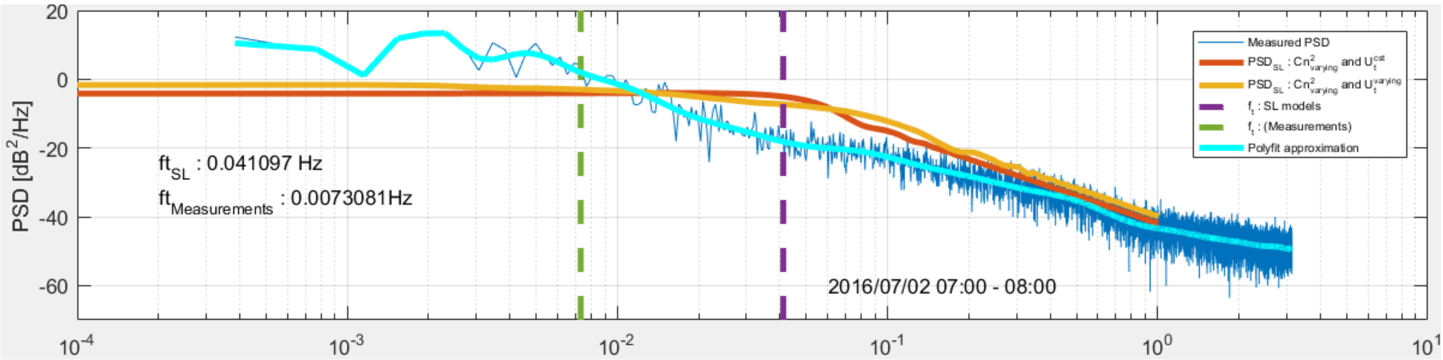

PSD [dB^2/Hz]
ft_{SL} : 0.041097 Hz
$ft_{Measurements}$: 0.0073081Hz
2016/07/02 07:00 - 08:00
Measured PSD
PSD_{SL} : $Cn^2_{varying}$ and U_t^{cst}
PSD_{SL} : $Cn^2_{varying}$ and $U_t^{varying}$
f_t : SL models
f_t : (Measurements)
Polyfit approximation

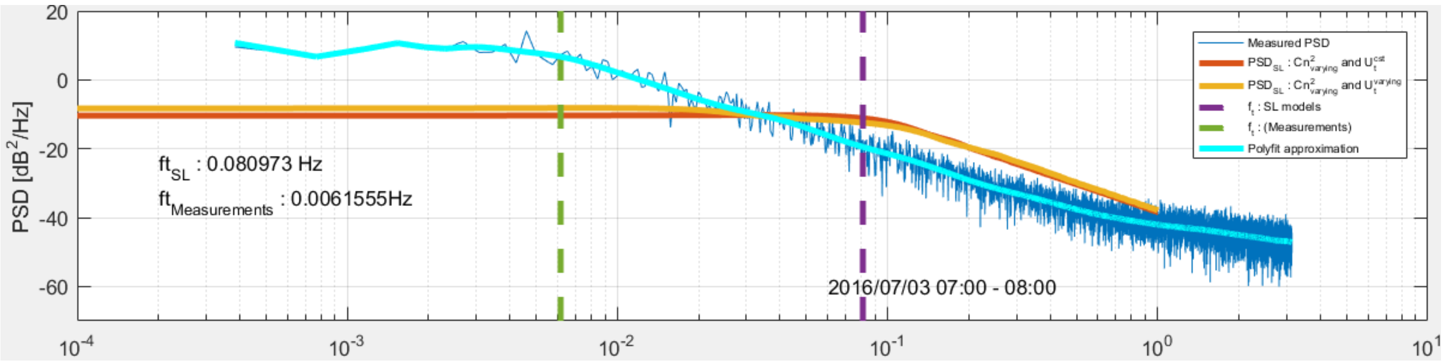

PSD [dB^2/Hz]
ft_{SL} : 0.080973 Hz
$ft_{Measurements}$: 0.0061555Hz
2016/07/03 07:00 - 08:00
Measured PSD
PSD_{SL} : $Cn^2_{varying}$ and U_t^{cst}
PSD_{SL} : $Cn^2_{varying}$ and $U_t^{varying}$
f_t : SL models
f_t : (Measurements)
Polyfit approximation

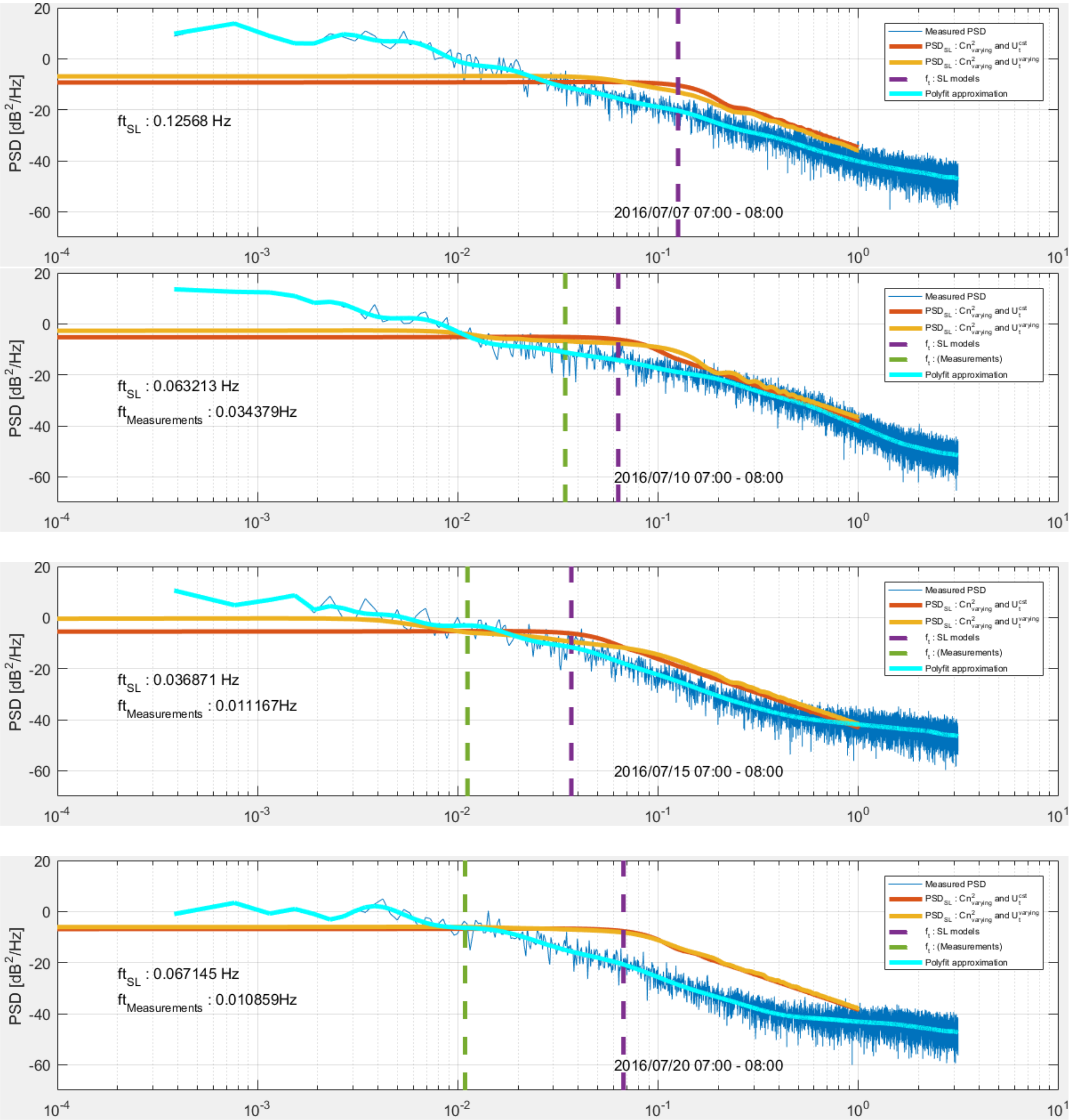

PSD [dB²/Hz]
Measured PSD
PSD_SL : Cn²_varying and U_t^cst
PSD_SL : Cn²_varying and U_t^varying
f_t : SL models
f_t : (Measurements)
Polyfit approximation
ft_SL : 0.12568 Hz
2016/07/07 07:00 - 08:00
ft_SL : 0.063213 Hz
ft_Measurements : 0.034379Hz
2016/07/10 07:00 - 08:00
ft_SL : 0.036871 Hz
ft_Measurements : 0.011167Hz
2016/07/15 07:00 - 08:00
ft_SL : 0.067145 Hz
ft_Measurements : 0.010859Hz
2016/07/20 07:00 - 08:00

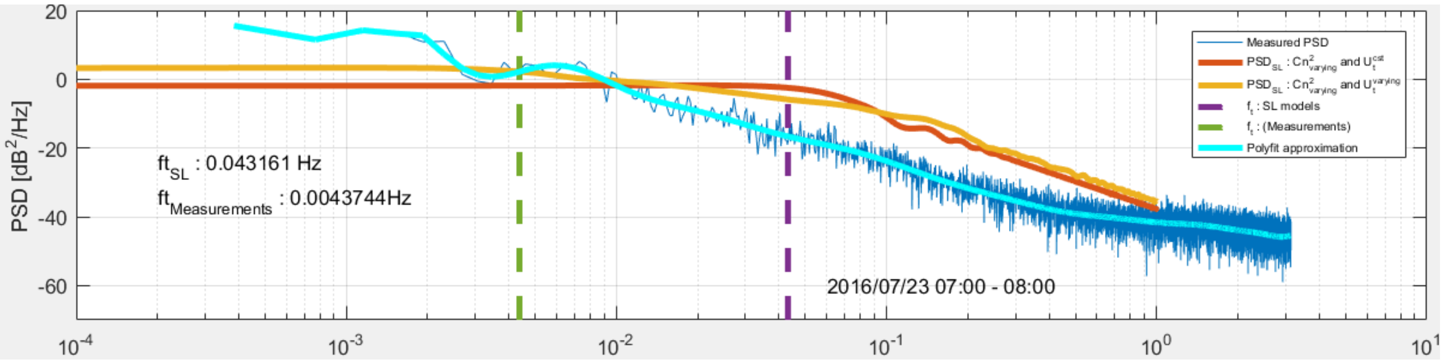

Figure 5.7 – Scintillation measurements versus our two models with constant and varying U_t on the 1^{st},2^{sd},3^{th}, 7^{th}, 10^{th}, 15^{th}, 20^{th}, and 23^{th} of July

From the figures 5.7, we see that when we are in logarithmic scale, our two models (with constant or varying U_t) are very similar. Indeed, if we look at the figures 5.5 and 5.3 showing the spectra from the two methods, we may think that our model are quite different but in logarithmic scale this is not the case.

We can also see that the shapes of our PSD model with varying U_t are not uniform along the days (as it was noticed from the spectra in figure 5.5). Indeed, if we look for example at our PSD model with varying U_t in yellow on the 2^{sd}, the 10^{th} and 15^{th}, we can see that the shapes are different. It is more difficult to see since we are now in logarithmic scale.

It is difficult to say if one model is better than the other. Even though they have some differences, they stay quite similar. The transition frequencies of both models are still too high compared to the one of the measurements. However, in general, we can see that in our model with varying U_t, the amplitude is slightly higher at low frequencies than the model with constant U_t and is thus a little bit closer to the measurement at these frequencies.

So far, we have always had too high transition frequencies. To solve this problem, we will try another hypothesis : $\sqrt{\lambda L} >> L_0$. As a reminder, we have computed before that :

$$\sqrt{\lambda L} = 24.5722m \tag{5.10}$$

In order to meet this hypothesis, L_0 must be thus lower than 24.5722 m.

5.2 Analyse of the second spectrum model when $\sqrt{\lambda L} >> L_0$

In the previous chapter, we computed the expression of the spectrum when $\sqrt{\lambda L} >> L_0$ in the case of varying C_n^2. The expression can be seen again in the following equation :

$$W_\chi(\omega) = 16\pi k^2 \sum_0^L C_n^2(\eta) d\eta \int_{\omega/U_t}^{\infty} \Phi_{vk}^{(0)}(\kappa)[(\kappa U_t)^2 - \omega^2]^{-1/2} \kappa d\kappa \tag{5.11}$$

As we did it in the previous section, we will first consider that U_t is constant along the the liaison.

As a reminder, the Von Karman spectrum has the following expression :

$$\Phi_n^{(vk)}(\kappa) = 0.033\ C_n^2(\frac{\vec{r_1} + \vec{r_2}}{2})(\kappa_L^2 + \kappa^2)^{-11/3} exp(-\kappa^2/\kappa_m^2) \qquad 2\pi/L_0 < \kappa \qquad (5.12)$$

Looking at this equation,we see now that we need to know the exact value of L_0. In order to meet our hypothesis, we need it to be lower than 24.7 m. We also know that L_0 is always between 10 m and 100 m. We have thus the following range for L_0 :

$$L_0 \in [10, 24.7] \qquad (5.13)$$

Hence, we will take the four cases in our simulations :

- $L_0 = 10$ m
- $L_0 = 15$ m
- $L_0 = 20$ m
- $L_0 = 24.5$ m

Now that we have chosen the values of L_0, we are going to have a look at the shape of the temporal frequency spectrum of the log-amplitude fluctuation.

5.2.1 The temporal frequency spectrum of χ when $\sqrt{\lambda L} >> L_0$

In the figure 5.8 and 5.9, we can see the temporal frequency spectrum in the four cases on the 3^{th} and the 10^{th} of July.

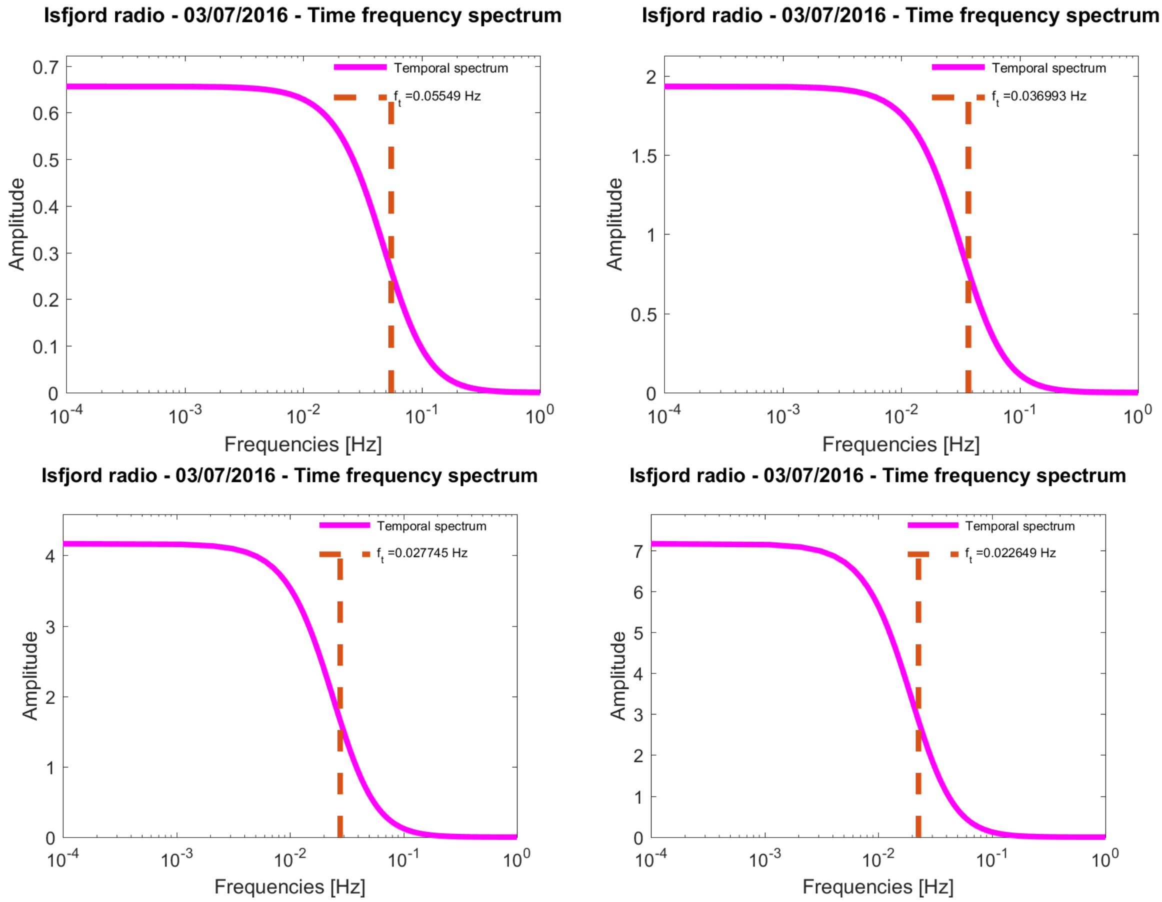

Figure 5.8 – Time-frequency spectrum when $\sqrt{\lambda L} >> L_0$ for $L_0 = 10$ (top left),15 (top right),20 (bottom left) and 24.5 m (bottom right) on the 3^{th} of July

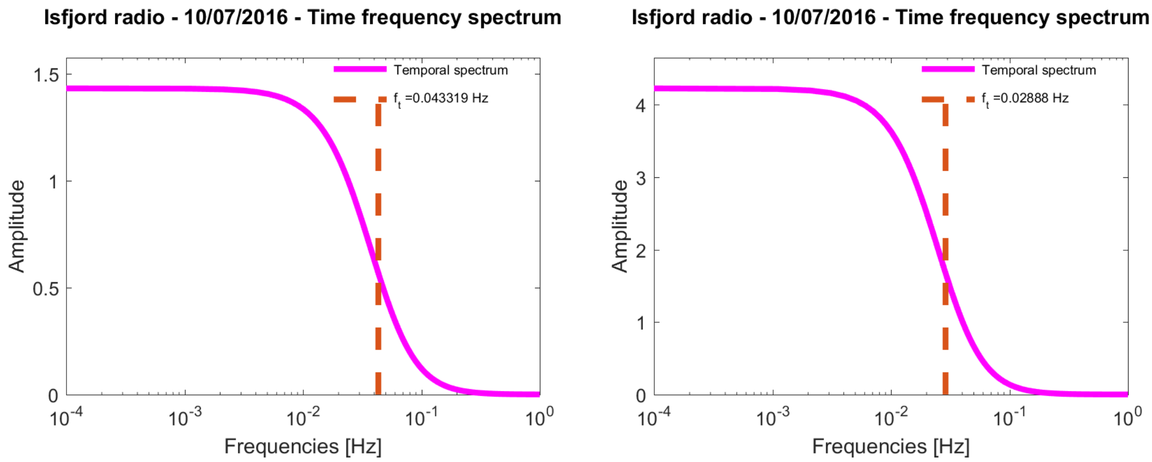

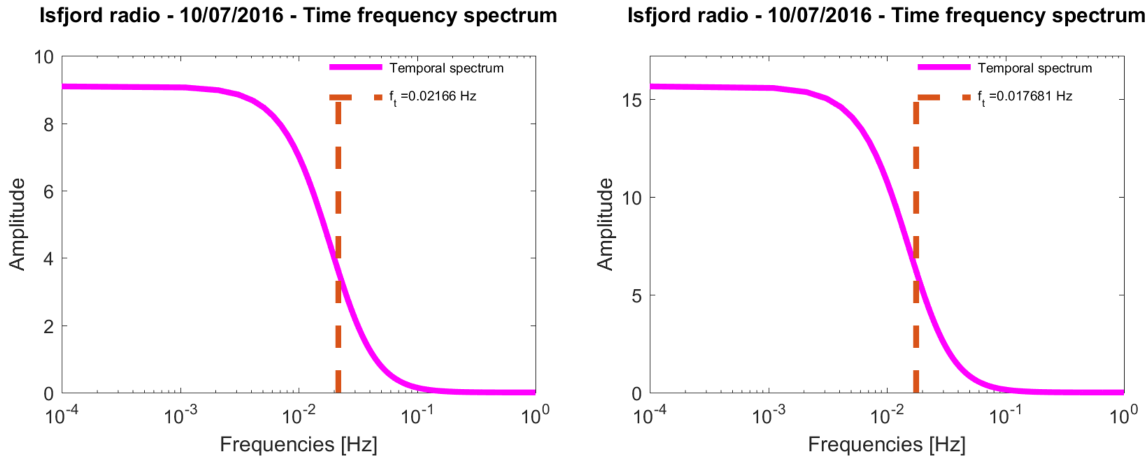

Figure 5.9 – Time-frequency spectrum when $\sqrt{\lambda L} >> L_0$ for $L_0 = 10$ (top left),15 (top right),20 (bottom left) and 24.5 m (bottom right) on the 10^{th} of July

From these two figures, we see that the shape of the spectra is very similar to the ones when $\sqrt{\lambda L} << L_0$. However, as we can see in the figures 5.8 and 5.9, the transition frequency is much smaller when considering this hypothesis. Also, if we compare the four different L_0, we see that the transition frequency decreases when L_0 is increasing. This is quite expected since we computed before that when $\sqrt{\lambda L} >> L_0$:

$$\omega_t = \frac{U_t}{2\pi L_0} \tag{5.14}$$

For example, on the 10^{th} of July, $f_t = 0.043Hz$ when $L_0 = 10\ m$ and $f_t = 0.017$ when $L_0 = 24.5\ m$. Beside that, there are no major differences between the four cases except the amplitude which increases with L_0.

We will now see if this second method is better than the first one.

5.2.2 Comparison of the model where $\sqrt{\lambda L} >> L_0$ with the measurements

In the figure 5.10, we can see our model where $\sqrt{\lambda L} >> L_0$ side by side with the measurements on the 1^{st}, 3^{th}, 5^{th}, 9^{th}, 10^{th}, 13^{th}, 15^{th} and 17^{th} of July. On each figure, we can see the four cases corresponding to the four L_0 and their associated transition frequency.

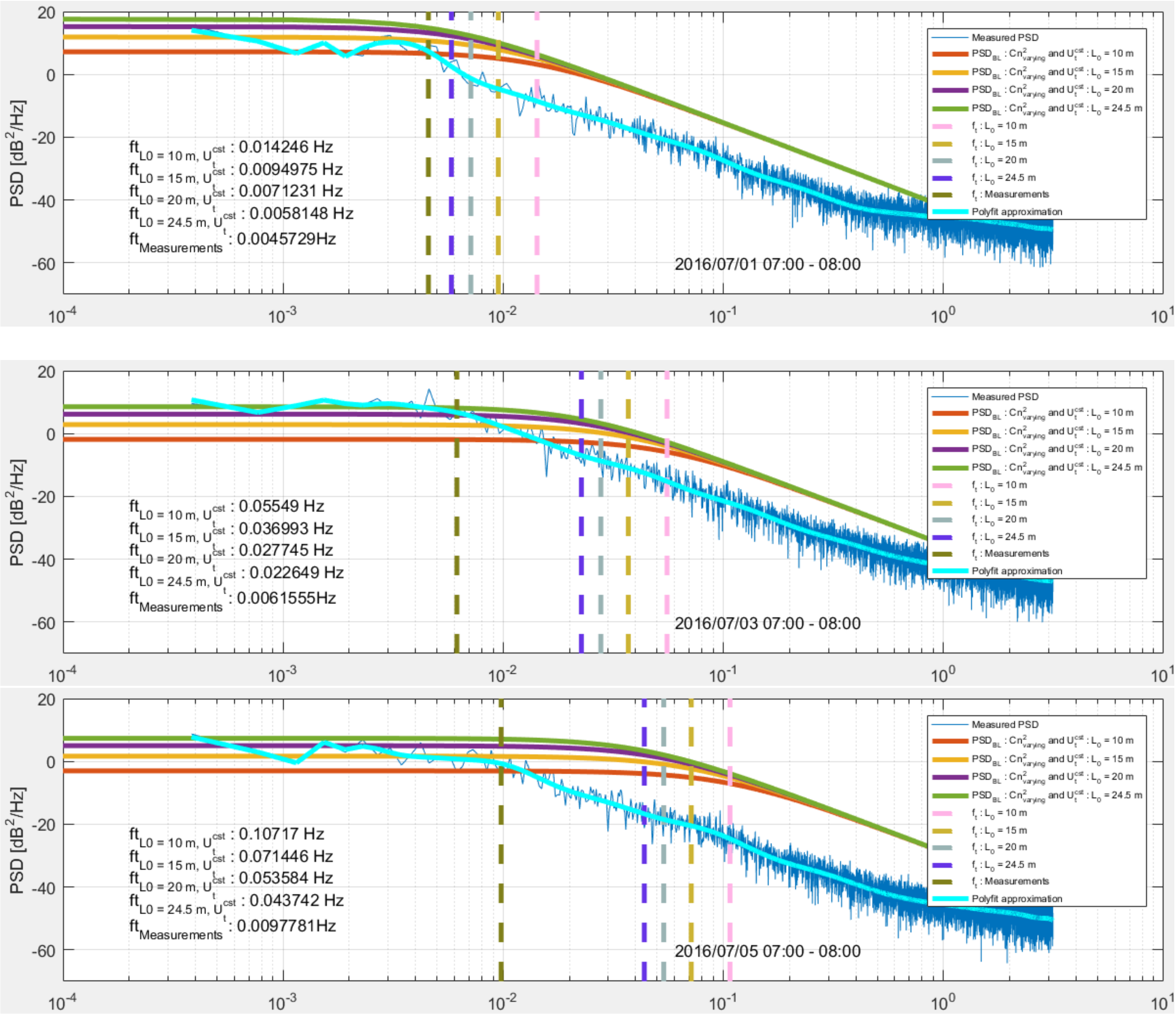

PSD [dB²/Hz]
ft_{L0 = 10 m, U_t^{cst}} : 0.014246 Hz
ft_{L0 = 15 m, U_t^{cst}} : 0.0094975 Hz
ft_{L0 = 20 m, U_t^{cst}} : 0.0071231 Hz
ft_{L0 = 24.5 m, U_t^{cst}} : 0.0058148 Hz
ft_{Measurements} : 0.0045729Hz
2016/07/01 07:00 - 08:00
Measured PSD
PSD_BL : Cn²_varying and U_t^cst : L_0 = 10 m
PSD_BL : Cn²_varying and U_t^cst : L_0 = 15 m
PSD_BL : Cn²_varying and U_t^cst : L_0 = 20 m
PSD_BL : Cn²_varying and U_t^cst : L_0 = 24.5 m
f_t : L_0 = 10 m
f_t : L_0 = 15 m
f_t : L_0 = 20 m
f_t : L_0 = 24.5 m
f_t : Measurements
Polyfit approximation
ft_{L0 = 10 m, U_t^{cst}} : 0.05549 Hz
ft_{L0 = 15 m, U_t^{cst}} : 0.036993 Hz
ft_{L0 = 20 m, U_t^{cst}} : 0.027745 Hz
ft_{L0 = 24.5 m, U_t^{cst}} : 0.022649 Hz
ft_{Measurements} : 0.0061555Hz
2016/07/03 07:00 - 08:00
ft_{L0 = 10 m, U_t^{cst}} : 0.10717 Hz
ft_{L0 = 15 m, U_t^{cst}} : 0.071446 Hz
ft_{L0 = 20 m, U_t^{cst}} : 0.053584 Hz
ft_{L0 = 24.5 m, U_t^{cst}} : 0.043742 Hz
ft_{Measurements} : 0.0097781Hz
2016/07/05 07:00 - 08:00

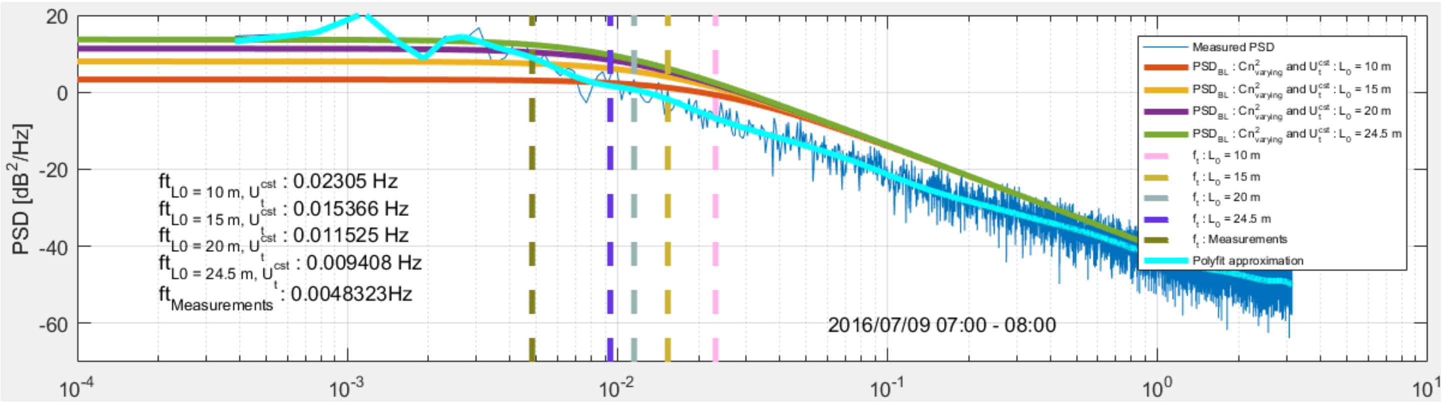
PSD [dB²/Hz]
ft L0 = 10 m, U t cst : 0.02305 Hz
ft L0 = 15 m, U t cst : 0.015366 Hz
ft L0 = 20 m, U t cst : 0.011525 Hz
ft L0 = 24.5 m, U t cst : 0.009408 Hz
ft Measurements : 0.0048323Hz
2016/07/09 07:00 - 08:00
Measured PSD
PSD BL : Cn² varying and U t cst : L0 = 10 m
PSD BL : Cn² varying and U t cst : L0 = 15 m
PSD BL : Cn² varying and U t cst : L0 = 20 m
PSD BL : Cn² varying and U t cst : L0 = 24.5 m
f t : L0 = 10 m
f t : L0 = 15 m
f t : L0 = 20 m
f t : L0 = 24.5 m
f t : Measurements
Polyfit approximation

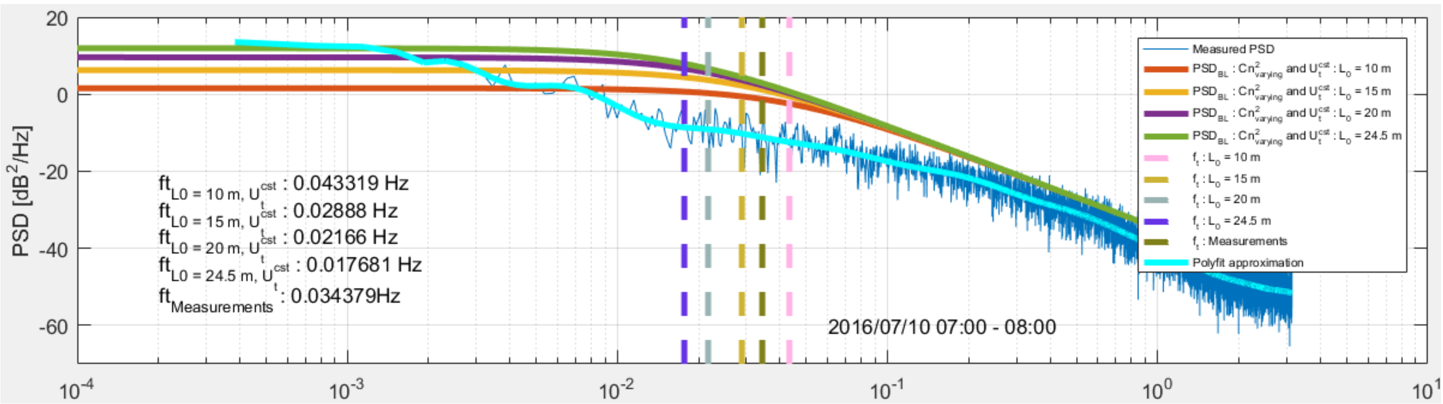
PSD [dB²/Hz]
ft L0 = 10 m, U t cst : 0.043319 Hz
ft L0 = 15 m, U t cst : 0.02888 Hz
ft L0 = 20 m, U t cst : 0.02166 Hz
ft L0 = 24.5 m, U t cst : 0.017681 Hz
ft Measurements : 0.034379Hz
2016/07/10 07:00 - 08:00
Measured PSD
PSD BL : Cn² varying and U t cst : L0 = 10 m
PSD BL : Cn² varying and U t cst : L0 = 15 m
PSD BL : Cn² varying and U t cst : L0 = 20 m
PSD BL : Cn² varying and U t cst : L0 = 24.5 m
f t : L0 = 10 m
f t : L0 = 15 m
f t : L0 = 20 m
f t : L0 = 24.5 m
f t : Measurements
Polyfit approximation

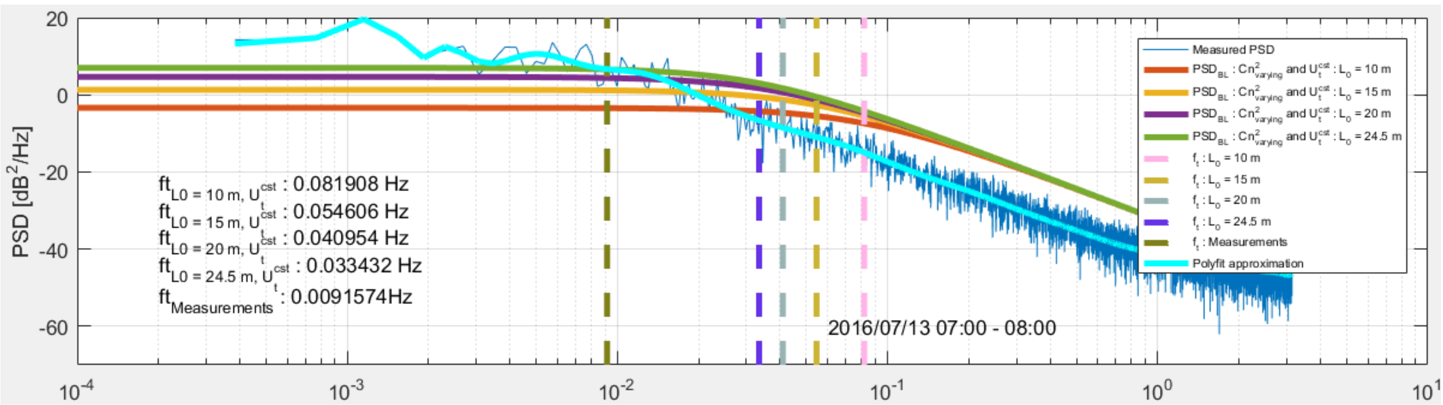
PSD [dB²/Hz]
ft L0 = 10 m, U t cst : 0.081908 Hz
ft L0 = 15 m, U t cst : 0.054606 Hz
ft L0 = 20 m, U t cst : 0.040954 Hz
ft L0 = 24.5 m, U t cst : 0.033432 Hz
ft Measurements : 0.0091574Hz
2016/07/13 07:00 - 08:00
Measured PSD
PSD BL : Cn² varying and U t cst : L0 = 10 m
PSD BL : Cn² varying and U t cst : L0 = 15 m
PSD BL : Cn² varying and U t cst : L0 = 20 m
PSD BL : Cn² varying and U t cst : L0 = 24.5 m
f t : L0 = 10 m
f t : L0 = 15 m
f t : L0 = 20 m
f t : L0 = 24.5 m
f t : Measurements
Polyfit approximation

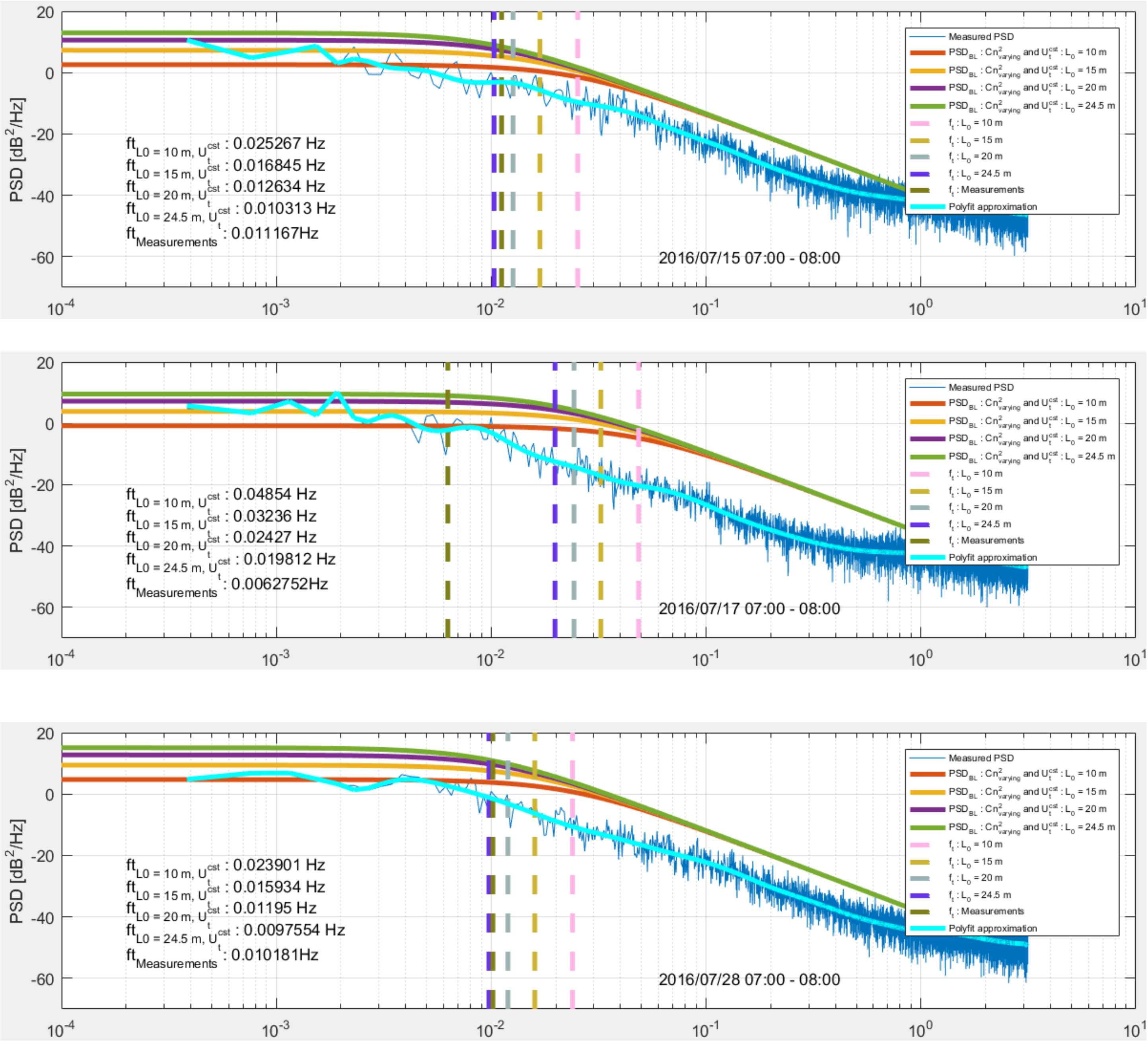

Figure 5.10 – Scintillation measurements versus our model when $\sqrt{\lambda L} >> L_0$ on the 1^{st}, 3^{th}, 5^{th}, 9^{th}, 10^{th}, 13^{th}, 15^{th} and 17^{th} of July of July

As it was said before, with this hypothesis, the transition frequency is much lower than before. If we look at figure 5.10, we can see that the transition frequencies of our models are approximately aligned with the ones from the measurements on several days. Indeed, if we look at the figure on the 1^{st}, 10^{th}, 15^{th} and the 28^{th} of July, we see that the measured transition frequency is extremely close to the ones of our models.

For example, on the 15^{th}, we have :

$$f_t(measurements) = 0.011167Hz$$

$$f_t(L_0 = 24.5m) = 0.010313Hz$$

The difference is really small (less than 8 %).

On the other days, the transition frequency of our model is again too high (but not as high as when $\sqrt{\lambda L} << L_0$). It is important to recall here that the measured transition frequency has been computed using a variance-based method and is more of an indication of where the transition frequency is placed than a fixed value. Therefore, we must accord more importance to the shape of the spectra than to the transition frequency in itself.

For example, on the 3^{th} of July, there is a non-negligible difference between the measured and modelled transition frequencies but the shapes of both models and measurements are quite close. Concerning the amplitude, this model is much better than before. As a reminder, in the previous model where $\sqrt{\lambda L} << L_0$, the amplitude at low frequencies was always too low (see figure 5.4). Here, our amplitude at low frequencies is almost always of the same order of amplitude as the measurements. At higher frequencies, the amplitude of our model is always a little bit too high but this is often due to a too large transition frequency.

Without any doubt, we can say that this model is much better than the previous one. The hypothesis of $\sqrt{\lambda L} >> L_0$ seems to be the best in this case. This is quite logical : since our antenna has a particularly low elevation angle (3 °), the length of our link through the turbulent atmoshpere is much longer than for antenna with usual elevation angle (like 30 °). Consequently, since our L is large, it makes sense to confirm the hypothesis $\sqrt{\lambda L} >> L_0$.

As we did before, we will now test our model with a varying transverse wind speed.

5.2.3 The temporal frequency spectrum with varying U_t when $\sqrt{\lambda L} >> L_0$

In the figures 5.11, 5.12 and 5.13, we can see the spectrum of our model where $\sqrt{\lambda L} >> L_0$ and U_t is varying on the 3^{th}, 15^{th}, and the 22^{th} of July.

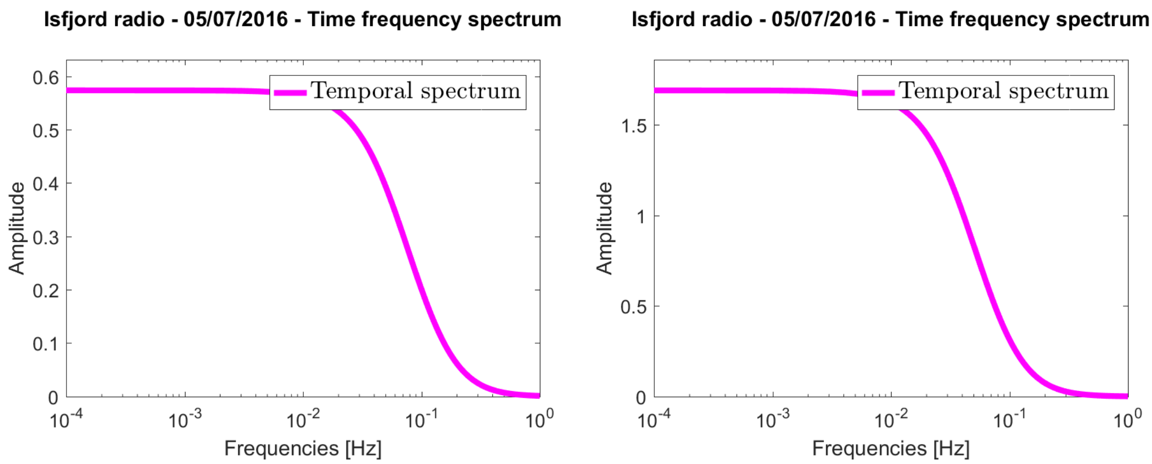

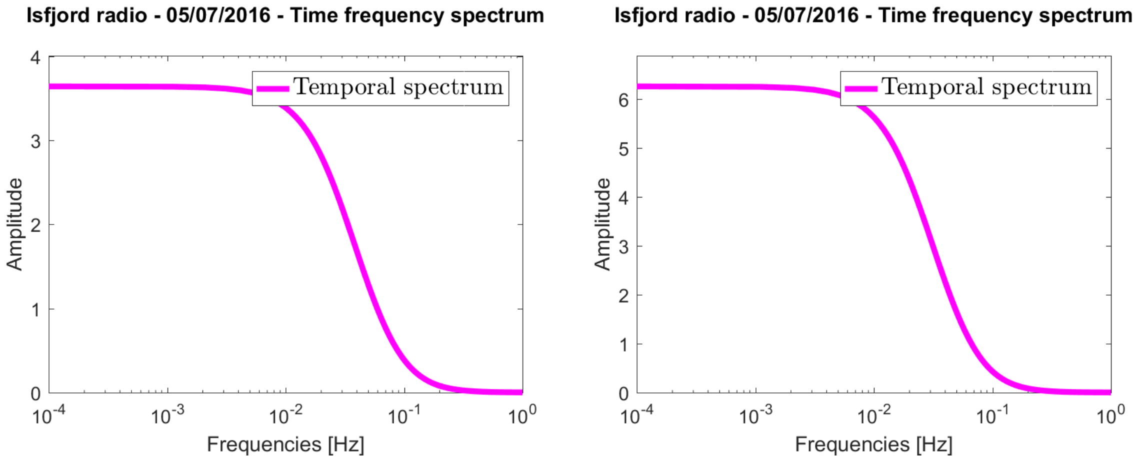

Figure 5.11 – Time-frequency spectrum when $\sqrt{\lambda L} >> L_0$ for $L_0 = 10$ (top left),15 (top right),20 (bottom left) and 24.5 m (bottom right) on the 5^{th} of July

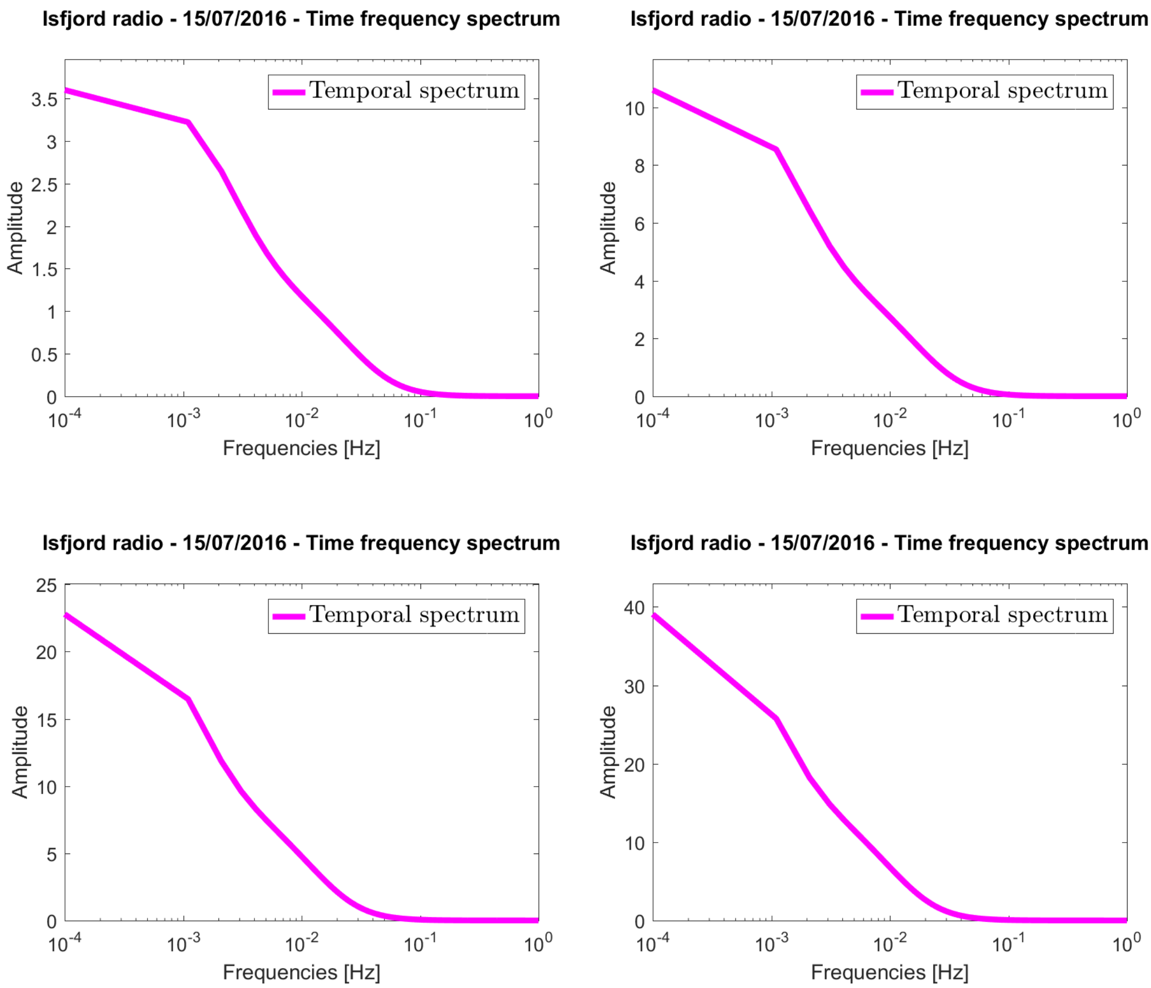

Figure 5.12 – Time-frequency spectrum when $\sqrt{\lambda L} >> L_0$ for $L_0 = 10$ (top left),15 (top right),20 (bottom left) and 24.5 m (bottom right) on the 15^{th} of July

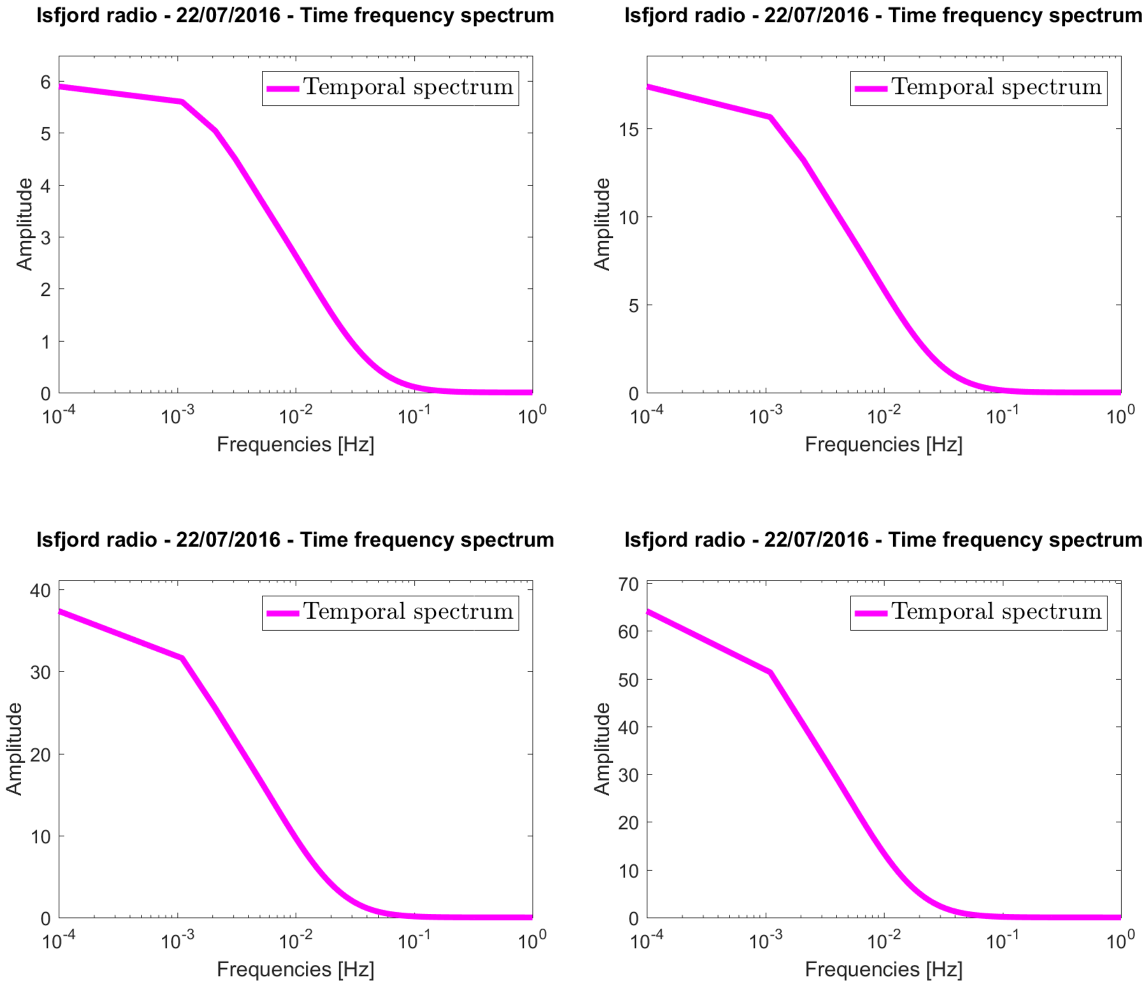

Figure 5.13 – Time-frequency spectrum when $\sqrt{\lambda L} >> L_0$ for $L_0 = 10$ (top left),15 (top right),20 (bottom left) and 24.5 m (bottom right) on the 22^{th} of July

As we can see in the 3 figures, the shape is not uniform along the days. Indeed if we look on the 3^{th} or the 15^{th}, the shapes of the spectra are completely different. While on the 3^{th}, we have a smooth curve, on the 15^{th} and the 22^{th} of July, we have an inflexion point around $10^{-3} Hz$.

In order to explain this inflexion point, we will have a look at the evolution of the transverse wind speed along the link on the 3 dates.

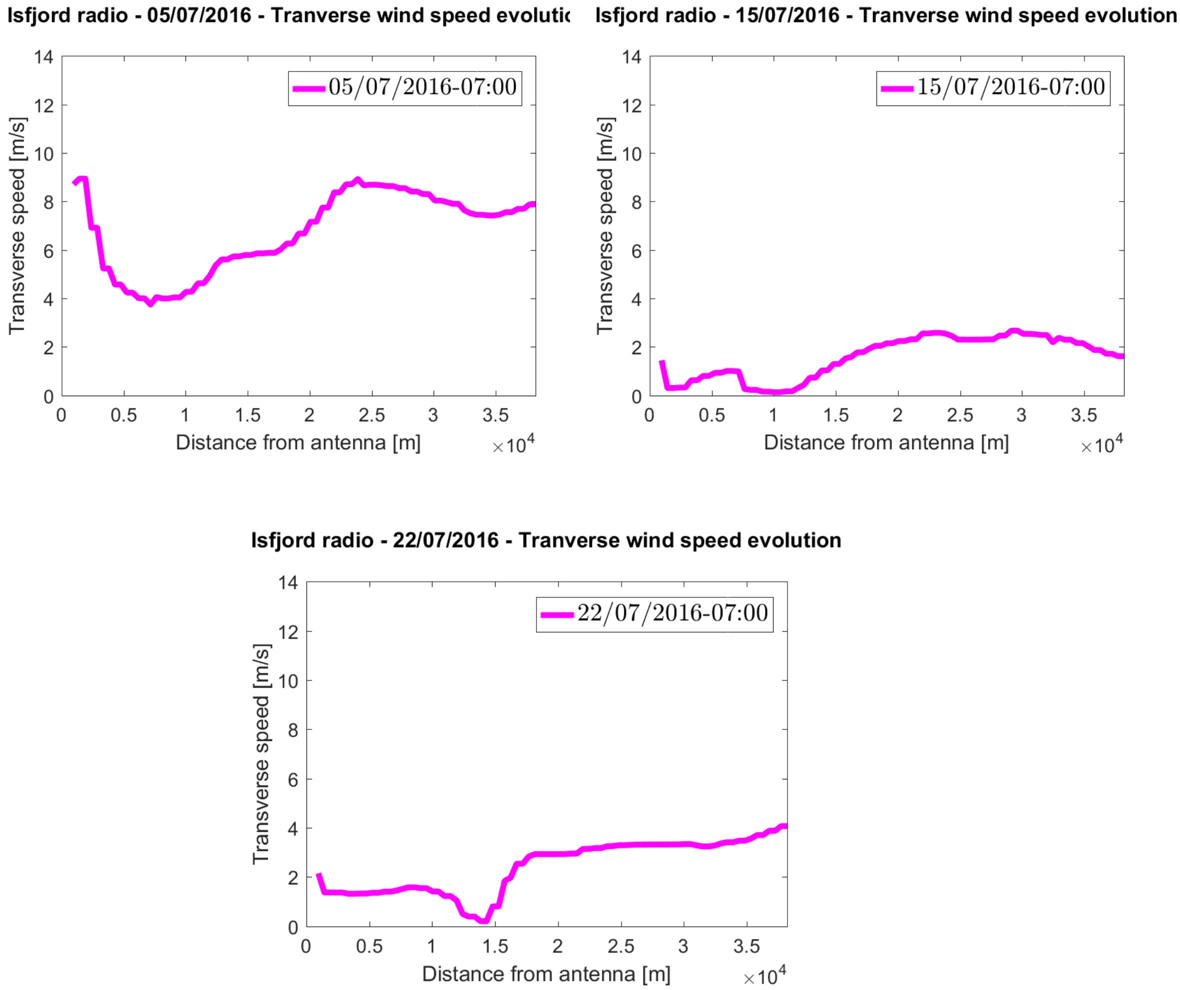

Figure 5.14 – Transverse wind speed evolution

In the figure 5.14, we can see that on the 15^{th} and the 22^{th}, the transverse wind speed is quite low along the path and is most of the time below 3 m/s. However, on the 5^{th}, the transverse wind speed is much higher and always around 5 m/s.

If we now look again at the spectrum (see figures 5.11, 5.12 and 5.13), we see that the spectra with an inflexion point corresponds to the dates where the U_t evolution was low. It is the same phenomenon we had in the previous model where $\sqrt{\lambda L} << L_0$. When we have a low U_t, the inferior born of the integral (see equation 5.11) is higher and the contribution to the spectrum is thus smaller.

Moreover, we see that this effect is stronger when L_0 is larger. This is due to the $(\kappa^2 + \frac{1}{L_0^2})^{-11/6}$ term which, at low frequencies, will increase with L_0 . Consequently the contribution to the integral will be larger and the amplitude will increase. Therefore, increasing the inferior born will have a stronger effect on the spectrum. This is the reason why the effect of U_t is stronger when L_0 is high.

Concerning the transition frequencies, they seem to decrease with the transverse speed. It is linked to the higher inferior born of the integral. As we can see, the conclusion is quite similar to the one we had in the previous model where $\sqrt{\lambda L} >> L_0$ with varying U_t.

Now we will compare this model with the measurements and see if it is better when considering a varying U_t.

5.2.4 Comparison of the model with varying U_t where $\sqrt{\lambda L} >> L_0$ with the measurements

In the figure 5.15, we can see the comparison between the spectrum with varying and constant U_t when $\sqrt{\lambda L} >> L_0$ in th case where $L_0 = 20m$.

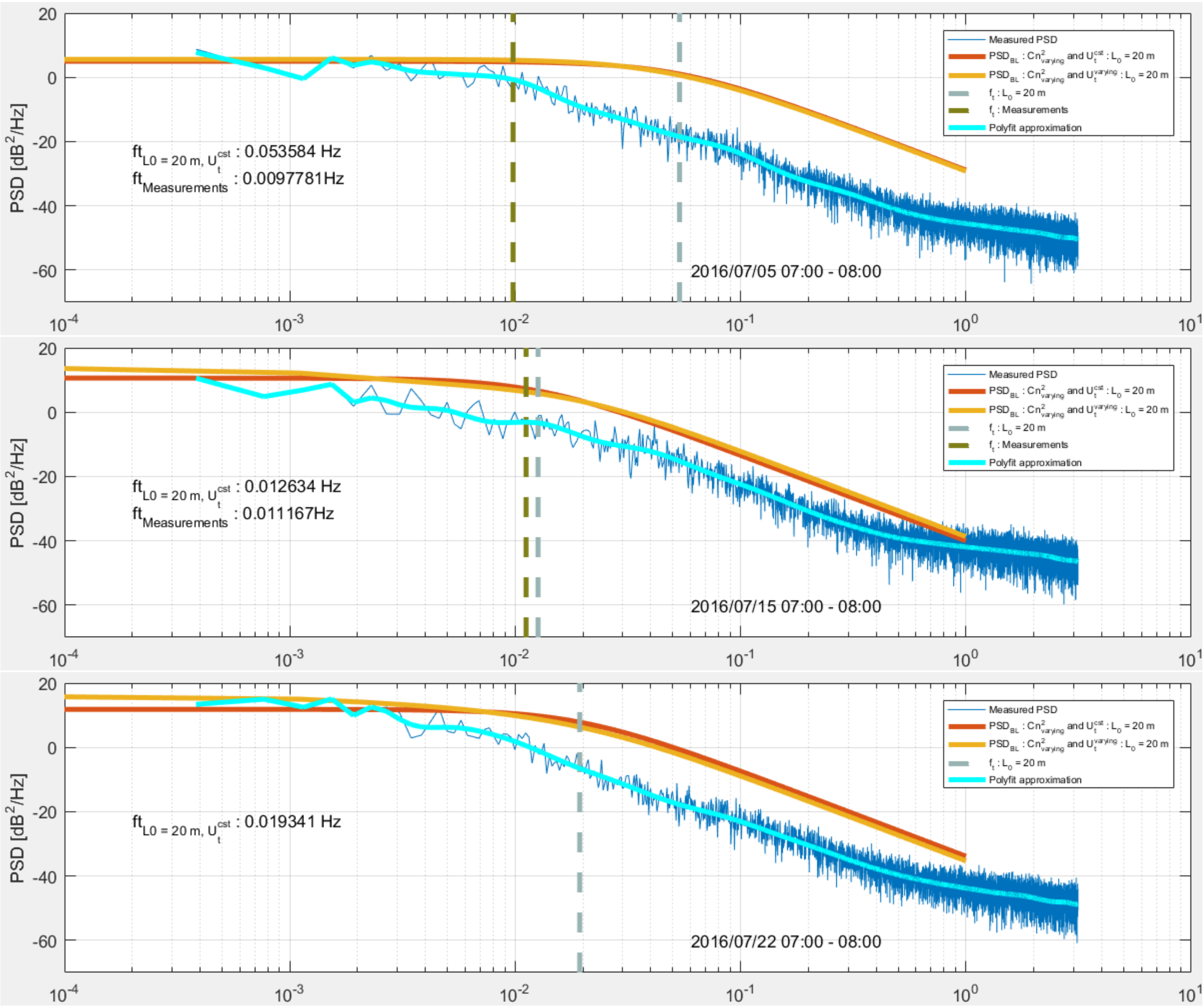

Figure 5.15 – Scintillation measurements versus our model when $\sqrt{\lambda L} >> L_0$ and that U_t is varying on the 5^{th}, 7^{th} and 22^{th} of July of July

In the figure 5.15, we see that in logarithmic scale, both models are very similar. Using all the data set of the month (not shown here), it appears that the two models are always very close and neither of them seems to be really better than the other.

We will now try a last model which is going to combine the two hypotheses $\sqrt{\lambda L} << L_0$ and $\sqrt{\lambda L} >> L_0$.

5.3 Analyse of the hybrid model

For this last model, we are going to combine the two previous methods and their hypotheses. Our first method supposed the hypothesis that $\sqrt{\lambda L_{link}} << L_0$. If for example, $L_0 = 10\ m$, then we can apply our method only if :

$$L_{link} << \frac{L_0^2}{\lambda} \tag{5.15}$$

In this example, with $\lambda = 0.0158\ m$ (from f = 19 GHz) and $L_0 = 10\ m$, we find that :

$$L_{link} = 6333m \tag{5.16}$$

The first method can thus be applied as long as the length of the link is smaller than 6333 m.

On the other hand, when the length of the link is larger than 6333 m, we have :

$$L_{link} >> \frac{L_0^2}{\lambda} \tag{5.17}$$

Which can be written equivalently to $\sqrt{\lambda L_{link}} >> L_0$ and corresponds to the hypothesis of our second method.

In a previous chapter, we computed that the length of link was equal to 38 215 m. If we want to combine the two methods, we can apply the first model for the 6333 first meters and the second one above 6333 m. If we make this combination, the temporal frequency spectrum will have the following expression :

$$\begin{aligned} W_\chi(\omega) &= 16\pi^2 k^2 \int_0^\infty d\kappa J_0(\kappa U_t \tau) \int_0^L d\eta C_n^2(\vec{r}) \Phi_n^{(o)}(\kappa) sin^2[\frac{\kappa^2(L-\eta)}{2k}][(\kappa U_t)^2 - \omega^2]^{1/2} \kappa d\kappa \\ &= 16\pi^2 k^2 \int_0^\infty d\kappa J_0(\kappa U_t \tau) \int_0^L d\eta C_n^2(\vec{r}) \Phi_n^{(vko)}(\kappa) [(\kappa U_t)^2 - \omega^2]^{1/2} \kappa d\kappa \end{aligned} \tag{5.18}$$

With the equation 5.18, the two methods are combined. In this work, we have tested our hybrid method with $L_0 = 10, 15 and 20m$. In term of the combination, it gives :

L_0	$\sqrt{\lambda L} << L_0$	$\sqrt{\lambda L} >> L_0$
10 m	$L << 6333m$	$L >> 6333m$
15 m	$L << 14250m$	$L >> 14250m$
20 m	$L << 25233m$	$L >> 25233m$

Now, we will see how the temporal frequency spectrum behaves with this hybrid method.

5.3.1 The temporal spectrum with the hybrid method

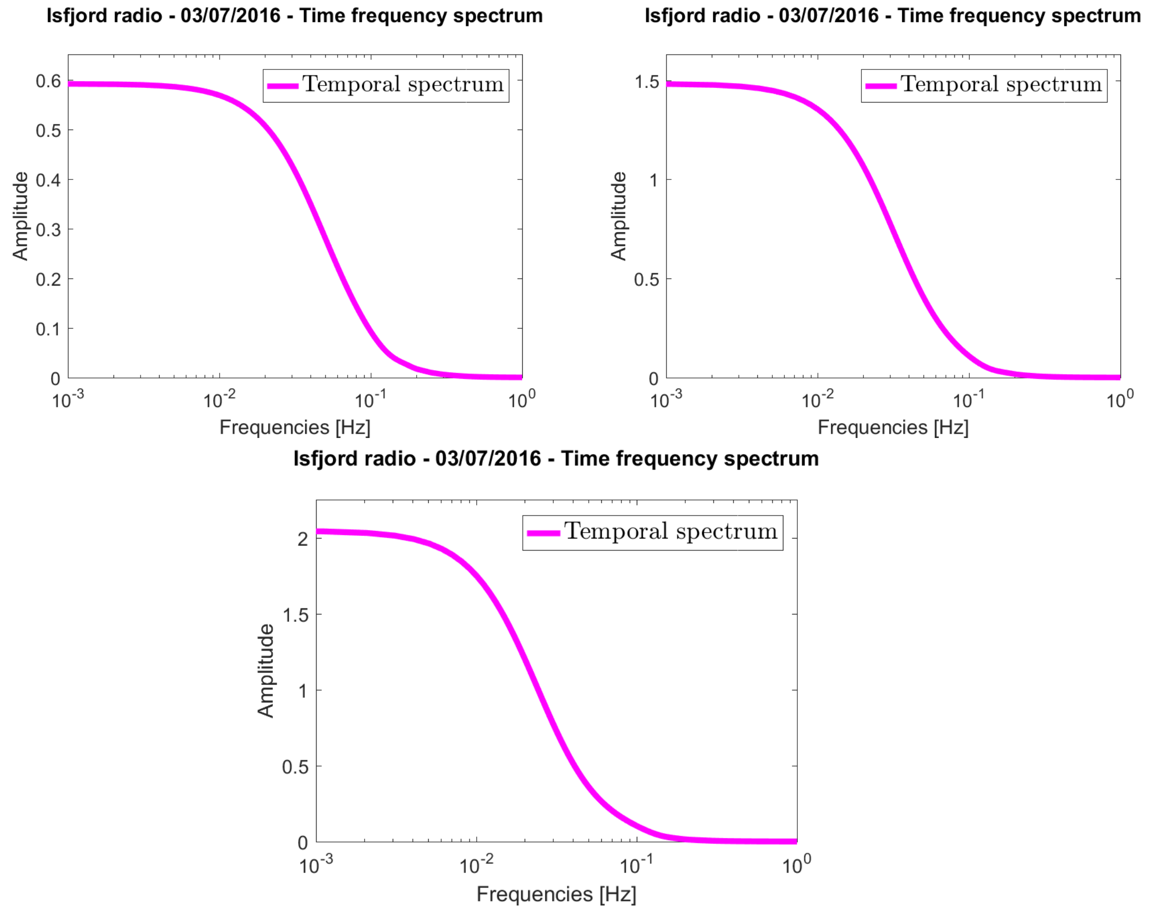

Figure 5.16 – Time-frequency spectrum when hybrid method for $L_0 = 10$ (top left),15 (top right),20 (bottom) on the 3^{th} of July

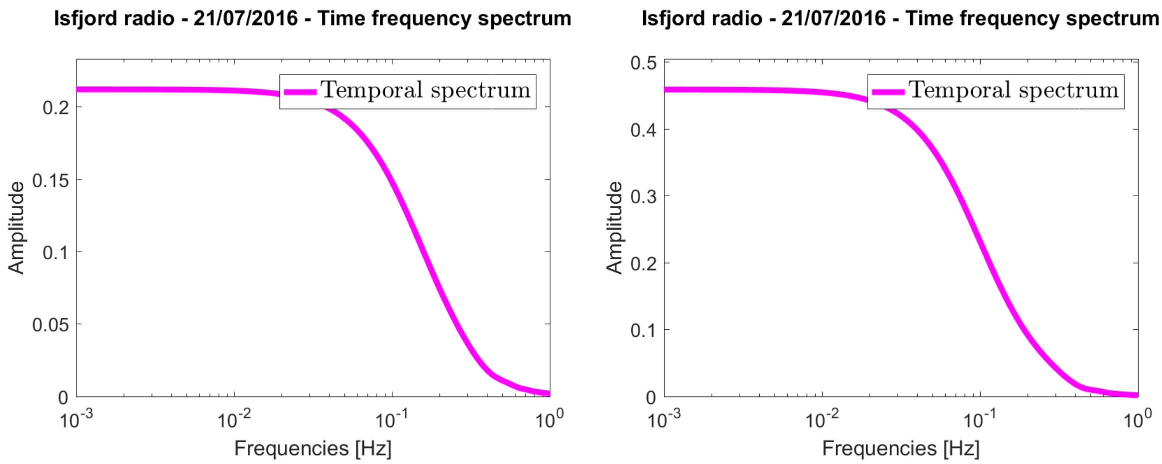

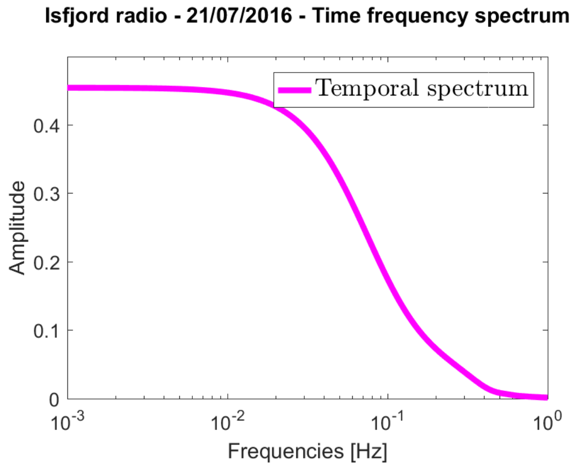

Figure 5.17 – Temporal frequency spectrum with the hybrid method for $L_0 = 10$ (top left), 15 (top right), 20 (bottom) on the 21^{th} of July

We see in the figure 5.19 and 5.20 that the spectra are really smooth. Moreover, we see that the spectrum shifts towards lower frequencies when L_0 increases. We can thus say that increasing L_0 will reduce the transition frequency. This is quite logical since the transition frequency of the second method is equal to $U_t/(2\pi L_0)$.

We will now have a look at the measurements to see if this combined method is better than the others.

5.3.2 Comparison with the measurements

In the figure 5.18, we can see the PSD of our model side by side with the measurements.

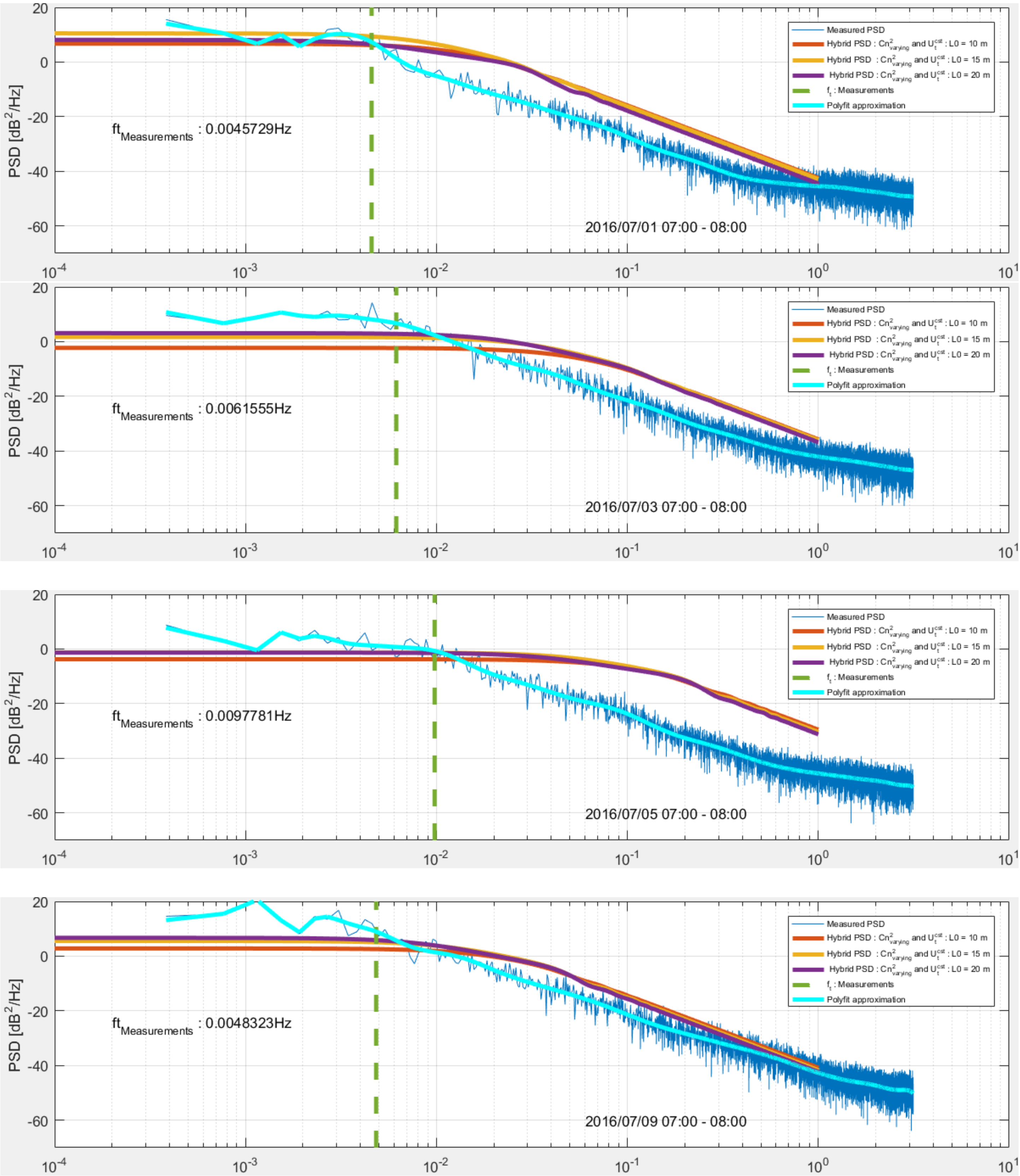
PSD [dB²/Hz]
Measured PSD
Hybrid PSD : Cn²varying and Ucst t : L0 = 10 m
Hybrid PSD : Cn²varying and Ucst t : L0 = 15 m
Hybrid PSD : Cn²varying and Ucst t : L0 = 20 m
ft : Measurements
Polyfit approximation
ftMeasurements : 0.0045729Hz
2016/07/01 07:00 - 08:00
ftMeasurements : 0.0061555Hz
2016/07/03 07:00 - 08:00
ftMeasurements : 0.0097781Hz
2016/07/05 07:00 - 08:00
ftMeasurements : 0.0048323Hz
2016/07/09 07:00 - 08:00

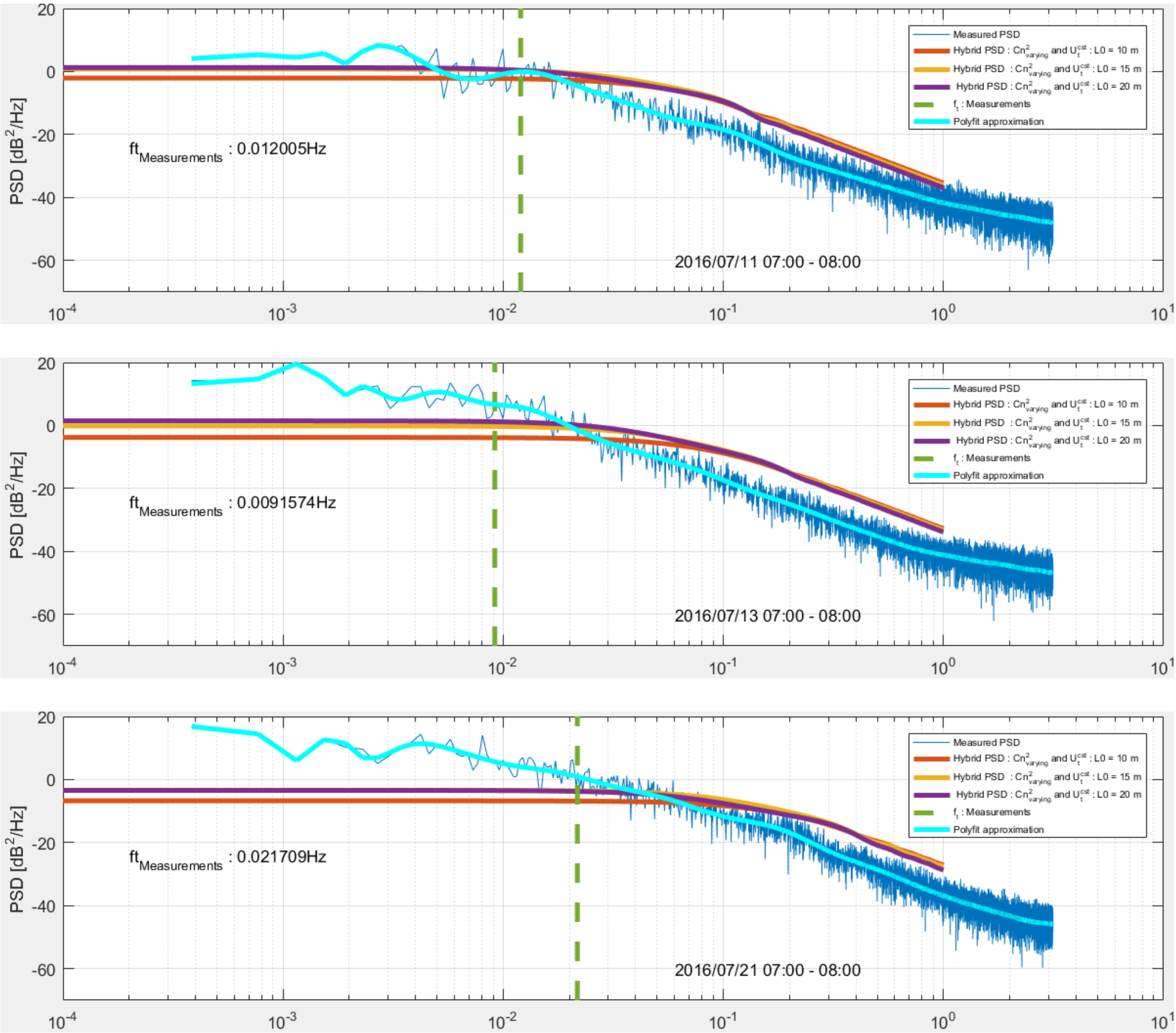

Figure 5.18 – Scintillation measurements versus our hybrid model on the 1^{th}, 3^{th}, 5^{th}, 9^{th}, 11^{th}, 13^{th} and 21^{th} of July

From the figure 5.18, we can see that our hybrid method is quite similar to our second method (see figure 5.10).

At low frequencies, we see that the PSD has a lower amplitude when L_0 decrease which is quite logical when we look at the equation 5.18. The change of L_0 does not seem to change much our PSD model and from the whole data set, it is difficult to say if one of the values of L_0 is better than the others.

At higher frequencies, our PSD models seem to be always a little higher than the measurements. However, on several days, the spectrum is really close to the measurements even at higher frequencies. For example, on the 9^{th} and the 15^{th} of July, our combined model is really similar to the measurements.

At this stage, it is difficult to say if our combined model is really better than the second method where $\sqrt{\lambda L} >> L_0$. We will see later in this chapter which model is the best. Before that, we will test this model with varying transverse wind speed as we did for the other models.

5.3.3 The temporal spectrum with varying Ut

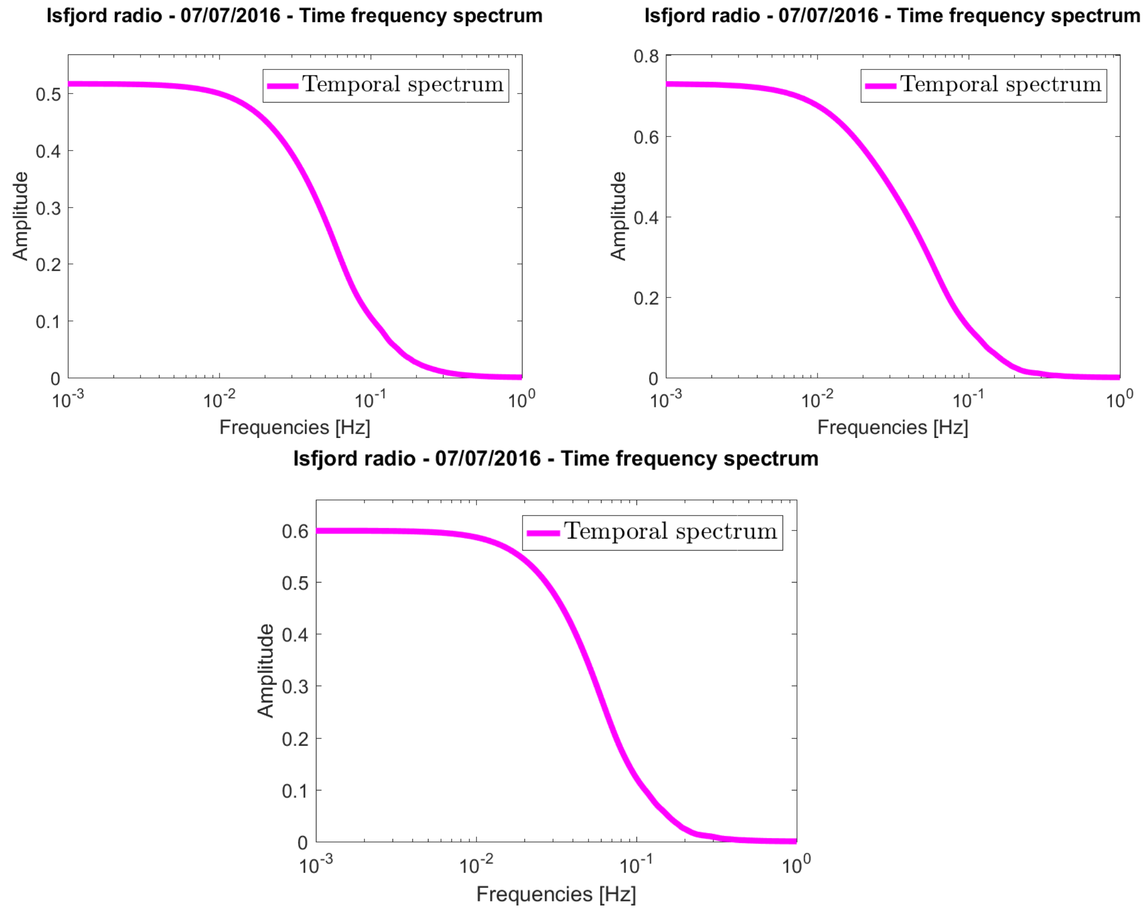

Figure 5.19 – Temporal frequency spectrum when $\sqrt{\lambda L} >> L_0$ for $L_0 = 10$ (top left),15 (top right),20 (bottom) on the 7^{th} of July

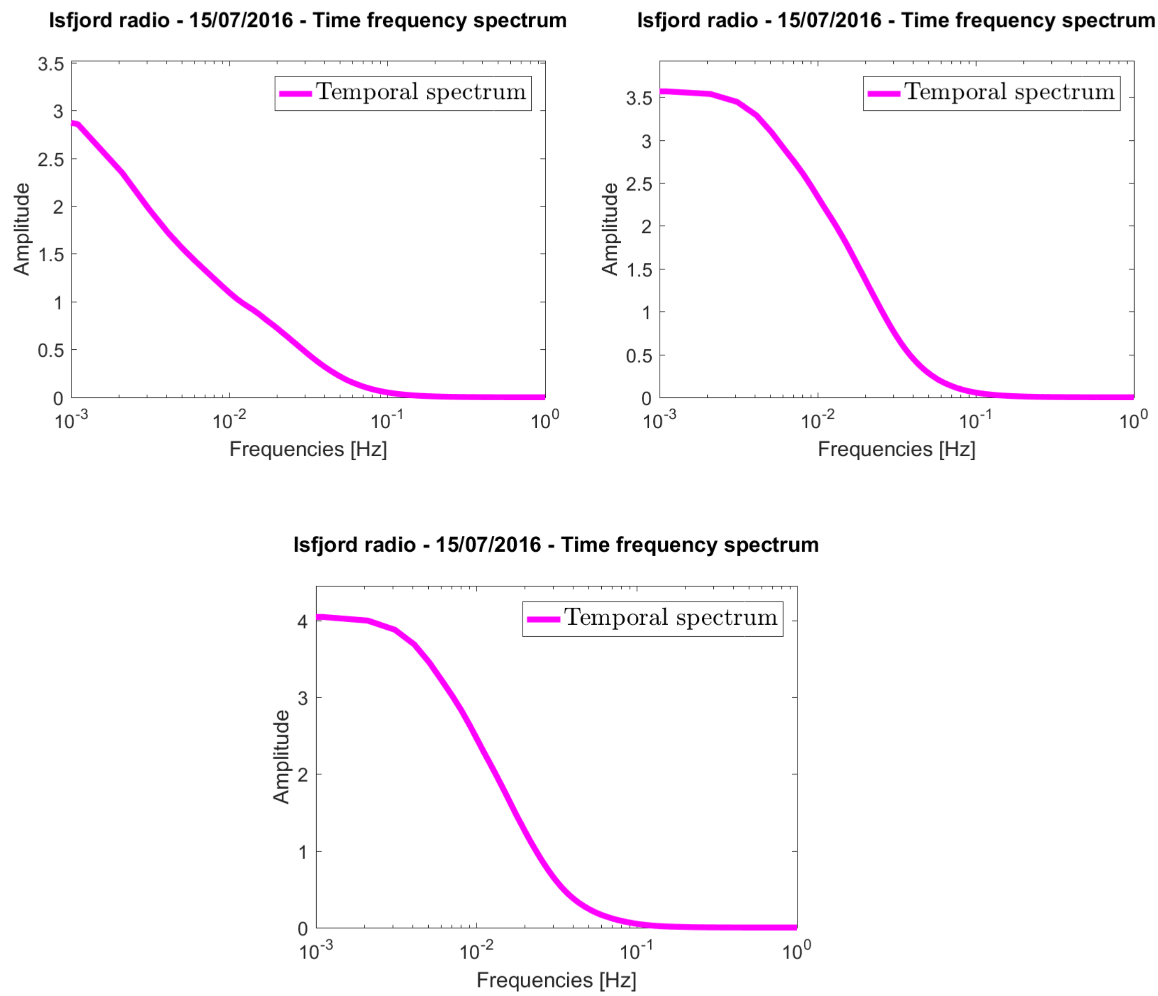

Figure 5.20 – Temporal frequency spectrum when $\sqrt{\lambda L} >> L_0$ for $L_0 = 10$ (top left),15 (top right),20 (bottom) on the 15^{th} of July

As before, when U_t is varying, the spectra are no longer uniform day after day. We can see that on the 15^{th}, the spectrum decreases a lot at low frequencies. This is due to transverse wind speed which is very low along the path(see figure 5.14). As explained in the previous models, the inferior born becomes higher because of the low U_t and the spectrum decreases thus a lot a low frequencies.

5.3.4 Comparison with the measurements

We will now see the comparison of our combined model when U_t is varying or when U_t is constant along the path with the measurements for $L_0 = 15m$ (see figure 5.21).

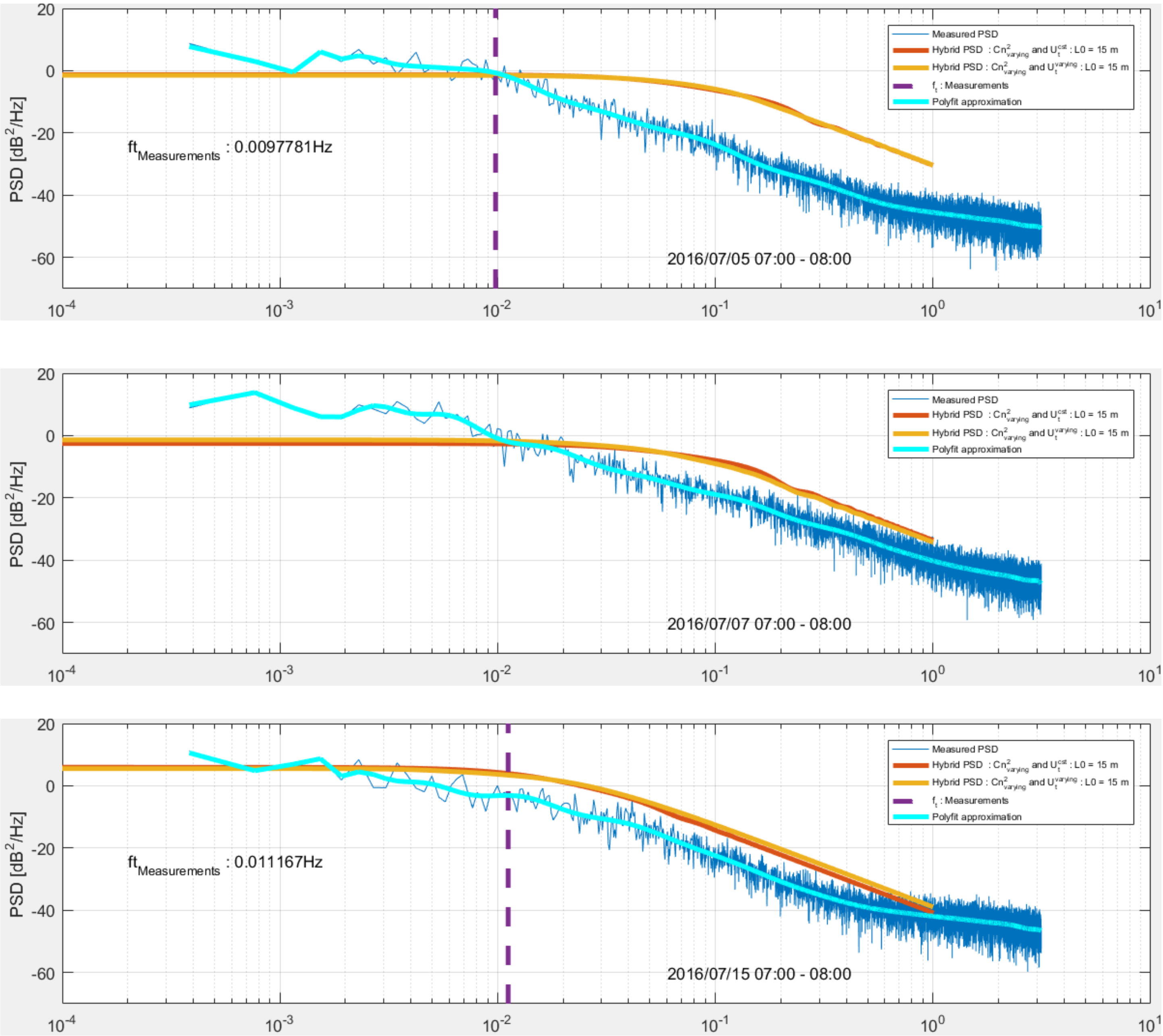

Figure 5.21 – PSD measurements versus the two PSD models

In the figure 5.21, we see that that our model does not change much when U_t is varying and that we can not clearly say if one is better than the other.

5.4 Choice and comparison of our 3 models

In this section, we are going to compare our 3 models and see which one is the closest to the measurements. Since considering a varying transverse wind speed has never changed much the spectrum for all our 3 models, we will only consider our 3 models with a constant U_t.

For this comparison, we will take $L_0 = 15\ m$. Our 3 models can be seen in figure 5.22 on the 5^{th}, 10^{th}, 15^{th}, 18^{th} and 26^{th} of July.

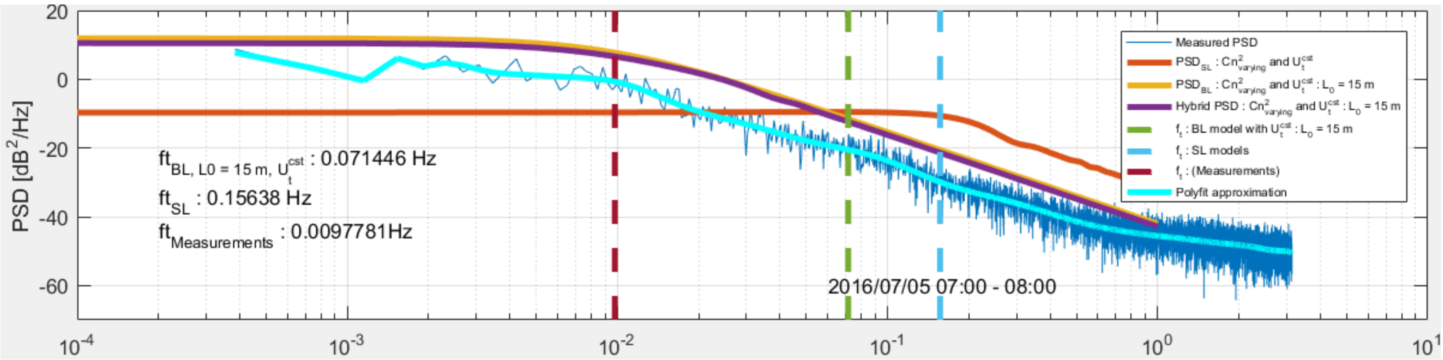

PSD [dB²/Hz]
ft_BL, L0 = 15 m, U_t^cst : 0.071446 Hz
ft_SL : 0.15638 Hz
ft_Measurements : 0.0097781Hz
2016/07/05 07:00 - 08:00
Measured PSD
PSD_SL : Cn²_varying and U_t^cst
PSD_BL : Cn²_varying and U_t^cst : L_0 = 15 m
Hybrid PSD : Cn²_varying and U_t^cst : L_0 = 15 m
f_t : BL model with U_t^cst : L_0 = 15 m
f_t : SL models
f_t : (Measurements)
Polyfit approximation

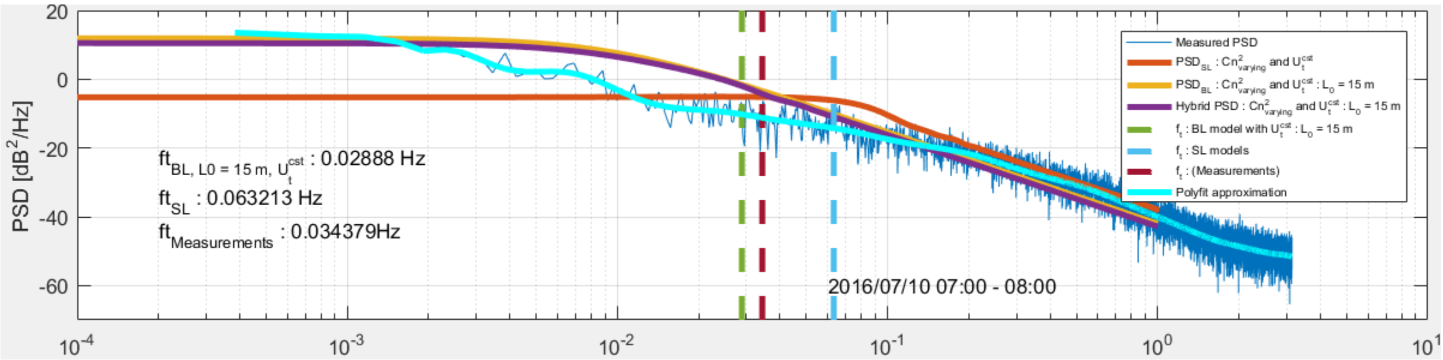

PSD [dB²/Hz]
ft_BL, L0 = 15 m, U_t^cst : 0.02888 Hz
ft_SL : 0.063213 Hz
ft_Measurements : 0.034379Hz
2016/07/10 07:00 - 08:00
Measured PSD
PSD_SL : Cn²_varying and U_t^cst
PSD_BL : Cn²_varying and U_t^cst : L_0 = 15 m
Hybrid PSD : Cn²_varying and U_t^cst : L_0 = 15 m
f_t : BL model with U_t^cst : L_0 = 15 m
f_t : SL models
f_t : (Measurements)
Polyfit approximation

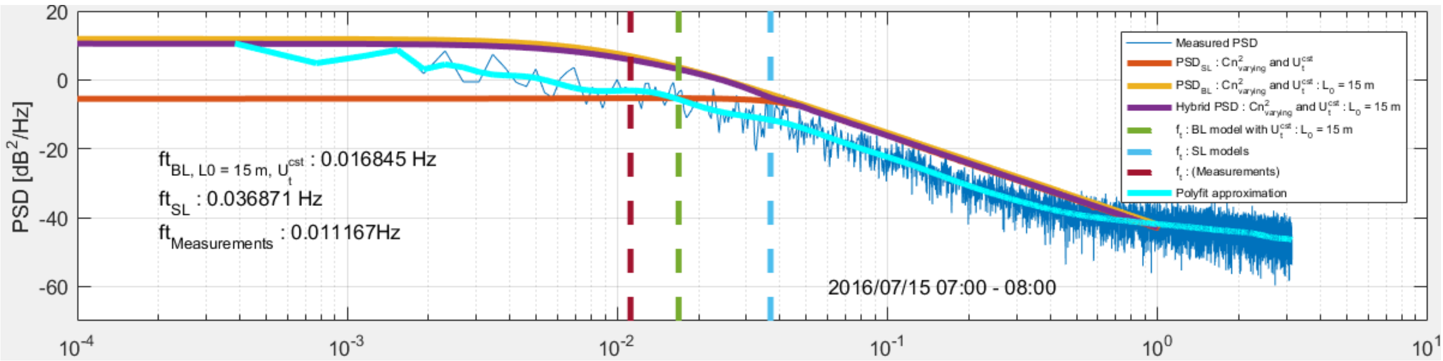

PSD [dB²/Hz]
ft_BL, L0 = 15 m, U_t^cst : 0.016845 Hz
ft_SL : 0.036871 Hz
ft_Measurements : 0.011167Hz
2016/07/15 07:00 - 08:00
Measured PSD
PSD_SL : Cn²_varying and U_t^cst
PSD_BL : Cn²_varying and U_t^cst : L_0 = 15 m
Hybrid PSD : Cn²_varying and U_t^cst : L_0 = 15 m
f_t : BL model with U_t^cst : L_0 = 15 m
f_t : SL models
f_t : (Measurements)
Polyfit approximation

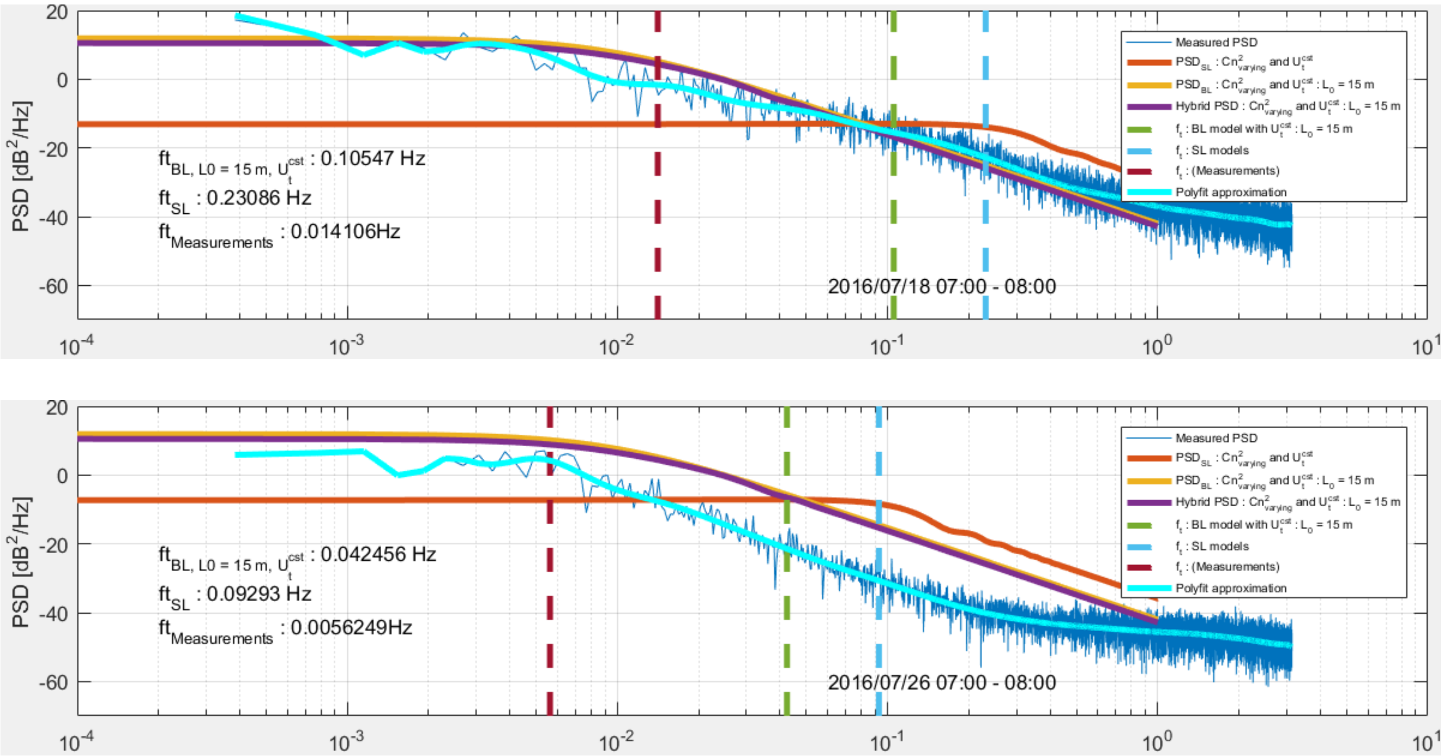

Figure 5.22 – PSD measurements versus the two PSD models

We can clearly see that our first model where $\sqrt{\lambda L} << L_0$ is not as good as the other two models. Our first model has always a too high transition frequency. If we now look at the other two models, we see that they almost overlap.

Nevertheless, our combined model has always a slightly smaller amplitude than our second model where $\sqrt{\lambda L} << L_0$. Since our second model often has a greater amplitude than the measurements (see figures 5.22 and 5.10), we can say that the combined model will be a little bit better than the second one. However, the amelioration is very small and not worth it.

Chapter 6

Conclusion

In this work, we developed several models in order to recreate the effect of the scintillation. This required us to go deep down in the fundamentals of wave propagation. Therefore, we had to understand a lot of theory and mathematical reasoning before being able to analyse the scintillation phenomenon.

Because of this complicated work of understanding, we did not have enough time to consider several things which could have been interesting. We will cite some examples here.

In the fourth chapter, the refractive structure constant was computed thanks to the definition of the structure function. Although, there are several methods which compute the C_n^2. Since the C_n^2 is never known with certainty, a comparison would have been a plus [7].

It could also have been worth to have a closer look at the value of L_0. As it was said in this work, its value is in general unknown but there are some articles which proposes new methods to compute it [2].

Furthermore, in this thesis, we have considered a constant turbulent zone of a 2 km depth but it would have maybe been better to adapt the turbulent zone depth day after day.

Finally, we did not have consider the influence of the antenna dish. Considering the size of the antenna would have maybe improved our scintillation model and given better results for the scintillation spectrum.

However, even if it would have been interesting to investigate these parameters, we can still make some conclusions about the scintillation models we made. Indeed, as it was seen in the last chapter, our two last models were quite close to the scintillation measurements. It seems that the hypothesis $\sqrt{\lambda L} >> L_0$ allows us to have a spectrum model which is often in accordance with the measurements. We would have expected an tangible amelioration from our combined method compared to the model where $\sqrt{\lambda L} >> L_0$ but unfortunately it is not the case (the amelioration is very small or absent).

In conclusion, we can say that for low-elevation link, our model with the hypothesis that the radius of the first Fresnel is larger than L_0 is quite precise to describe the scintillation phenomenon on most days. Therefore, this model could be a good start in order to predict the scintillation phenomenon at low-elevation angles and, in the future, enhance link budget design for radio communication systems.

Bibliography

[1] Constantinos N. Kassianides Ali Savvaris and Ifiok E. Otung. Observed effects of cloud and wind on the intensity and spectrum of scintillation. *IEEE Transactions on antennas and propagation*, 52(6), 2004.

[2] Y. Coqueugniot C. E. Coulman, J. Vernin and J. L. Caccia. Outer scale of turbulence appropriate to modeling refractive index structure profiles. *Applied optics*, 1988.

[3] Cheng Yee Chen and Mandeep Jit Singh. Comparison of tropospheric scintillation prediction models of the indonesian climate. *Earth, Planets and Space*, 2014. `https://link.springer.com/article/10.1186/1880-5981-66-64`.

[4] T. CHERUBINI and S. BUSINGER. Another look at the refractive index structure function. *Journal of Applied Meteorology and Climatology*, 2012.

[5] ECMWF. Part iii : Dynamics and numerical procedures. 2015.

[6] Fabrizio Cuccoli Enrica Martini, A. Freni and Luca Facheris. Derivation of clear-air turbulence parameters from high-resolution radiosonde data. *Journal of Atmospheric and Oceanic Technology*, 2016.

[7] Frank S. Marzano Giovanni d'Auria and Ugo Merlo. Model for estimating the refractive-index structure constant in clear-air intermittent turbulence. *Applied optics*, 1993.

[8] H.Vasseur and D.Vanhoenacker. Characterisation of tropospheric turbulent layers from radiosonde data. *Electronics letters*, 1998.

[9] Akira Ishimaru. Temporal frequency spectra of multifrequency waves in turbulent atmosphere. *IEEE*, 1972.

[10] Akira Ishimaru. *Wave Propagation and Scattering in Random Media*. Academic Press, 1978.

[11] Richard Raspet John M. Noble, W.C. Kirkpatrick Alberts and Mark A Coleman. Infrasound wind noise reduction via porous fabric domes. *The Journal of the Acoustical Society of America*, 2014.

[12] Jugandi. Fresnel zone, 2017. `https://en.wikipedia.org/wiki/Fresnel_zone`.

[13] Robert S. Lawrence and John W. Strohbehn. A survey of clear-air propagation effects relevant to optical communications. *IEEE*, 1970.

[14] Danielle Vanhoenacker-Janvier Martin Rytir, Carlo Riva and Terje Tjelta. Tropospheric scintillation spectra and transversal wind speed for satellite links at very low elevation angles. *IEEE*, 2017.

[15] The Editors of Encyclopædia Britannica. Atmospheric turbulencel modeling. `https://www.britannica.com/science/atmospheric-turbulence`.

[16] Carlos Pereira, Danielle Vanhoenacker-Janvier, Nicolas Jeannin Laurent Castanet, and Antonio Martellucci. Simulation of tropospheric scintillation on leo satellite link based on space-time channel modeling. *Archive ouverte pluridisciplinaire HAL*, 2014.

[17] International Telecommunication Union : Radiocommunications sector. The radio refractive index : its formula and refractive data. 2016.

[18] V.I. Tatarski. *Wave Propagation in a Turbulent Medium.* McGraw-Hill Book Company, 1961.

[19] V.I. Tatarski. *The effects of the turbulent atmosphere on wave propagation.* Jerusalem: Israel Program for Scientific Translations, 1971.

[20] D. Vanhoenacker-Janvier. Propagation in wireless media : Fundamentals. LELEC 2700 UCL.

[21] ENRIC VILAR and JOHN HADDON. Measurement and modeling of scintillation intensity to estimate turbulence parameters in an earth-space path. *IEEE Transactions on antennas and propagation*, AP-32(4), 1984.

[22] Richard Woo and Akira Ishimaru. Effects of turbulence in a planetary atmosphere on radio occultation. *IEEE Transactions on antennas and propagation*, AP-22(4), 1974.

[23] Daniel Zwilinger. *Table of Integrals, Series and Products.* Academic Press, 2014.

Rue Archimède, 1 bte L6.11.01, 1348 Louvain-la-Neuve **www.uclouvain.be/epl**